



**Center for Advanced
Communications**

Villanova University

TECHNICAL REPORT

(10/1/01 – 9/30/02)

**CLASSIFICATION AND DISCRIMINATION OF SOURCES
WITH TIME-VARYING FREQUENCY AND SPATIAL SPECTRA**

Submitted to

Office of Naval Research

Grant No. N00014-98-1-0176

Principal Investigator

Moeness G. Amin

Contributors

Prof. Moeness Amin
Dr. Gordon Frazer
Dr. Yimin Zhang
Dr. Fauzia Ahmad

October 2002

DISTRIBUTION STATEMENT A
Approved for Public Release
Distribution Unlimited

20021008 194

Table of Contents

Executive Summary	i
1. Characterization of near-field scattering using quadratic sensor-angle distributions	i
2. Improved blind separations of nonstationary sources based on spatial time-frequency distributions	ii
3. A unified representation of nonstationary and cyclostationary signals	ii
4. Aperture synthesis for a through-the-wall imaging system	ii
5. Nonstationary interference suppression in DS/SS communications using space-time oblique projection techniques	ii
6. Time-frequency ESPRIT for direction-of-arrival estimation of chirp signals	iii
7. Automatic classification of auto- and cross-terms of time-frequency distributions in antenna arrays	iii
8. A new approach to FM jammer suppression for digital communications	iii
List of Publications	iv
Appendix (Publications)	
Characterization of near-field scattering using quadratic sensor-angle distributions	1
Improved blind separations of nonstationary sources based on spatial time-frequency distributions	32
A unified representation of nonstationary and cyclostationary signals	44
Aperture synthesis for through-the-wall imaging system	53
Time-frequency ESPRIT for direction-of-arrival estimation of chirp signals	69
Automatic classification of auto- and cross-terms of time-frequency distributions in antenna arrays	81
ONR FY02 Collection Data	94

Executive Summary

Classification and Discrimination of Sources with Time-Varying Frequency and Spatial Spectra

ONR, Grant no. N00014-98-1-0176

Moeness Amin (PI)

This report presents the results of the research performed under ONR grant number N00014-98-1-0176 over the period of October 1st, 01 to September 30th, 02. The research team working on this project consists of: Prof. Moeness Amin (PI), Dr. Gordon Frazer (DSTO, Australia), Dr. Yimin Zhang (Postdoctoral Fellow), Dr. Fauzia Ahmad (Postdoctoral Fellow), Mr. Behzad Mohammadi (Graduate Student). We have also collaborated with Dr. Alex Gershman from McMaster University, Canada, Prof. H. Ge from NJIT, Dr. N. Ma from DSO, Singapore, and Prof. A. Zoubir from Curtin University, Australia. The research over this fiscal year has produced 6 journal papers and 8 conference papers. Copies of the principle publications are included in the report.

The research efforts over the past year have focused on improved characterization, separations, suppression, discrimination, and localization of nonstationary and cyclostationary sources using multi-sensor array receivers. The major contributions over the 2001-2002 fiscal year are: 1) Characterization of near-field scattering using quadratic sensor-angle distributions, 2) Improved blind separations of nonstationary sources based on spatial time-frequency distributions, 3) Introducing a unified representation of nonstationary and cyclostationary signals, 4) Devising aperture synthesis for a through-the-wall imaging system, 5) Nonstationary interference suppression in direct sequence spread spectrum communications using space-time oblique projection techniques, 6) Formulating the time-frequency ESPRIT for direction-of-arrival estimation of chirp signals, 7) Automatic classification of auto- and cross-terms of time-frequency distributions in antenna arrays, 8) Proposing a new approach to jammer suppression for digital communications.

1. Characterization of Near-Field Scattering Using Quadratic Sensor-Angle Distributions

We have introduced the quadratic sensor angle distribution (SAD) for near-field source characterization. The SAD is a joint-variable distribution and a dual in sensor number and angle to Cohen's class of time-frequency distributions. It provides the power at every angle for each sensor in the array. In this distribution, near-field sources have different angle for each sensor. We use a known test source to illuminate the local scatterer distribution we wish to characterize. The high-power test source can be removed via orthogonal projection so as to reveal the less powerful local scatter. It is shown that the eigen-decomposition of the quadratic representation of SAD lends itself to source representation via multiple subarray beamforming. The SAD can be used to clearly identify scatterers on the array axis both within and beyond the array extent. Distinction between far-field spatial spread source and near-field point source can also be easily achieved.

2. Improved Blind Separations of Nonstationary Sources Based on Spatial Time-Frequency Distributions

Blind source separation based on spatial time-frequency distributions (STFDs) provides improved performance over blind source separation methods based on second-order statistics, when dealing with nonstationary signals that are localizable in the time-frequency (t-f) domain. In the existing STFD methods, the covariance matrix is first used to whiten the data vector, then the mixing matrix and subsequently the source waveforms are estimated using STFD matrices constructed from the source t-f autoterm points. We have improved the STFD-based source separation method by performing both whitening and estimation steps using the source t-f signatures. This modification provides robust performance to noise, and allows reduction of the number of sources considered for separation.

3. A Unified Representation of Nonstationary and Cyclostationary Signals

The cyclic auto-correlation function, commonly used for cyclostationary signals, and the ambiguity function, typically employed for analysis and recovery of nonstationary signals, such as FM, have the same formulation. However, nonstationary and cyclostationary signals have distinct localization properties in the time-lag frequency-lag domain. Therefore, nonstationary and cyclostationary signals can be represented and processed within the same framework for many applications, with the distinct signatures allowing effective source discriminations. An example in array processing is given where nonstationary and cyclostationary signals are separated following simple spatial signature estimation exploiting the aforementioned properties.

4. Aperture Synthesis for a Through-the-Wall Imaging System

An aperture synthesis scheme using subarrays that is based on the coarray concept is proposed for through-the-wall microwave imaging applications. Simulation results depicting the effectiveness of the proposed synthetic aperture technique for a TWI system are presented. The effects of incorrect estimates of wall parameters and errors in array element placement on this technique are also investigated.

5. Nonstationary Interference Suppression In DS/SS Communications Using Space-Time Oblique Projection Techniques

Orthogonal space-time subspace using a multi-antenna array has been recently proposed as an effective means for nonstationary interference suppression in direct-sequence spread-spectrum (DS/SS) communications. Interference mitigation techniques may compromise the desired signal in the process of removing the interferers. This effect is known as self-noise. The orthogonal subspace projection introduces self-noise and signal distortions due to potentially high correlation between the spatio-temporal signature of the DS/SS signal and that of the interferers. We propose to use the space-time oblique projection, instead of the orthogonal subspace projection. The oblique projection, while completely suppresses interferers, does not distort the desired signal and, therefore, no self-noise is generated. The performance of a receiver with space-time oblique projection, along with the sensitivity to the errors in spatio-temporal signatures of the signals and interferers, is analyzed and compared with the receiver performance employing the orthogonal subspace projection method.

6. Time-Frequency ESPRIT for Direction-of-Arrival Estimation of Chirp Signals

We have developed an ESPRIT-type algorithm for estimating the Directions-Of-Arrival (DOA's) of multiple chirp signals using Spatial Time-Frequency Distributions (STFD's). An averaged STFD matrix (or multiple averaged STFD matrices) are used instead of the covariance matrix to estimate the signal and noise subspaces. The proposed algorithm is shown to provide a significant performance improvement over the traditional ESPRIT algorithm for FM sources, specifically in situations with closely spaced sources and low Signal-to-Noise Ratios (SNR's). Simulation results are provided to illustrate the performance of the proposed approach in scenarios with multiple narrowband chirp sources.

7. Automatic Classification of Auto-and Cross-Terms of Time-Frequency Distributions in Antenna Arrays

The problem of selecting auto- and cross-terms of time-frequency distributions (TFDs) of nonstationary signals impinging on a multi-antenna receiver is considered. A detection approach is introduced which allows performance measurement and comparison of various schemes via receiver operating characteristics. Array averaging and array differencing techniques are both employed to form a basis for time-frequency point selection. The proposed classification method is evaluated against the bootstrap-based method. It is shown that the former offers improved performance and simplified implementations.

8. A New Approach to FM Jammer Suppression for Digital Communications

We have considered the problem of FM jammer suppression in digital communications. It is pointed out that the cyclic auto-correlation function, commonly used for cyclostationary signals, and the ambiguity function, typically employed for analysis and recovery of nonstationary signals, such as FM, have the same formulation. However, nonstationary and cyclostationary signals have distinct localization properties in the time-lag frequency-lag domain, and this property can be effectively used for jammer suppression. Utilizing the spread of an FM jammer signature beyond that of the communication signal, one can select the jammer-only time-lag frequency-lag points for effective jammer spatial signature estimation. Suppression of the jammer signal is then proceeded by projecting the received signal to the jammers' orthogonal spatial subspace. Simulation examples for the recovery of BPSK signals in the presence of strong and moderate FM jammers are presented.

List of Publications

- * G. Frazer and M. Amin, "Characterization of near-field scattering using quadratic sensor-angle distributions," submitted to IEEE Transactions on Signal Processing, September 2002.
- W. Mu, M. G. Amin, and Y. Zhang, "Bilinear signal synthesis in array processing," Accepted for publication in the IEEE Transactions on Signal Processing.
- Y. Zhang and M. G. Amin, "Array processing for nonstationary interference suppression in DS/SS communications using subspace projection techniques," IEEE Transactions on Signal Processing, Dec. 2001.
- A. Gershman, M. Pesavento, M. Amin, "Estimating parameters of multiple wideband polynomial-phase sources in sensor arrays," IEEE Transactions on Signal Processing, Dec. 2001.
- * Y. Zhang and M. G. Amin, "Improved blind separations of nonstationary sources based on spatial time-frequency distributions," submitted to IEEE Signal Processing Letters, June 2002
- * Y. Zhang, M. G. Amin, and G. J. Frazer, "A unified representation of nonstationary and cyclostationary signals," submitted to IEEE Signal Processing Letters, August 2002.
- * A. Hassanien, A. B. Gershman, and M. G. Amin, "Time-frequency ESPRIT for direction-of arrival estimation of chirp signals," IEEE Sensor Array and Multichannel Signal Processing Workshop, Rosslyn, VA, Aug. 2002.
- Y. Zhang and K. Yang, "Subband adaptive arrays with different decimations," Proceedings of the IEEE Sensor Array and Multichannel Signal Processing Workshop, Rosslyn, VA, Aug. 2002.
- Y. Zhang, M. G. Amin, and G. J. Frazer, "A new approach to FM jammer suppression for digital communications", Proceedings of the IEEE Sensor Array and Multichannel Signal Processing Workshop, Rosslyn, VA, Aug. 2002.
- G. J. Frazer and M. G. Amin, "Characterization of near-field scattering using a multiple weighted summed beamformer", Proceedings of SPIE 2002, Advanced Signal Processing Algorithms, Architectures and Implementations XII, Seattle, WA, July 2002.
- * L. Cirillo, A. Zoubir, N. Ma, and M. Amin, "Automatic classification of auto-and cross-terms of time-frequency distributions in antenna arrays," Proceedings of the IEEE International Conference on Acoustics, Speech and Signal Processing, Orlando, FL, May 2002.
- G. J. Frazer and M. G. Amin, "Characterization of near-field scattering using quadratic sensor-angle distributions", Proceedings of the IEEE International Conference on Acoustics, Speech and Signal Processing, Orlando, FL, May 2002.
- L. A. Cirillo, A. M. Zoubir, and M. G. Amin, "Selection of auto- and cross-terms for blind non-stationary sources separation," Proceedings of the 1st IEEE International Symposium on Signal Processing and Information Technology, Cairo, Egypt, December 2001.
- G. J. Frazer and M. G. Amin, "Near-field scatter measurements using quadratic sensor-angle distributions", Proceedings of the Second IEEE Sensor and Multichannel Signal Processing Workshop, Washington, DC, Aug. 2002.

Papers marked (*) are included in the report.

Appendix

Publications

Characterization of Near-Field Scattering Using Quadratic Sensor-Angle Distributions

Gordon J. Frazer and Moeness G. Amin

Abstract

We introduce the quadratic sensor angle distribution (SAD) for near-field source characterization. The SAD is a joint-variable distribution and a dual in sensor number and angle to Cohen's class of time-frequency distributions. It provides the power at every angle for each sensor in the array. In this distribution, near-field sources have different angle for each sensor. We use a known test source to illuminate the local scatterer distribution we wish to characterize. The high-power test source can be removed via orthogonal projection so as to reveal the less powerful local scatter. It is shown that the eigen-decomposition of the quadratic representation of SAD lends itself to source representation via multiple subarray beamforming. The SAD can be used to clearly identify scatterers on the array axis both within and beyond the array extent. Distinction between far-field spatial spread source and near-field point source can also be easily achieved.

I. Introduction

In this paper, we propose a new method for characterizing the near-field electromagnetic scatter local to a linear equi-spaced array of electromagnetic sensors. The particular application is from the area of high frequency surface-wave radar, although the proposed method may be also applied in other sensor array applications, provided the array is linear and equi-spaced and the local scatterers are in the near-field.

Surface-wave radar is an emerging coastal and exclusive economic zone surveillance technology. Surface-wave radar systems used in this role are located at a land-sea boundary and use surface-wave propagation and the conductivity of sea water to detect and track targets across water beyond the line-of-sight radar horizon. Detection and tracking of small surface vessels can be achieved at ranges in excess of 200km where the optical horizon may be no more than 20km. These radars operate in the congested lower HF (approximately 3-10MHz) section of the electromagnetic spectrum. The systems with which we have experience use floodlight transmission and an array of receiver sensors. A mix of classical digital beamforming, space-time adaptive processing, and high resolution angle algorithms are used to determine target direction.

A typical surface-wave radar receiving array may consist of between 8 and 64 sensors and can be 500m or 1km in total length. It is typically sited on a coastal beach which may or may not provide a uniform transition from land to sea. For example, the coast may in fact be a bay in which case the land sea boundaries beyond either end of the array may cause near-field scattering and distort the wave-front arriving at the array. There may be other locally sited structures, such as buildings and fences, which can be the source of local scatter (consider that the wavelength of the radar signal is between 30-100m). This makes achieving very low sidelobe spatial beams with a classical beamformer a difficult problem and can render the receiver system vulnerable to interference through beam sidelobes (possibly via skywave propagation).

The near-field scatter produced by these mechanisms are correlated with the desired direct far-field radar return from targets (and clutter). This scatter is typically approximately 20-40dB weaker than the direct signal. Without mitigation it is possible to achieve classical beam sidelobes of 30-35dB, however in general the remaining components of the receiving system can sustain substantially higher performance [1].

A method is required that can mitigate the effect of local scatter so that the radar system can realize the inherent sidelobe capability as set by the radar equipment [1]. An important part of this strategy is to first characterize the local scatter distribution. A means of performing this characterization is the subject of the work we present in this paper.

Breed and Posch introduced the spatial Wigner distribution (SWD) as a tool for determining the range and angle of a near field source [2]. They exploited the property that the phase front

of a wave emanating from a source in the near field of an array has an approximately quadratic phase law, or equivalently an approximately linear spatial frequency law. The true propagating wave phase front is in fact spherical and is only approximately quadratic for near field sources some distance from the array, and therefore, the method in [2] breaks down for sources close to the array.

A comprehensive treatment of SWD was given by Swindlehurst and Kailath in [3]. They included an examination of the applicability of the quadratic-spherical approximation and use a parametric high resolution technique to determine the linear frequency law parameters (and hence the near-field source position).

More recently a related but altogether different spatial time-frequency distribution (STFD) was introduced in [4], [5]. This is a true spatial TFD in that individual entries in the array spatial covariance matrix are replaced by time-frequency representations of the energy comprising these entries (both auto and cross) throughout the interval T . This approach has been applied successfully to two challenging array processing problems; blind signal separation and angle estimation.

There is a substantial body of literature concerned with processing spatial signals received by an array of sensors from sources in the near-field of the array, e.g. [6]. It is mostly concerned with techniques for estimating the angle and range of the source. Both a subspace method and a maximum likelihood algorithm are presented in [7].

Several authors have proposed methods for determining the angle of distributed sources located in the far-field of an array [8], [9]. These techniques address the effect of scatter local to a transmitter in the far-field and not for scatter that is sufficiently local to the receiving system to be in the near field of the array. In this paper, we propose a generalization of the spatial Wigner distribution introduced in [2], combined with orthogonal projection techniques for the characterization of the structure of local electromagnetic scattering induced by the near environment and mutual interaction between sensors in the array. We use a known test source to illuminate the local scatterer distribution we wish to characterize. The high-power test source can be removed via orthogonal projection so as to reveal the less powerful local scatter. It is shown that the eigen-decomposition of the quadratic representation of SAD lends itself to source representation via multiple subarray beamforming. The SAD can be used to clearly identify scatterers on the array axis both within and beyond the array extent. Distinction between far-field spatial spread source and near-field point source can also be easily achieved.

This paper is organised as follows. In section 2, a signal model for far-field and near-field sources are presented. Both point and spatial spread sources are considered. The sensor-angle distribution is introduced in section 3. The source range and angle expressions viewed by each

sensor are presented in section 4 using the geometrical relation between the source of interest and the array. Exact and least-squares maximum estimates of the source range and angle, along with Cramer-Rao bound, measured from the center of the array using the respective SAD estimates at each sensor are also derived in section 4. Alias-free implementations and subarray beamforming interpretation of the SAD are delineated in Section 5. Section 6 includes simulations demonstrating the offerings of the SAD in near-field source characterization.

II. Signal Model

A. Model

Our proposed measurement technique requires one cooperative source, S , with complex envelope s_k^S , in the far-field of the array at known angle θ^S and where k denotes time index. Consider a linear equi-spaced array of M sensors, where sensor position errors are negligible and the gain and phase of all sensors are accurately matched. Steering vectors for the far-field $\mathbf{a}(\theta)$ and near-field $\mathbf{a}(\theta, \mathbf{r})$ take on the standard form with θ being the angle. For the near-field steering vector, r denotes range [10].

Assume that the conditions on the test source and sensor array are such that the following signal model is appropriate

$$\mathbf{z}_k = \mathbf{A}\mathbf{S}_k + \mathbf{q}_k + \mathbf{n}_k \quad (1)$$

In this model, \mathbf{z}_k is a vector of dimension M , representing the k^{th} snapshot of sensor outputs. The vector \mathbf{q}_k consists of additive spatial and temporal coloured noise produced in the environment, and \mathbf{n}_k represents additive white noise modeling the internal noise of the array of sensors receiving system.

The matrix \mathbf{A} can take on one of two forms, depending on whether the local scatterer is best modeled as a collection of P discrete point scatterers, or as a single spatially distributed scatterer. For the case of P discrete scatterers

$$\mathbf{A} = [\mathbf{a}(\theta^S), \mathbf{a}(\theta_1, \mathbf{r}_1), \dots, \mathbf{a}(\theta_i, \mathbf{r}_i), \dots, \mathbf{a}(\theta_P, \mathbf{r}_P)] \quad (2)$$

In the above equation, the near-field scatterer $i = 1, \dots, P$ is characterized by the angle θ_i and range r_i . In the case of a distributed scatterer contained in the near field azimuth and range set Ω , with reflectivity, $R_\Omega(\theta, r)$ and with respect to a reference location (θ_0, r_0)

$$\mathbf{a}^\Omega(\theta_0, \mathbf{r}_0) = \frac{\int_\Omega \mathbf{R}_\Omega(\theta' - \theta_0, \mathbf{r}' - \mathbf{r}_0) \cdot \mathbf{a}(\theta' - \theta_0, \mathbf{r}' - \mathbf{r}_0) \, d\theta' \, d\mathbf{r}'}{\|\int_\Omega \mathbf{R}_\Omega(\theta' - \theta_0, \mathbf{r}' - \mathbf{r}_0) \cdot \mathbf{a}(\theta' - \theta_0, \mathbf{r}' - \mathbf{r}_0) \, d\theta' \, d\mathbf{r}'\|} \quad (3)$$

and hence

$$\mathbf{A} = [\mathbf{a}(\theta^S), \mathbf{a}^\Omega(\theta_0, \mathbf{r}_0)] \quad (4)$$

Likewise, the signal vector \mathbf{S}_k can be constructed in two ways, depending on whether the near-field scatterers are best modeled as discrete or distributed. For the discrete case,

$$\mathbf{S}_k = [\mathbf{s}_k^S, \mathbf{s}_k^1, \dots, \mathbf{s}_k^P] \quad (5)$$

where the test source complex amplitude is given by s_k^S and the complex amplitude of the i^{th} of P discrete scatterers is denoted as s_k^i . In the distributed scatterer case,

$$\mathbf{S}_k = [\mathbf{s}_k^S, \mathbf{s}_k^\Omega] \quad (6)$$

The s_k^S and s_k^i and s_k^Ω may be uncorrelated or correlated for each case respectively.

The i^{th} element of the steering vector for the far-field source (the first column of \mathbf{A}) $\mathbf{a}(\theta^S)$ takes on the standard form

$$a_i(\theta^S) = \exp \left(-j \frac{2\pi d}{\lambda} \sin \theta^S \cdot \left[(i-1) - \frac{M-1}{2} \right] \right) \quad (7)$$

whereas, in the case of any near-field source or scatterer, the i^{th} element of the steering vector $\mathbf{a}(\theta_s, \mathbf{r}_s)$, is given by

$$a_i(r_s, \theta_s) = \frac{1}{r_{s,i}} \cdot \exp \left(-j \frac{2\pi}{\lambda} \cdot r_{s,i} \right) \quad (8)$$

assuming a normalized and equal gain for each sensor.

The spatial environment is characterized by the spatial covariance matrix $\mathbf{R}_{k,m}$, where

$$\mathbf{R}_{k,m} = \mathbf{A} \mathbf{S}_{k,m} \mathbf{A}^H + \mathbf{Q}_{k,m} + \sigma^2 \mathbf{I} \quad (9)$$

with $\mathbf{R}_{k,m} = \mathbf{E}[\mathbf{z}_k \mathbf{z}_m^H]$, the source covariance $\mathbf{S}_{k,m} = \mathbf{E}[\mathbf{s}_k \mathbf{s}_m^H]$, and the noise covariance $\mathbf{Q}_{k,m} = \mathbf{E}[\mathbf{q}_k \mathbf{q}_m^H]$. Assume that \mathbf{s}_k , \mathbf{q}_k and \mathbf{n}_k are uncorrelated, that $\mathbf{S}_{k,m} = \mathbf{S} \delta_{k-m}$ and $\mathbf{Q}_{k,m} = \mathbf{Q} \delta_{k-m}$, and that $\mathbf{S} \delta_k = \mathbf{S} \delta_{k'}$ and $\mathbf{Q} \delta_k = \mathbf{Q} \delta_{k'}$ for k different from k' . In this case \mathbf{S} , \mathbf{Q} and hence \mathbf{R} are temporally white and stationary, and as such we can remove the dependency on k and m . These assumptions are not in fact strictly required but we include them in order to reasonably bound the class of signals we consider in the subsequent discussions. The variance of the receiver internal noise is σ^2 . Individual elements of matrix \mathbf{S} are denoted as ρ_{ij} .

We ensure that the cooperative test source has sufficient signal to noise ratio (generally greater than 50dB) to perform our measurement by requiring that

$$\rho_{\text{snr}} = \frac{\rho_{11}}{(\sigma^2 + \text{tr}[\mathbf{Q}])} \gg 1 \quad (10)$$

It is also expected that the direct far-field source power will be substantially greater than the total near-field power (by 20-40dB), i.e.,

$$\rho_{\text{snf}} = \frac{\rho_{11}}{\sum_{k=2}^P \rho_{k,k}} \gg 1 \quad (11)$$

III. Sensor-Angle Distributions

The proposed method uses an extension to the spatial Wigner distribution originally introduced by Breed and Posch [2]. To avoid confusion, it has been necessary to change the name to reflect the generalization to all members of Cohen's class of quadratic distributions [11]. While the title "spatial Wigner distribution" is informative, retaining the name "spatial time-frequency distribution" for the remaining members of Cohen's class applied to spatial signals does not correctly describe the distribution we are interested in. Therefore, in this work, we have renamed the class of quadratic distributions applied to spatial signals to be *sensor-angle distributions* (SAD). The corresponding spectra are called sensor-angle spectra (SAS).

The Cohen's class SAD for the k^{th} snapshot is a distribution of the angle of sources impinging on the array *at each sensor*,

$$\mathbf{T}_k(i, \theta; \mathbf{z}_k) = \sum_{l=-\infty}^{\infty} \sum_{m=-\infty}^{\infty} \phi(m, l) \mathbf{z}_k(i + m + l) \mathbf{z}_k^*(i + m - l) e^{-j4\pi\theta l} \quad (12)$$

where i and θ are the sensor index and angle respectively. The kernel $\phi(m, l)$ characterizes the distribution and is a function of sensor position, m , and sensor lag, l . All the standard data-independent or data-dependent kernel designs applied in the time-frequency literature may be used with the SAD [11].

The sensor-angle spectrum (SAS) is the *power* (not energy or energy density) distribution of the sources impinging on the array. The SAS is given by

$$\mathbf{T}^S(i, \theta; \mathbf{z}_k) = \mathbf{E}[\mathbf{T}_k(i, \theta; \mathbf{z}_k)] \quad (13)$$

where an estimate for temporally stationary sources is given by

$$\hat{\mathbf{T}}^S(i, \theta; \mathbf{z}_k) = \frac{1}{N} \sum_{k=0}^{N-1} \mathbf{T}_k(i, \theta; \mathbf{z}_k) \quad (14)$$

for N snapshots.

The objective is to use the SAD (or SAS) to characterise the near-field scatterers of a far-field source signal. We expect the test signal to be substantially more powerful than the local scatter we wish to characterize (see (11)). With the knowledge of the far-field source angle-of-arrival, a spatial filter can be designed to remove its dominance, allowing a clear depiction of the near field source in the sensor-angle (s-a) domain. Alternatively, a simple technique is to project the sensor data on the orthogonal subspace of the far-field source spatial signature. In (12) and (13), the data snapshot \mathbf{z}_k is replaced by $\mathbf{P}\mathbf{z}_k$ where \mathbf{P} is the orthogonal projection operator formed from the test source steering vector $\mathbf{a}(\theta^S)$ as

$$\mathbf{P} = \mathbf{I} - \mathbf{a}(\theta^S) [\mathbf{a}^H(\theta^S) \mathbf{a}(\theta^S)]^{-1} \mathbf{a}^H(\theta^S) \quad (15)$$

Therefore, we compute the SAS

$$\hat{\mathbf{T}}^S(\mathbf{i}, \theta; \mathbf{P})|_{\theta^S} \quad (16)$$

associated with a test source in the far-field of the array at angle θ^S .

In some applications, a single test angle will provide sufficient characterization using (16) while in other applications, two or many test angles will be required, in which case the full characterization is given by

$$\hat{\mathbf{T}}^S(\mathbf{i}, \theta; \mathbf{P}(\theta^S)) \quad (17)$$

as θ^S is scanned over the required domain of angles for the test source.

IV. Range-Angle Estimation from SAD

A. Geometry

A.1 Assumptions

Consider a linear equi-spaced array of M sensors placed on a flat plane in a two dimensional surface. Assume that sensor position errors are negligible and the gain and phase of all sensors and corresponding data acquisition equipment are accurately matched. Assume that the array is narrowband, i.e., the reciprocal of the bandwidth of any signals received is large compared with the propagation delay across the array. The wavelength of all sources received is λ . Let the origin of a coordinate system O be at the mid-point of the array, with the sensors individually spaced by d regularly along the x-axis and indexed $i = 1, \dots, M$ from left to right. We assume that $d < \frac{\lambda}{2}$. Boresight is along the y-axis.

A source is placed in the near-field (i.e. a circular wavefront impinges on the array) at location r_s meters from the origin and θ_s degrees from boresight. We define that angles are to be measured clockwise from array boresight (the y-axis). For M odd, there is a sensor at the origin, whereas for M even, the origin is midpoint between two sensors. The array geometry and the notations are shown in figure 1 for the case of $M = 8$.

A.2 Sensor angle for a source at (r_s, θ_s)

The physical position of some point along the axis of the array, with respect to an origin O at the midpoint, is denoted x . The position of the i^{th} sensor in the array can be written

$$x = d \cdot \left[(i - 1) - \frac{M - 1}{2} \right] \text{ for } i \in \{1, \dots, M\} \quad (18)$$

The distance from position x to a source at (r_s, θ_s) is

$$r_{s,x} = \sqrt{x^2 - 2 \cdot r_s \cdot x \cdot \sin \theta_s + r_s^2} \quad (19)$$

with the angle given by

$$\theta_{s,x} = \cos^{-1} \left[\frac{x^2 + r_{s,x}^2 - r_s^2}{2 \cdot x \cdot r_{s,x}} \right] - \frac{\pi}{2} \quad (20)$$

Substituting equation (19) into equation (20) eliminates the dependency on $r_{s,x}$ so that $\theta_{s,x}$, which is the angle from position x to the given source at (r_s, θ_s) , may now be written directly in terms of the source location

$$\theta_{s,x} = \cos^{-1} \left[\frac{x - r_s \cdot \sin \theta_s}{\sqrt{x^2 - 2 \cdot r_s \cdot x \cdot \sin \theta_s + r_s^2}} \right] - \frac{\pi}{2} \quad (21)$$

A specific case of interest is the angle at each sensor, which may be expressed as a function of the source location and the sensor number $i \in \{1, \dots, M\}$.

$$\theta_{s,i} = \Theta(i, r_s, \theta_s) \text{ for a given } d \text{ and } M \quad (22)$$

Substituting equation (18) into equation (21) gives a direct expression for the angle at the i^{th} sensor to a source at location (r_s, θ_s)

$$\Theta(i, r_s, \theta_s) = \cos^{-1} \left[\frac{[d \cdot [(i-1) - \frac{M-1}{2}]] - r_s \cdot \sin \theta_s}{\sqrt{[d \cdot [(i-1) - \frac{M-1}{2}]]^2 - 2 \cdot r_s \cdot [d \cdot [(i-1) - \frac{M-1}{2}]] \cdot \sin \theta_s + r_s^2}} \right] - \frac{\pi}{2} \quad (23)$$

A.3 Source location from sensor angle

Given knowledge of the sensor-angle at any two or more sensors, it is possible to determine the range and bearing (r_s, θ_s) of a source. This is, however, subject to identifiability requirements that each sensor has a different angle to the source, which is in fact a requirement that the source be in the near-field of the array. Given $\theta_{s,i}$ and $\theta_{s,j}$ with $i \neq j$, one determines sensor to source ranges $r_{s,i}$ and $r_{s,j}$ respectively using

$$r_{s,i} = [|i - j|] \cdot d \cdot \frac{\cos[\theta_{s,j}]}{\sin[\theta_{s,i} - \theta_{s,j}]} \quad (24)$$

and

$$r_{s,j} = [|i - j|] \cdot d \cdot \frac{\cos[\theta_{s,i}]}{\sin[\theta_{s,i} - \theta_{s,j}]} \quad (25)$$

This requires that $\theta_{s,i} - \theta_{s,j} \neq 0$. The range and bearing with respect to the origin can be determined relative to any of the individual sensors using the individual sensor range and bearing. For example, for the j^{th} sensor, we use $r_{s,j}$ and $\theta_{s,j}$ according to

$$r_s^2 = r_{s,j}^2 + \left[\left[\frac{M-1}{2} - [j-1] \right] \cdot d \right]^2 - 2 \cdot r_{s,j} \cdot \left[\left[\frac{M-1}{2} - [j-1] \right] \cdot d \right] \sin \theta_{s,j} \quad (26)$$

and

$$\theta_s = \cos^{-1} \left[\frac{r_{s,j}}{r_s} \cos \theta_{s,j} \right] \quad (27)$$

A.4 Estimating source location

Alternatively, an estimate for source location can be determined given estimates of the sensor angle $\hat{\theta}_{s,i}$ and equation (23). The least squares estimate for source location is

$$(\hat{r}_s^{LS}, \hat{\theta}_s^{LS}) = \arg \min_{r_s, \theta_s} \left[\sum_i [\hat{\theta}_{s,i} - \Theta(i, r_s, \theta_s)]^2 \right] \quad (28)$$

and, under the assumption

$$[\hat{\theta}_{s,i} - \theta_{s,i}] \rightarrow \mathcal{N}(0, \sigma_i^2) \quad (29)$$

then the maximum likelihood estimate for source location is

$$(\hat{r}_s^{MLE}, \hat{\theta}_s^{MLE}) = \arg \min_{r_s, \theta_s} \left[\sum_i [\hat{\theta}_{s,i} - \Theta(i, r_s, \theta_s)]^2 \right] \quad (30)$$

B. Cramer-Rao Bound for Location from Sensor Angle Measurements

Estimating the angle to a source at each sensor from a spatial signal is analogous to estimating the instantaneous frequency (IF) of a single component time domain signal. Numerous techniques for estimating IF have been proposed, including methods based on model fitting of unwrapped phase estimates, and from extraction of the peak value at each time in particular time-frequency distributions [12]. More recently a technique using iterative linear representations of the signal has been proposed based on the cross polynomial Wigner distribution [13].

Performance bounds for IF estimation are given in [14] and a comparison of several IF estimation techniques with respect to the Cramer-Rao lower bound (CRLB) is given in [13]. These results are applicable for high signal to noise ratio cases and include expressions for bias and variance in the overall frequency function of time estimates (and not at one instant of time). These results show that the estimate will be biased for IF laws other than constant or linear (using a second order TFD) or for a polynomial IF law of order greater than the order of a polynomial TFD.

Recently, expressions for the bias and variance of IF estimates based on extracting the peak of a TFD at each time have been developed for the case of low signal to noise ratio (SNR) [15]. These results explain the outlier behaviour frequently observed when using peak extraction algorithms at low SNR. The authors have partitioned the error behaviour into two mechanisms, corresponding to high and low SNR, and provide insight into when each mechanism applies.

Regardless of the particular IF estimation technique, the aforementioned performance bounds governing IF estimation at each data sample can be applied to the problem of determining the localization performance for a near-field source, in range and angle, using sensor-angle measurements. Given knowledge of the IF (or sensor-angle) estimation error, we now derive the CRLB for the location of the source in range and angle.

The assumption that the sensor-angle measurement estimate errors are Gaussian and independent (high SNR case) (equation (29)) can be re-stated as the following sensor angle measurement model

$$\hat{\theta}_{s,i} = \Theta(i; r_s, \theta_s) + w_i \text{ for } i \in \{1, \dots, M\} \quad (31)$$

where $w_i \sim \mathcal{N}(0, \sigma_i^2)$ and $\mathbf{E}[\mathbf{w}_i \mathbf{w}_i^*] = \sigma_i^2 \delta_{i-i'}$ and where the variance of w_i may be different for each sensor i . The assumptions of Gaussianity and of independence of angle measurements at different sensors are discussed in [16] in the time-frequency context. These assumptions may not be satisfied for all members of SAD [15], however, they simplify the CRLB derivations discussed in the following section. Let

$$\mathbf{y} = [\hat{\theta}_{s,1}, \dots, \hat{\theta}_{s,M}]^T \quad (32)$$

be the vector of sensor angle measurements and let

$$\Theta(\mathbf{r}_s, \theta_s) = [\Theta(1; \mathbf{r}_s, \theta_s), \dots, \Theta(M; \mathbf{r}_s, \theta_s)]^T \quad (33)$$

be the vector of predicted measurements. The likelihood and log likelihood functions for this model are

$$p(\mathbf{y}; \mathbf{r}_s, \theta_s) = \prod_i^M \frac{1}{\sqrt{2\pi\sigma_i^2}} \exp\left(-\frac{1}{2\sigma_i^2} [\hat{\theta}_{s,i} - \Theta(i; \mathbf{r}_s, \theta_s)]^2\right) \quad (34)$$

and

$$\ln p(\mathbf{y}; \mathbf{r}_s, \theta_s) = -\sum_i^M \ln[\sqrt{2\pi} \cdot \sigma_i] - \sum_i^M \frac{1}{2\sigma_i^2} [\hat{\theta}_{s,i} - \Theta(i; \mathbf{r}_s, \theta_s)]^2 \quad (35)$$

Or, in vector form using equations (32) and (33) and with $\Sigma = \text{diag}(\sigma_1^2, \dots, \sigma_M^2)$ (where diag is the square matrix with the specified entries along the diagonal and zero elsewhere) we can write equation (34) as

$$\mathbf{y} \sim \mathcal{N}(\Theta(\mathbf{r}_s, \theta_s), \Sigma) \quad (36)$$

To determine the CRLB we require the Fisher Information matrix (FIM) (for the two parameters to be estimated r_s and θ_s)

$$\mathbf{I}(\mathbf{r}_s, \theta_s) = \begin{bmatrix} -\mathbf{E}\left[\frac{\partial^2 \ln p(\mathbf{y}; \mathbf{r}_s, \theta_s)}{\partial \mathbf{r}_s^2}\right] & -\mathbf{E}\left[\frac{\partial^2 \ln p(\mathbf{y}; \mathbf{r}_s, \theta_s)}{\partial \mathbf{r}_s \partial \theta_s}\right] \\ -\mathbf{E}\left[\frac{\partial^2 \ln p(\mathbf{y}; \mathbf{r}_s, \theta_s)}{\partial \theta_s \partial \mathbf{r}_s}\right] & -\mathbf{E}\left[\frac{\partial^2 \ln p(\mathbf{y}; \mathbf{r}_s, \theta_s)}{\partial \theta_s^2}\right] \end{bmatrix} \quad (37)$$

For the particular case of a model of the form of equation (36) the FIM simplifies to [17]

$$\mathbf{I}(\mathbf{r}_s, \theta_s) = \begin{bmatrix} \left[\frac{\partial \Theta(\mathbf{r}_s, \theta_s)}{\partial \mathbf{r}_s}\right]^T \Sigma^{-1} \left[\frac{\partial \Theta(\mathbf{r}_s, \theta_s)}{\partial \mathbf{r}_s}\right] & \left[\frac{\partial \Theta(\mathbf{r}_s, \theta_s)}{\partial \mathbf{r}_s}\right]^T \Sigma^{-1} \left[\frac{\partial \Theta(\mathbf{r}_s, \theta_s)}{\partial \theta_s}\right] \\ \left[\frac{\partial \Theta(\mathbf{r}_s, \theta_s)}{\partial \theta_s}\right]^T \Sigma^{-1} \left[\frac{\partial \Theta(\mathbf{r}_s, \theta_s)}{\partial \mathbf{r}_s}\right] & \left[\frac{\partial \Theta(\mathbf{r}_s, \theta_s)}{\partial \theta_s}\right]^T \Sigma^{-1} \left[\frac{\partial \Theta(\mathbf{r}_s, \theta_s)}{\partial \theta_s}\right] \end{bmatrix} \quad (38)$$

and $\Sigma^{-1} = \text{diag}(\frac{1}{\sigma_1^2}, \dots, \frac{1}{\sigma_M^2})$. The individual elements of $\mathbf{I}(\mathbf{r}_s, \theta_s)$ in equation (38) can be written in terms of the sensor elements as

$$\mathbf{I}(\mathbf{r}_s, \theta_s)_{1,1} = \sum_{i=1}^M \frac{1}{\sigma_i^2} \frac{\partial \Theta(i; \mathbf{r}_s, \theta_s)}{\partial \mathbf{r}_s} \frac{\partial \Theta(i; \mathbf{r}_s, \theta_s)}{\partial \mathbf{r}_s} \quad (39)$$

$$\mathbf{I}(\mathbf{r}_s, \theta_s)_{1,2} = \sum_{i=1}^M \frac{1}{\sigma_i^2} \frac{\partial \Theta(i; \mathbf{r}_s, \theta_s)}{\partial \mathbf{r}_s} \frac{\partial \Theta(i; \mathbf{r}_s, \theta_s)}{\partial \theta_s} \quad (40)$$

$$\mathbf{I}(\mathbf{r}_s, \theta_s)_{2,1} = \sum_{i=1}^M \frac{1}{\sigma_i^2} \frac{\partial \Theta(i; \mathbf{r}_s, \theta_s)}{\partial \theta_s} \frac{\partial \Theta(i; \mathbf{r}_s, \theta_s)}{\partial \mathbf{r}_s} \quad (41)$$

$$\mathbf{I}(\mathbf{r}_s, \theta_s)_{2,2} = \sum_{i=1}^M \frac{1}{\sigma_i^2} \frac{\partial \Theta(i; \mathbf{r}_s, \theta_s)}{\partial \theta_s} \frac{\partial \Theta(i; \mathbf{r}_s, \theta_s)}{\partial \theta_s} \quad (42)$$

This requires that the partial derivatives of equation (23) with respect to the location parameters (r_s, θ_s) be evaluated

$$\frac{\partial \Theta(i; \mathbf{r}_s, \theta_s)}{\partial r_s} = \frac{-\left(-\frac{\sin \theta_s}{\sqrt{x^2 - 2r_s x \sin \theta_s + r_s^2}} - \frac{(x - r_s \sin \theta_s)(-2x \sin \theta_s + 2r_s)}{2(x^2 - 2r_s x \sin \theta_s + r_s^2)^{3/2}}\right)}{\sqrt{1 - \frac{(x - r_s \sin \theta_s)^2}{x^2 - 2r_s x \sin \theta_s + r_s^2}}} \quad (43)$$

and

$$\frac{\partial \Theta(i; \mathbf{r}_s, \theta_s)}{\partial \theta_s} = \frac{-\left(-\frac{r_s \cos \theta_s}{\sqrt{x^2 - 2r_s x \sin \theta_s + r_s^2}} + \frac{(x - r_s \sin \theta_s)r_s x \cos \theta_s}{(x^2 - 2r_s x \sin \theta_s + r_s^2)^{3/2}}\right)}{\sqrt{1 - \frac{(x - r_s \sin \theta_s)^2}{x^2 - 2r_s x \sin \theta_s + r_s^2}}} \quad (44)$$

with $x = d \cdot [(i-1) - \frac{M-1}{2}]$ for $i \in \{1, \dots, M\}$ (as in equation (18)). Let equation (37) be re-written as

$$\mathbf{I}(\mathbf{r}_s, \theta_s) = \begin{bmatrix} \mathbf{I}(\mathbf{r}_s, \theta_s)_{1,1} & \mathbf{I}(\mathbf{r}_s, \theta_s)_{1,2} \\ \mathbf{I}(\mathbf{r}_s, \theta_s)_{2,1} & \mathbf{I}(\mathbf{r}_s, \theta_s)_{2,2} \end{bmatrix} \quad (45)$$

where the individual elements are determined using equations (43) and (44), evaluated at a particular (r_s, θ_s) of interest, substituted into equations (39) through (42), where the σ_i^2 are the variance of the angle measurement at each sensor. The Cramer-Rao lower bounds for estimates of r_s and θ_s are, respectively

$$\text{var}(\hat{r}_s) \geq \frac{\mathbf{I}(\mathbf{r}_s, \theta_s)_{2,2}}{[\mathbf{I}(\mathbf{r}_s, \theta_s)_{1,1} \cdot \mathbf{I}(\mathbf{r}_s, \theta_s)_{2,2} - \mathbf{I}(\mathbf{r}_s, \theta_s)_{1,2} \cdot \mathbf{I}(\mathbf{r}_s, \theta_s)_{2,1}]} \quad (46)$$

and

$$\text{var}(\hat{\theta}_s) \geq \frac{\mathbf{I}(\mathbf{r}_s, \theta_s)_{1,1}}{[\mathbf{I}(\mathbf{r}_s, \theta_s)_{1,1} \cdot \mathbf{I}(\mathbf{r}_s, \theta_s)_{2,2} - \mathbf{I}(\mathbf{r}_s, \theta_s)_{1,2} \cdot \mathbf{I}(\mathbf{r}_s, \theta_s)_{2,1}]} \quad (47)$$

The CRLB is a function of the source location. For one particular array configuration and sensor-angle estimate variance at each sensor, the variation of CRLB for source location over a grid of possible source locations is shown in figures 2 and 3.

V. Implementation

A. Alias-Free SAD

In practice, implementing the SAD directly using the previous definition has proven undesirable. This can be seen by rewriting equation (12) as

$$\mathbf{T}_k(\mathbf{i}, \theta; \mathbf{z}_k) = \mathcal{F}[\mathbf{K}_{\mathbf{z}_k}(\mathbf{i}, l) * \phi(\mathbf{i}, l)] \quad (48)$$

where

$$K_{\mathbf{z}_k}(i, l) = \mathbf{z}_k(\mathbf{i} + l)\mathbf{z}_k^*(\mathbf{i} - l) \quad (49)$$

(\mathcal{F} denotes Fourier transform in the variable $l \rightarrow \theta$ and $*$ denotes convolution in the variable i .) The sensor position (index i) dependent lag (index l) sequence, $K_{\mathbf{z}_k}(i, l)$, is evaluated at even lag intervals only (i.e. where the lag spacing between sensors is even). This under-samples the true position dependent lag sequence and causes aliasing in the resulting SAD for many source locations.

It is possible to correct the aliasing problem by oversampling the spatial signal by two (i.e. space the sensors by $d = \frac{\lambda}{4}$) or by interpolating the $d = \frac{\lambda}{2}$ sampled spatial signal. Oversampling is frequently impractical as it doubles the cost of the array. Interpolation is also undesirable because sensor arrays frequently have a limited number of sensors (M) and the array “end” effects associated with interpolating the finite extent spatial signal corrupt the resulting SAD.

A more satisfactory approach is to exploit the results of Jeong and Williams [18]. By rotating the domain of $K_{\mathbf{z}_k}(i, l)$ and $\phi(i, l)$ by -45° it is possible to construct values in $\phi(i, l)$ corresponding

to odd interval lags in $K_{\mathbf{z}_k}(i, l)$. Let

$$K'_{\mathbf{z}_k}(i_1, i_2) = \mathbf{z}_k(\mathbf{i}_1) \mathbf{z}_k^*(\mathbf{i}_2) \quad (50)$$

and

$$\phi'(i_1, i_2) = \phi\left(\frac{m+l}{2}, \frac{m-l}{2}\right) \quad (51)$$

for sensors i_1 and i_2 . The rotated $K'_{\mathbf{z}_k}$ contains the $|i_1 - i_2| \in \{\dots, -2, 0, 2, \dots\}$ lag values corresponding to the even lags determined in equation (49). It also, however, contains the missing odd lag samples ($|i_1 - i_2| \in \{\dots, -3, -1, 1, 3, \dots\}$) required to avoid aliasing. Similarly, the kernel $\phi'(i_1, i_2)$ is evaluated on the rotated (i_1, i_2) domain and likewise provides support for the missing odd interval lag values. These values may be interpolated from the even lag kernel samples, or, exactly computed from the definition of the kernel sequence. Note that the rotated kernel $\phi'(i_1, i_2)$ has a larger extent than prior to rotation. Using this approach it is possible to compute an approximately alias-free SAD [19].

B. Quadratic SAD

Cunningham and Williams [20], and Amin [21], have shown (in the context of time-frequency distributions) that it is possible to express $\mathbf{T}_k(\mathbf{i}, \theta; \mathbf{z}_k)$ in quadratic form as a weighted sum of spatial beamformers. Let the eigen-decomposition of the rotated (or alias-free, see equation (51)) kernel be given as

$$\phi'(i_1, i_2) = \mathbf{V} \Sigma \mathbf{V}^H \quad (52)$$

where the columns \mathbf{v}_j (for $j \in \{0, \dots, J-1\}$) of \mathbf{V} are the J eigenvectors of ϕ' and the diagonal entries of matrix Σ are the corresponding eigenvalues, $\sigma_0, \dots, \sigma_{J-1}$. Due to the use of the rotated kernel $\phi'(i_1, i_2)$, $J = 4L + 1$, for a given maximum lag extent L in the non-rotated cone-shaped kernel $\phi(m, l)$. The SAD may be written as

$$\mathbf{T}_k(\mathbf{i}, \theta; \mathbf{z}_k) = \sum_{j=0}^{J-1} \sigma_j |\mathbf{v}_j \cdot \mathbf{z}_{k,i}|^2 \quad (53)$$

where $\mathbf{z}_{k,i}$ is the (possibly zero extended) spatial sequence surrounding sensor i for the k^{th} snapshot. Due to the rapid drop in the eigenvalues of commonly used kernels, $\mathbf{T}_k(\mathbf{i}, \theta; \mathbf{z}_k)$ can be well approximated as $\tilde{\mathbf{T}}_k(\mathbf{i}, \theta; \mathbf{z}_k)$ by using few terms J' ($J' < J$) in equation (53). This approximation is discussed fully in [21].

Equation (53) can be interpreted in the context of classical beamforming using subarrays. A subarray beamformer constructs multiple sub-beams using classical beamforming applied to

subsets of sensor elements in the array. Typically, the sensors in a subarray are adjacent. The sensors corresponding to adjacent subarrays may or may not overlap within the full array. A given subarray beamformer estimates the spatial spectrum local to the position of the subarray within the full array.

At each sensor index i , equation (53) is a weighted sum of multiple beamformers evaluated using the same spatial signal $\mathbf{z}_{\mathbf{k},i}$ surrounding sensor i (which may include the case where the full spatial signal $\mathbf{z}_{\mathbf{k}}$ is used). This weighted sum at sensor i is a representation of the spatial spectrum at sensor i (i.e. the SAD). It has similar form to a classical subarray beamformer, although differs in two distinct ways. Up to J beamformers are determined at each sensor (not one) and the structure of the beamformer weights and the combining ratios are prescribed by the SAD kernel ϕ' . It is important to note that the J' subarray beamformers can be applied to J' consecutive snapshots, providing that the source maintains its signal value over J' samples. A source with constant modulus property will naturally satisfy this condition. This flexibility does not exist in a typical application of time-frequency analysis. A deviation from the constant-modulus property has the effect of changing the eigen-decomposition by scaling the eigenvalues in equation (53). We should note that a change in the signal phase does not alter the magnitude squares of equation (53). The ability to apply each term of the approximation in equation (53) to a different snapshot, instead of the same data vector, reduces computational time and hardware requirements.

VI. Simulations

In this section, we demonstrate the proposed approach for near-field scatter characterization. Consider a 64 sensor linear equi-spaced array operating at a carrier frequency of 6.14MHz ($\lambda = 46.8\text{m}$) with 15m spacing between sensors. The local scatterer distribution comprises a point scatterer in the near-field at range 1200m and angle -30° , from the array center (the array has total length 945m). Assume the test source angle is 20° with respect to boresight and that the test source is temporally stationary and coherent with and 26dB stronger power than the scattered source. In this example we have used the Wigner distribution so that the kernel in (12) is $\delta(m)$. Of course, other members of Cohen's class may also be used.

Figure 4 shows the SAD for the received data. The plot shows the received power (plot intensity) as a function of angle (spatial frequency) on the vertical axis and sensor position within the array on the horizontal axis. The spatial frequency axis extends beyond the interval ± 1 since the sensors are spaced more closely than $\frac{\lambda}{2}$. The SAD is dominated by the substantially more powerful far-field test source and there is no clear indication of any additional scattering. The far-field source has the same angle for every sensor, and therefore, depicts a horizontal signature in the s - a domain. In figure 5, we have applied the orthogonal projection operator to

the received sensor data and computed the SAD for \mathbf{Pz}_k , as per equations (15) and (16). The SAD now clearly shows the presence of near-field local scatter. In this case, the location of the near field source is far enough from the array for the quadratic phase approximation used by Breed and Posch to be valid (i.e. the sensor v. angle relationship is approximately linear).

The beampatterns, computed using a 70dB Taylor window, for the cases of \mathbf{z}_k and \mathbf{Pz}_k are shown in figure 6. From the plots, the presence of near-field scatter cannot be confirmed as compared with alternative explanations for the distorted beampatterns, such as poor array calibration.

Now we wish to demonstrate the use of the alias-free summed beamformer SAD described in equation (53). Again the simulations assume a 64 element linear equi-spaced array, with operating frequency and sensor spacing as before.

In the first simulation, a far-field source was placed at angle 30° (all angles are with respect to array boresight) and a near-field source placed at a range of 100m and an angle of -40° . The Choi-Williams SAD ($\sigma=100$) implemented using the alias-free rotated kernel form is shown in figure 7. Signals apparently arriving from spatial frequencies greater than 1 or less than -1 do not correspond to real signals. The crosses marked on the figure indicate the true angles of each source at every sensor.

The weighted summed beamformer implementation of the Choi-Williams SAD described in equation (53) has been computed for the same scenario as in figure 7. The result is shown in figure 8 for the case where $J'=25$ and $J=65$ (i.e. 25 beamformers have been retained out of a possible total of 65). Note that visually, there is no apparent loss of fidelity using the approximate SAD. This implementation has substantially lower computational complexity.

The simulation results shown in figures 9 and 10 are for the case of two near-field sources. In figure 9, one source is placed at a range of 300m and an angle of 30° , whereas the second is at a range of 200m and an angle of -40° . The SAD is a Choi-Williams kernel implemented using weighted summed beamforming with $J'=25$ and $J=65$ (i.e. 25 of 65 retained). Note the presence of cross terms between the two source sensor-angle signatures. The Choi-Williams kernel is well known to perform poorly in terms of cross term suppression for the case when the underlying signals are other than close to parallel to either the sensor (time) axis or the angle (frequency) axis in the SAD (TFD).

The results presented in figure 10 again show the result of a SAD using a Choi-Williams kernel implemented with the 25 term weighted summed beamformer. There are two near-field sources and the source positions have been selected to be along the axis of the array. The first source is at 300m and 90° while the second is at 600m and -90° . The first source is embedded within the array and co-located exactly at a sensor position. The second source is beyond the lefthand

extent of the array. The first source has been localized at exactly the correct sensor within the array (at 300m from the array center). Near-field spreading loss ($1/r$) between sensors has caused the source intensity to drop dramatically at adjacent sensors. The corresponding dual time-frequency domain signature is that of an impulse. The second source is again correctly represented as being at -90° to the left end of the array. Notice that the $1/r$ spreading loss for the near-field source means that the SAD has stronger intensity at the left end of the array. This is the degenerate near-field situation, where even though the source is in the near-field of the array, the angle to each sensor in the array is identical.

The simulations shown in figures 11 through 16 contrast the cases of point sources in the far and near-field and a spatially spread source in the far-field. Traditional beampatterns (computed using a 70dB Taylor weight) show that it may be difficult to discriminate between spatially spread far-field sources and a near-field point source. Using the SAD, one is clearly able to visually separate these cases (contrast figures 14 and 16). Note that the spatially spread source was generated using 20 realizations of a low pass noise process modulating the spatial steering vector corresponding to the mean angle for the spread source.

VII. Conclusions

We have proposed a new method for characterizing near-field scatter local to a receiving array. As part of the characterization, we have exploited and generalised the spatial Wigner distribution proposed by Breed and Posch, although we have renamed it the sensor angle distribution to avoid confusion with a similarly named but differently defined spatial time-frequency distribution. An orthogonal projection operator derived from the steering vector for the far-field test source is used to exclude the direct propagation path from the test source in the characterization.

This paper has addressed several issues concerning the use of the Sensor-Angle Distribution (SAD) as a tool for characterizing near-field scatter environments.

An expression has been derived describing the angle to a source or scatter site from each sensor in an array. Formulas are given for least squares, and, under certain conditions, maximum likelihood estimates of source location based on source angle measurements such as those obtained from a SAD.

The use of a rotated smoothing kernel has proven effective at overcoming aliasing in the SAD caused by the spatial frequencies obtained for realistically positioned sources.

An approximate method for implementing the SAD has been found to have a direct interpretation in terms of a multiple subarray beamformer. However, the weighting functions applied to the beamformer, and the fact that more than one beamformer is combined to construct the final spatial spectrum at each sensor is an extension of present subarray concepts.

The SAD presented in this paper assumed the use of a data-independent sensor-angle kernel,

as reflected in equation (12). It is important to note that data-dependent kernels can also be employed in the SAD. Positive time-frequency distributions [22], optimum time-frequency kernels [23], and the time-frequency reassignment method [24] can all be cast in terms of the two new variables, sensor and angle, leading to potential improvements over equation (12) in resolution and cross-term suppression.

VIII. Acknowledgements

This work is supported by the Australian Defense Science and Technology Organization, under the Defence Science Fellowship program, and the US Office of Naval Research, Grant No. N00014-98-1-0176.

Appendix

I. Cramer-Rao Bound for Location from Sensor Measurements

Consider the received signal model

$$\mathbf{z}_k = \mathbf{a} \cdot \mathbf{s}_k + \mathbf{w}_k \quad (54)$$

where k is the array snapshot index. For the case of a single near-field source at (r_s, θ_s) then \mathbf{s}_k is a scalar s_k and \mathbf{a} is given by equation (8). Let the total number of snapshots be N with the index $k \in \{1, \dots, N\}$. The noise is additive Gaussian noise where $\mathbf{w}_k = [\mathbf{w}_1, \dots, \mathbf{w}_M]_k^T$ which for all received snapshots can be written $\mathbf{W} = [\mathbf{w}_1, \dots, \mathbf{w}_N]$. The noise is characterized by $\mathbf{E}[\mathbf{w}_{i,k} \mathbf{w}_{i',k'}^*] = \sigma_{i,k}^2 \delta_{i-i'} \delta_{k-k'} = \sigma_i^2$, or, more completely $w_{i,k} \sim \mathcal{N}(0, \sigma_i^2)$. In this case the variance of i^{th} sensor may be different for each sensor i , but remains the same over all snapshots for a given sensor. Let $\mathbf{Z} = [\mathbf{z}_1, \dots, \mathbf{z}_N]$ be the data matrix of all received data. Let $\mathbf{s} = [s_1, \dots, s_N]$ be the deterministic source signal characterized only by the vector \mathbf{s} . Equation (54) can be re-written as

$$\mathbf{Z} = \mathbf{a}(r_s, \theta_s) \cdot \mathbf{s} + \mathbf{W} \quad (55)$$

which has unknown parameters (r_s, θ_s) and nuisance parameter \mathbf{s} (which increases in dimension as N increases).

The likelihood function for this model is

$$p(\mathbf{Z}; \mathbf{r}_s, \theta_s, \mathbf{s}) = \prod_{k=1}^N p(\mathbf{z}_k; \mathbf{r}_s, \theta_s, s_k) \quad (56)$$

with

$$p(\mathbf{z}_k; \mathbf{r}_s, \theta_s, s_k) = \prod_{i=1}^M \frac{1}{\sqrt{2\pi\sigma_i^2}} \exp\left(-\frac{1}{2\sigma_i^2} [z_{i,k} - \mathbf{a}_i(r_s, \theta_s) \cdot \mathbf{s}_k]^2\right) \quad (57)$$

hence

$$p(\mathbf{Z}; \mathbf{r}_s, \theta_s, \mathbf{s}) = \prod_{k=1}^N \left[\prod_{i=1}^M \frac{1}{\sqrt{2\pi\sigma_i^2}} \exp \left(-\frac{1}{2\sigma_i^2} [\mathbf{z}_{i,k} - \mathbf{a}_i(\mathbf{r}_s, \theta_s) \cdot \mathbf{s}_k]^2 \right) \right] \quad (58)$$

with the log-likelihood given by

$$\ln p(\mathbf{Z}; \mathbf{r}_s, \theta_s, \mathbf{s}) = -N \sum_{i=1}^M \ln[\sqrt{2\pi}\sigma_i] - N \sum_{i=1}^M \left[\frac{1}{2\sigma_i^2} [\mathbf{z}_{i,k} - \mathbf{a}_i(\mathbf{r}_s, \theta_s) \cdot \mathbf{s}_k]^2 \right] \quad (59)$$

The FIM is constructed from the partial derivatives of $\mathbf{a}_i(\mathbf{r}_s, \theta_s) \cdot \mathbf{s}_k$ with respect to r_s , θ_s and s_k . Let

$$y_{i,k} = \mathbf{a}_i(\mathbf{r}_s, \theta_s) \cdot \mathbf{s}_k \quad (60)$$

or

$$y_{i,k} = \frac{s_k}{r_{s,i}} \cdot e^{-j\frac{2\pi}{\lambda} r_{s,i}} \quad (61)$$

Inserting the $r_{i,s}$ gives

$$y_{i,k} = \frac{s_k}{\sqrt{x^2 - 2r_s x \sin \theta_s + r_s^2}} \cdot e^{-j\frac{2\pi}{\lambda} \sqrt{x^2 - 2r_s x \sin \theta_s + r_s^2}} \quad (62)$$

where x at each sensor position is

$$x = d \cdot \left[(i-1) - \frac{M-1}{2} \right] \text{ for } i \in \{1, \dots, M\} \quad (63)$$

The partial derivatives are (in terms of x to improve clarity)

$$\frac{\partial y_{i,k}}{\partial r_s} = \frac{s_k \cdot e^{-j\frac{2\pi}{\lambda} \sqrt{x^2 - 2r_s x \sin \theta_s + r_s^2}}}{x^2 - 2r_s x \sin \theta_s + r_s^2} \cdot [-x \sin \theta_s + r_s] \cdot \left[\frac{-1}{\sqrt{x^2 - 2r_s x \sin \theta_s + r_s^2}} - j\frac{2\pi}{\lambda} \right] \quad (64)$$

$$\frac{\partial y_{i,k}}{\partial \theta_s} = \frac{s_k \cdot e^{-j\frac{2\pi}{\lambda} \sqrt{x^2 - 2r_s x \sin \theta_s + r_s^2}}}{x^2 - 2r_s x \sin \theta_s + r_s^2} \cdot [r_s x \cos \theta_s] \cdot \left[\frac{1}{\sqrt{x^2 - 2r_s x \sin \theta_s + r_s^2}} + j\frac{2\pi}{\lambda} \right] \quad (65)$$

$$\frac{\partial y_{i,k}}{\partial s_k} = \frac{1}{\sqrt{x^2 - 2r_s x \sin \theta_s + r_s^2}} \cdot e^{-j\frac{2\pi}{\lambda} \sqrt{x^2 - 2r_s x \sin \theta_s + r_s^2}} \quad (66)$$

For the case of $k = 1$ (i.e. the single snapshot case), the individual elements of the FIM are

$$\mathbf{I}(\mathbf{r}_s, \theta_s, \mathbf{s}_k) = \begin{bmatrix} \sum_{i=1}^M \frac{1}{\sigma_i^2} \frac{\partial y_{i,k}}{\partial r_s} \frac{\partial y_{i,k}}{\partial r_s} & \sum_{i=1}^M \frac{1}{\sigma_i^2} \frac{\partial y_{i,k}}{\partial r_s} \frac{\partial y_{i,k}}{\partial \theta_s} & \sum_{i=1}^M \frac{1}{\sigma_i^2} \frac{\partial y_{i,k}}{\partial r_s} \frac{\partial y_{i,k}}{\partial s_k} \\ \sum_{i=1}^M \frac{1}{\sigma_i^2} \frac{\partial y_{i,k}}{\partial \theta_s} \frac{\partial y_{i,k}}{\partial r_s} & \sum_{i=1}^M \frac{1}{\sigma_i^2} \frac{\partial y_{i,k}}{\partial \theta_s} \frac{\partial y_{i,k}}{\partial \theta_s} & \sum_{i=1}^M \frac{1}{\sigma_i^2} \frac{\partial y_{i,k}}{\partial \theta_s} \frac{\partial y_{i,k}}{\partial s_k} \\ \sum_{i=1}^M \frac{1}{\sigma_i^2} \frac{\partial y_{i,k}}{\partial s_k} \frac{\partial y_{i,k}}{\partial r_s} & \sum_{i=1}^M \frac{1}{\sigma_i^2} \frac{\partial y_{i,k}}{\partial s_k} \frac{\partial y_{i,k}}{\partial \theta_s} & \sum_{i=1}^M \frac{1}{\sigma_i^2} \frac{\partial y_{i,k}}{\partial s_k} \frac{\partial y_{i,k}}{\partial s_k} \end{bmatrix} \quad (67)$$

The CRLB for each of the unknown parameters is determined from the inverse of equation (67) evaluated using equations (64) through (66) at the true values of the unknown parameter.

$$\text{var}(r_s) \geq [\mathbf{I}(\mathbf{r}_s, \theta_s, \mathbf{s}_k)]_{1,1}^{-1} \quad (68)$$

$$\text{var}(\theta_s) \geq [\mathbf{I}(\mathbf{r}_s, \theta_s, \mathbf{s}_k)]_{2,2}^{-1} \quad (69)$$

$$\text{var}(s_k) \geq [\mathbf{I}(\mathbf{r}_s, \theta_s, \mathbf{s}_k)]_{3,3}^{-1} \quad (70)$$

Appendix

I. Cramer-Rao Bound for Location from Sensor Phase Measurements

Consider the case where only the phase of the received signal is recorded at each sensor. In this case equation (61) becomes

$$y_{i,k} = e^{-j\frac{2\pi}{\lambda}r_{s,i}} \quad (71)$$

where, as before, substituting in $r_{i,s}$ gives

$$y_{i,k} = e^{-j\frac{2\pi}{\lambda}\sqrt{x^2 - 2r_s x \sin \theta_s + r_s^2}} \quad (72)$$

The partial derivatives of the two remaining unknown parameters (r_s, θ_s) are (in terms of sensor location x)

$$\frac{\partial y_{i,k}}{\partial r_s} = -j\frac{2\pi}{\lambda} \left[\frac{-x \sin \theta_s + r_s}{\sqrt{x^2 - 2r_s x \sin \theta_s + r_s^2}} \right] e^{-j\frac{2\pi}{\lambda}\sqrt{x^2 - 2r_s x \sin \theta_s + r_s^2}} \quad (73)$$

$$\frac{\partial y_{i,k}}{\partial \theta_s} = j\frac{2\pi}{\lambda} \left[\frac{r_s x \cos \theta_s}{\sqrt{x^2 - 2r_s x \sin \theta_s + r_s^2}} \right] e^{-j\frac{2\pi}{\lambda}\sqrt{x^2 - 2r_s x \sin \theta_s + r_s^2}} \quad (74)$$

The elements of the FIM are then

$$\mathbf{I}(\mathbf{r}_s, \theta_s)_{1,1} = \sum_{i=1}^M \frac{1}{\sigma_i^2} \frac{\partial y_{i,k}}{\partial r_s} \frac{\partial y_{i,k}}{\partial r_s} \quad (75)$$

$$\mathbf{I}(\mathbf{r}_s, \theta_s)_{1,2} = \sum_{i=1}^M \frac{1}{\sigma_i^2} \frac{\partial y_{i,k}}{\partial r_s} \frac{\partial y_{i,k}}{\partial \theta_s} \quad (76)$$

$$\mathbf{I}(\mathbf{r}_s, \theta_s)_{2,1} = \sum_{i=1}^M \frac{1}{\sigma_i^2} \frac{\partial y_{i,k}}{\partial \theta_s} \frac{\partial y_{i,k}}{\partial r_s} \quad (77)$$

$$\mathbf{I}(\mathbf{r}_s, \theta_s)_{2,2} = \sum_{i=1}^M \frac{1}{\sigma_i^2} \frac{\partial y_{i,k}}{\partial \theta_s} \frac{\partial y_{i,k}}{\partial \theta_s} \quad (78)$$

The Cramer-Rao lower bounds for estimates of r_s and θ_s based on phase only measurements at each sensor in the array, are, respectively

$$\text{var}(\hat{r}_s) \geq \frac{\mathbf{I}(\mathbf{r}_s, \theta_s)_{2,2}}{[\mathbf{I}(\mathbf{r}_s, \theta_s)_{1,1} \cdot \mathbf{I}(\mathbf{r}_s, \theta_s)_{2,2} - \mathbf{I}(\mathbf{r}_s, \theta_s)_{1,2} \cdot \mathbf{I}(\mathbf{r}_s, \theta_s)_{2,1}]} \quad (79)$$

and

$$\text{var}(\hat{\theta}_s) \geq \frac{\mathbf{I}(\mathbf{r}_s, \theta_s)_{1,1}}{[\mathbf{I}(\mathbf{r}_s, \theta_s)_{1,1} \cdot \mathbf{I}(\mathbf{r}_s, \theta_s)_{2,2} - \mathbf{I}(\mathbf{r}_s, \theta_s)_{1,2} \cdot \mathbf{I}(\mathbf{r}_s, \theta_s)_{2,1}]} \quad (80)$$

References

- [1] G. J. Frazer and Y. I. Abramovich, "Quantifying multi-channel receiver calibration," in *Second IEEE Sensor and Multichannel Signal Processing Workshop*, Rosslyn, VA, USA, August 2002.
- [2] B. R. Breed and T. E. Posch, "A range and azimuth estimator based on forming the spatial Wigner distribution," in *Proceedings of ICASSP 84*, 1984, pp. 41B.9.1–41B.9.2.
- [3] A. L. Swindlehurst and T. Kailath, "Near-field source parameter estimation using a spatial Wigner distribution approach," in *Advanced Algorithms and Architectures for Signal Processing III*. SPIE, 1988, vol. 975, pp. 86–92.
- [4] A. Belouchrani and M. G. Amin, "Blind source separation based on time-frequency signal representations," *IEEE Transactions on Signal Processing*, vol. 46, no. 11, pp. 2888–2897, November 1998.
- [5] M. G. Amin, "Spatial time-frequency distributions for direction finding and blind source separation," in *Proceedings of SPIE on Aerospace/Defense Sensing, Simulation, and Controls, Wavelet Conference*, Orlando, FL, April 1999.
- [6] D. Astely and B. Ottersten, "The effects of local scattering on direction of arrival estimation with MUSIC," *IEEE Transactions on Signal Processing*, vol. 47, no. 12, pp. 3220–3234, December 1999.
- [7] Y. D. Huang and M. Barkat, "Near-field multiple source localization by passive sensor array," *IEEE Transactions on Antennas and Propagation*, vol. 39, no. 7, pp. 968–975, July 1991.
- [8] S. Valaee, B. Champagne, and P. Kabal, "Parametric localization of distributed sources," *IEEE Transactions on Signal Processing*, vol. 43, no. 9, pp. 2144–2153, September 1995.
- [9] G. Fuks, J. Goldberg, and H. Messer, "Bearing estimation in a Ricean channel - Part I: Inherent accuracy limitations," *IEEE Transactions on Signal Processing*, vol. 49, no. 5, pp. 925–937, May 2001.
- [10] D. H. Johnson and D. E. Dudgeon, *Array Signal Processing: Concepts and Techniques*, Prentice-Hall Signal Processing Series. Prentice-Hall, 1993.
- [11] L. Cohen, *Time-Frequency Analysis*, Prentice-Hall, Englewood Cliffs, NJ, 1995.
- [12] B. Boashash, "Interpreting and estimating the instantaneous frequency of a signal - Part II: Algorithms," *Proceedings of the IEEE*, vol. 80, no. 4, pp. 539–569, April 1992.
- [13] B. Ristic and B. Boashash, "Instantaneous frequency estimation of quadratic and cubic FM signals using the cross polynomial Wigner-Ville distribution," *IEEE Transactions on Signal Processing*, vol. 44, no. 6, pp. 1549–1553, June 1996.
- [14] K. M. Wong and Q. Jin, "Estimation of the time-varying frequency of a signal: The Cramer-

Rao bound and the application of the Wigner distribution," *IEEE Transactions on Acoustics, Speech and Signal Processing*, vol. 38, no. 3, pp. 519–536, March 1990.

- [15] I. Djurovic and L. Stankovic, "Influence of high noise on the instantaneous frequency estimation using quadratic time-frequency distributions," *IEEE Signal Processing Letters*, vol. 7, no. 11, pp. 317–319, November 2000.
- [16] B. C. Lovell, R. C. Williamson, and B. Boashash, "The relationship between instantaneous frequency and time-frequency representations," *IEEE Transactions on Signal Processing*, vol. 41, no. 3, pp. 1458–1461, March 1993.
- [17] Steven M. Kay, *Fundamentals of Statistical Signal Processing: Estimation Theory*, Prentice Hall, NJ, USA, 1993.
- [18] J. Jeong and W. J. Williams, "Alias-free generalized discrete-time time frequency distributions," *IEEE Transactions on Signal Processing*, vol. 40, no. 11, pp. 2757–2765, November 1992.
- [19] A. H. Costa and G. Faye Boudreaux-Bartels, "An overview of aliasing errors in discrete-time formulations of time-frequency representations," *IEEE Transactions on Signal Processing*, vol. 47, no. 5, pp. 1463–1474, May 1999.
- [20] G. S. Cunningham and W. J. Williams, "Kernel decomposition of time-frequency distributions," *IEEE Transactions on Signal Processing*, vol. 42, no. 6, pp. 1425–1442, June 1994.
- [21] M. G. Amin, "Spectral decomposition of time-frequency distribution kernels," *IEEE Transactions on Signal Processing*, vol. 42, no. 5, pp. 1156–1165, May 1994.
- [22] P. J. Loughlin, J. W. Pitton, and L. E. Atlas, "Construction of positive time-frequency distributions," *IEEE Transactions on Signal Processing*, vol. 42, no. 10, pp. 2697–2705, October 1994.
- [23] D. L. Jones and R. G. Baraniuk, "An adaptive optimal-kernel time-frequency distribution," *IEEE Transactions on Signal Processing*, vol. 43, no. 10, pp. 2361–2371, October 1995.
- [24] F. Auger and P. Flandrin, "Improving the readability of time-frequency and time-scale representations by the reassignment method," *IEEE Transactions on Signal Processing*, vol. 43, no. 5, pp. 1068–1089, May 1995.

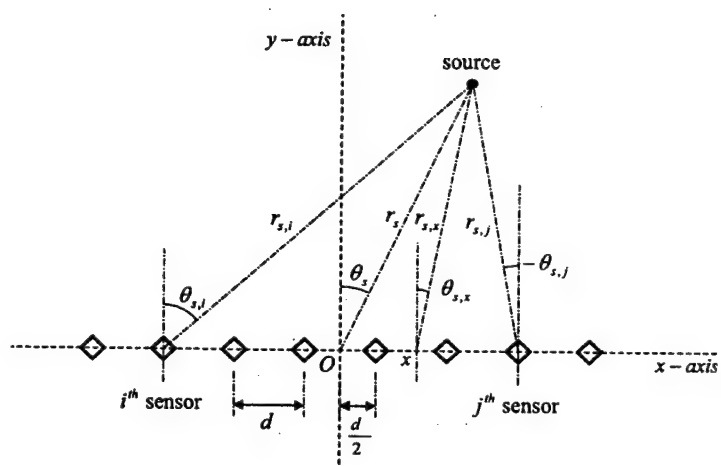


Fig. 1. Sensor array geometry and notations for a linear array and a near-field source.

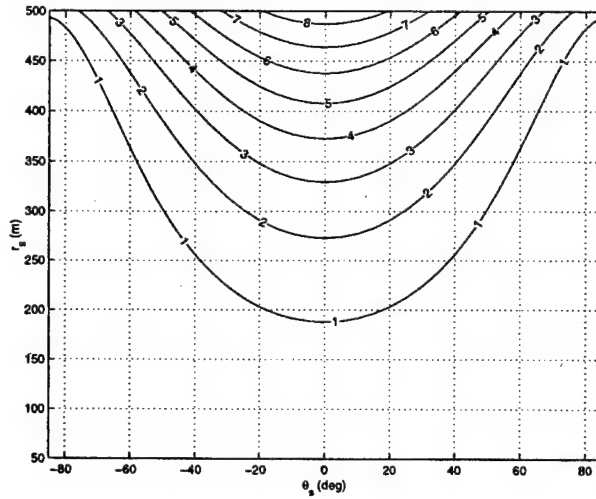


Fig. 2. CRLB (in m^2) of the range to a source, for various source locations, for the case of a 64 sensor linear array, spaced 15m between sensors. The sensor-angle is assumed to have been estimated at each sensor with a variance of 1 deg^2 .

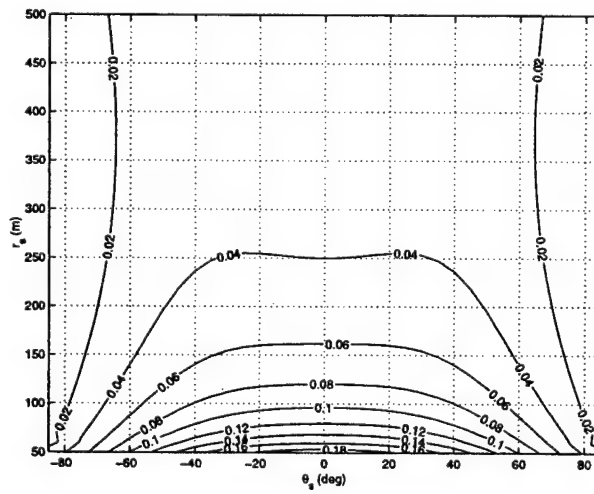


Fig. 3. CRLB (in deg^2) of the angle to a source, for various source locations, for the case of a 64 sensor linear array, spaced 15m between sensors. The sensor-angle is assumed to have been estimated at each sensor with a variance of 1 deg^2 .

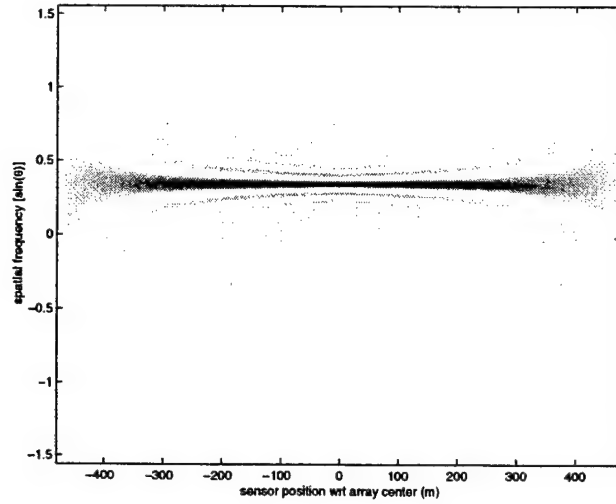


Fig. 4. SAD for the received sensor data \mathbf{z}_k . The far-field test source (at angle 20°) dominates the SAD characterization.

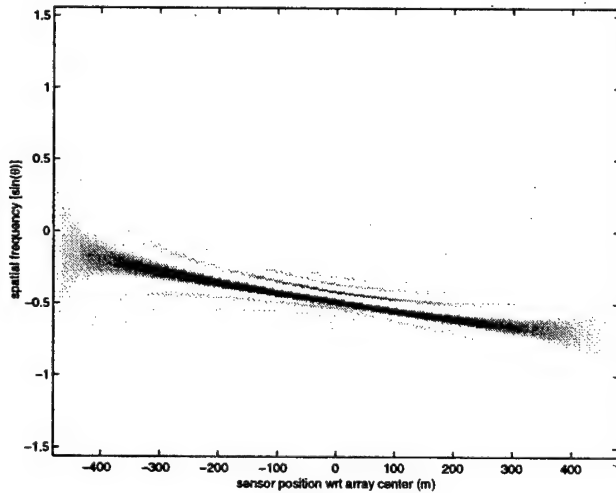


Fig. 5. SAD for the received data following application of the orthogonal projection operator, \mathbf{Pz}_k . With the direct propagation path from the far-field test signal removed by the orthogonal projection operator, the local scatterer spectrum is revealed. The local point scatterer is at a range of 1200m and angle of -30° .

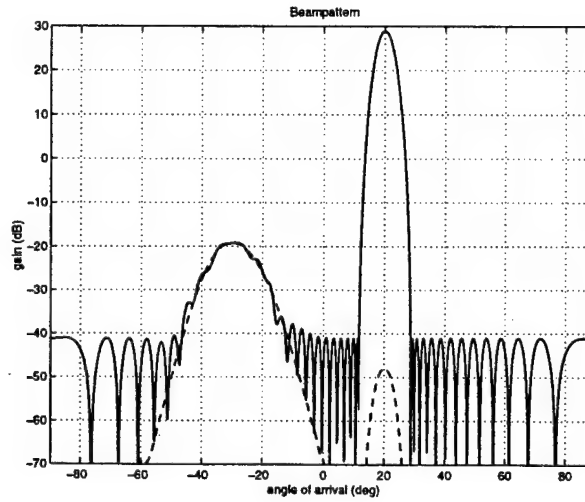


Fig. 6. Beampattern for z_k (—) and Pz_k (---). Without the sensor angle characterization it is not possible to identify perturbations from the ideal test source beampattern as being due to near-field scatter. For example, poor array calibration may be indistinguishable from local scatter.

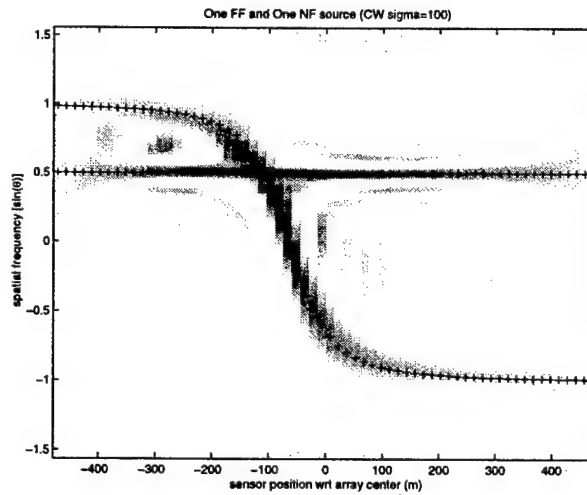


Fig. 7. Choi-Williams SAD for a far-field source at angle 30° and a near-field source at range 100m and angle -40° . True angles for each source at every sensor are marked by crosses.

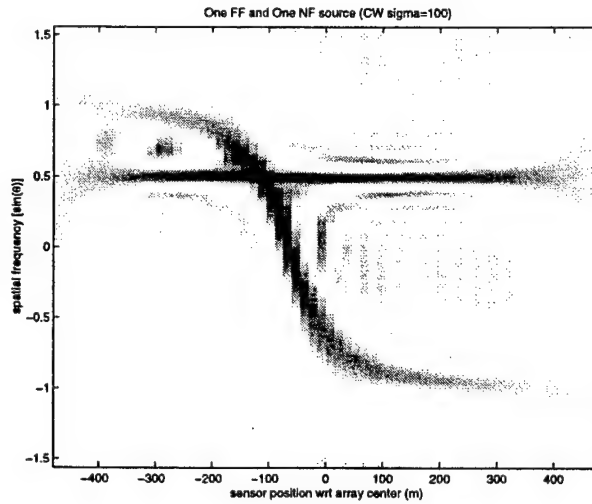


Fig. 8. Approximate weighted summed beamformer SAD for a far-field source at angle 30° and a near-field source at range 100m and angle -40° . In this case 25 of a possible 65 beamformers are summed together (see equation (53)).

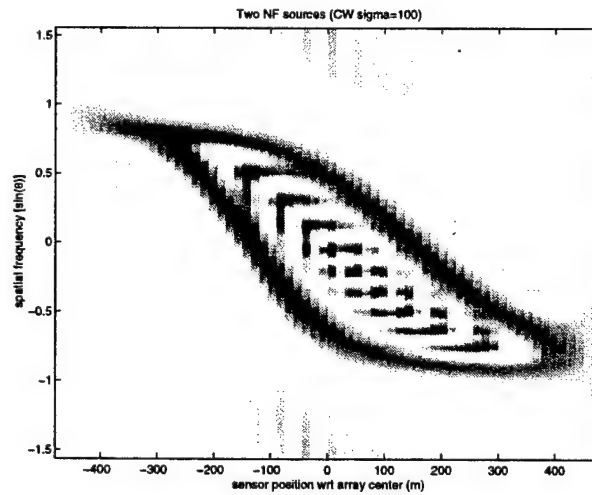


Fig. 9. Approximate weighted summed beamformer results for two near-field sources at 300m and 30° and 200m and -40° . 25 of a possible 65 beamformers are summed together.

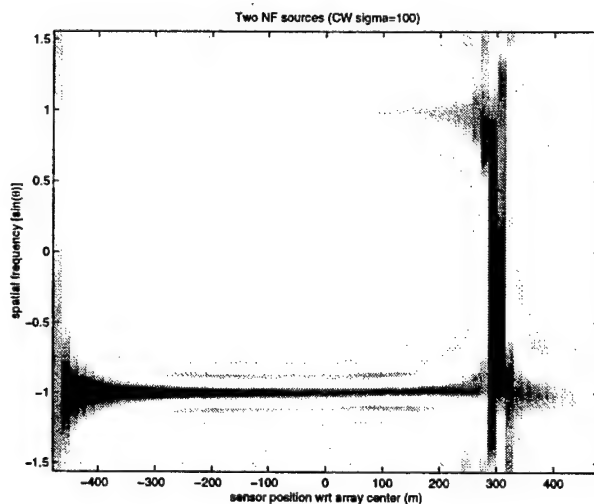


Fig. 10. Approximate weighted summed beamformer results for two near-field sources where the sources are aligned along the axis of the array at 600m and -90° and 300m and 90° .

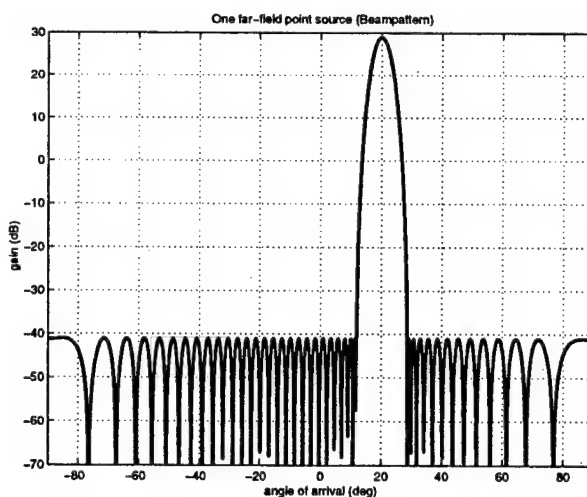


Fig. 11. Beampattern for a far-field point source at angle 20° .

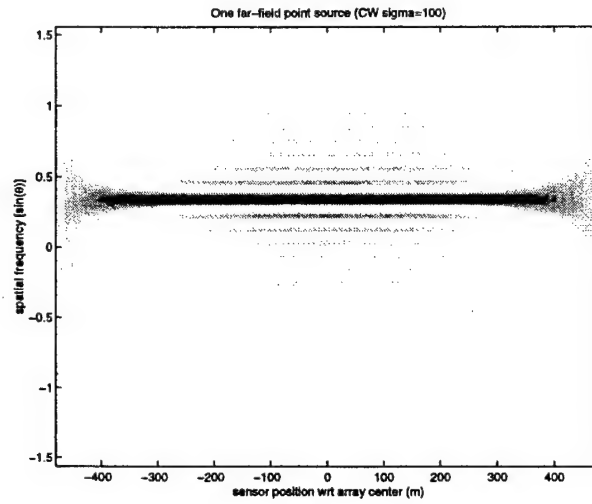


Fig. 12. Approximate weighted summed beamformer SAD ($J'=25$ and $J=65$) result for a far-field point source at angle 20° .

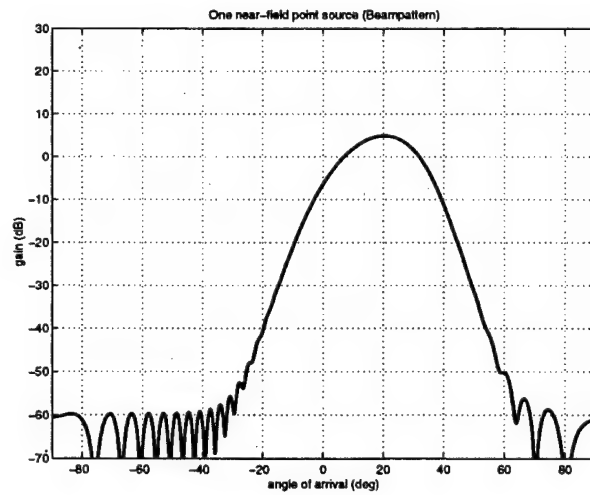


Fig. 13. Beampattern for a near-field point source at range 800m and angle 20° .

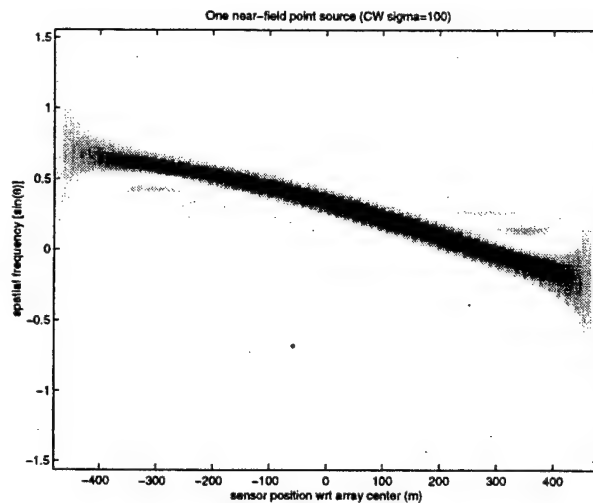


Fig. 14. Approximate weighted summed beamformer SAD (25 of 65) result for a near-field point source at range 800m and angle 20° .

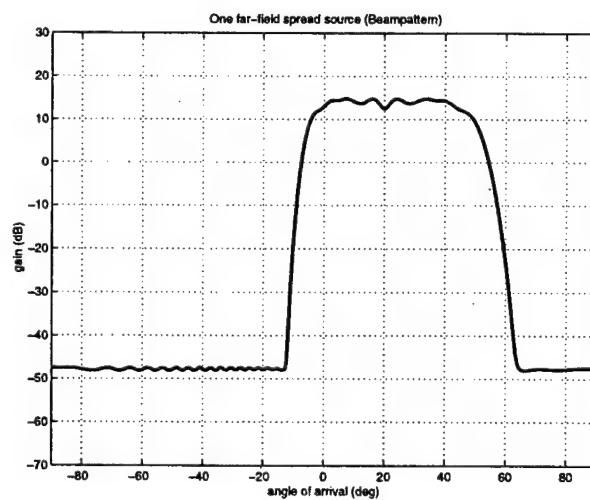


Fig. 15. Beampattern for a far-field spatially spread source with mean angle 20° .

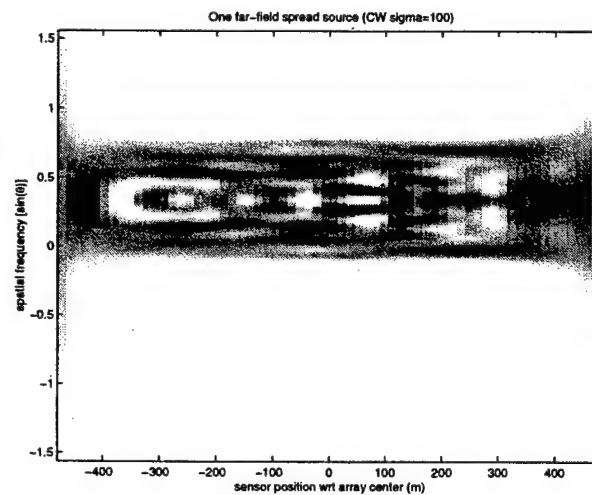


Fig. 16. Approximate weighted summed beamformer SAD (25 of 65) result for a far-field spatially spread source with mean angle 20° .

Improved Blind Separations of Nonstationary Sources Based on Spatial Time-Frequency Distributions

Yimin Zhang and Moeness G. Amin

Abstract

Blind source separation based on spatial time-frequency distributions (STFDs) provides improved performance over blind source separation methods based on second-order statistics, when dealing with nonstationary signals that are localizable in the time-frequency (t-f) domain. In the existing STFD methods, the covariance matrix is first used to whiten the data vector, then the mixing matrix and subsequently the source waveforms are estimated using STFD matrices constructed from the source t-f autoterm points. This letter improves the STFD-based source separation method by performing both whitening and estimation steps using the source t-f signatures. This modification provides robust performance to noise, and allows reduction of the number of sources considered for separation.

I. Introduction

Several narrowband blind source separation (BSS) methods have been proposed in the literature [1], [2], [3], [4]. Generally, blind source separations for independent sources are performed based on the employment of at least two different sets of matrices that span the same signal subspace. One matrix is used for whitening purpose, while others are jointly used to estimate the spatial signatures and source waveforms impinging on a multi-antenna receiver. Covariance matrices with different time lags, or cumulants matrices with different orders are typically used for the above purpose.

Nonstationary signals are frequently encountered in radar, sonar, and acoustic applications [5], [6]. For nonstationary signals, time-frequency distributions (TFDs) have been recently employed for array processing and found successful in blind separations of nonstationary signals [7], [8], [9], [10], [11], [12]. These methods are particularly effective when the signals are highly localized in the time-frequency (t-f) domain. In these methods, while the spatial time-frequency distribution (STFD) matrices are used for source diagonalization and anti-diagonalization, the whitening matrix remains the signal covariance matrix. The STFD matrices are constructed from the auto-TFDs and cross-TFDs of the sensor data and evaluated at different points of high signal-to-noise ratio (SNR) pertaining to the t-f signatures of the sources. Although this method improves the performance over that based on solely the covariance matrices, yet it does not fully utilize all inherent advantages of STFD.

This letter modifies the existing STFD-based BSS methods by performing whitening using an averaged STFD matrix over the source t-f signatures and, as such, making use of the t-f localization properties of the sources in both the whitening step and joint estimation step of the source separation procedure.

Employing the STFD for whitening leads to robustness of subspace decompositions to noise and, thereby, enhances the unitary mixture representations of the problem. It also

applies equal source discrimination and allows the consideration of the same subset of sources in both the whitening and joint-diagonalization phases.

II. Signal Model

In narrowband array processing, when n signals arrive at an m -element array, the linear data model

$$\mathbf{x}(t) = \mathbf{y}(t) + \mathbf{n}(t) = \mathbf{A}\mathbf{d}(t) + \mathbf{n}(t) \quad (1)$$

is commonly used, where \mathbf{A} is the mixing matrix of dimension $m \times n$ and is assumed to be full column rank, $\mathbf{x}(t) = [x_1(t), \dots, x_m(t)]^T$ is the sensor array output vector, and $\mathbf{d}(t) = [d_1(t), \dots, d_n(t)]^T$ is the source signal vector, where the superscript T denotes the transpose operator. $\mathbf{n}(t)$ is an additive noise vector whose elements are modeled as stationary, spatially and temporally white, zero-mean complex random processes, independent of the source signals.

The covariance matrix is given by

$$\mathbf{R}_{\mathbf{xx}} = E[\mathbf{x}(t)\mathbf{x}^H(t)] = \mathbf{R}_{\mathbf{yy}} + \sigma\mathbf{I} = \mathbf{A}\mathbf{R}_{\mathbf{dd}}\mathbf{A}^H + \sigma\mathbf{I}, \quad (2)$$

where $E(\cdot)$ is the statistical expectation operator, the superscript H denotes conjugate transpose, $\mathbf{R}_{\mathbf{dd}} = E[\mathbf{d}(t)\mathbf{d}^H(t)]$ is the signal covariance matrix, σ is the noise power at each sensor, and \mathbf{I} denotes the identity matrix. We assume that $\mathbf{R}_{\mathbf{xx}}$ is nonsingular, and the observation period consists of N snapshots with $N > m$.

III. Blind Source Separation based on Spatial Time-Frequency Signatures

A. Spatial Time-Frequency Distributions

The discrete form of Cohen's class of STFD of the data snapshot vector $\mathbf{x}(t)$ is given by [7]

$$\mathbf{D}_{\mathbf{xx}}(t, f) = \sum_{l=-\infty}^{\infty} \sum_{\tau=-\infty}^{\infty} \phi(l, \tau) \mathbf{x}(t+l+\tau) \mathbf{x}^H(t+l-\tau) e^{-j4\pi f\tau} \quad (3)$$

where $\phi(l, \tau)$ is a t-f kernel. Substituting (1) into (3), we obtain

$$\mathbf{D}_{\mathbf{xx}}(t, f) = \mathbf{D}_{\mathbf{yy}}(t, f) + \mathbf{D}_{\mathbf{yn}}(t, f) + \mathbf{D}_{\mathbf{ny}}(t, f) + \mathbf{D}_{\mathbf{nn}}(t, f). \quad (4)$$

Under the uncorrelated signal and noise assumption and the zero-mean noise property, $E[\mathbf{D}_{\mathbf{yn}}(t, f)] = E[\mathbf{D}_{\mathbf{ny}}(t, f)] = \mathbf{0}$. It follows

$$E[\mathbf{D}_{\mathbf{xx}}(t, f)] = \mathbf{D}_{\mathbf{yy}}(t, f) + E[\mathbf{D}_{\mathbf{nn}}(t, f)] = \mathbf{A}\mathbf{D}_{\mathbf{dd}}(t, f)\mathbf{A}^H + E[\mathbf{D}_{\mathbf{nn}}(t, f)]. \quad (5)$$

Similar to (2), which relates the signal covariance matrix to the data spatial covariance matrix, (5) provides the basis for source separation by relating the STFD matrix to the source TFD matrix, $\mathbf{D}_{\mathbf{dd}}(t, f)$.

B. Blind Source Separation [7]

In blind source separation techniques, there is an ambiguity with respect to the order and the complex amplitude of the sources. It is convenient to assume that each source has unit norm, that is, $\mathbf{R}_{\mathbf{dd}} = \mathbf{I}$.

The first step of blind source separation based on TFDs is whitening of the signal $\mathbf{x}(t)$ of the observation. This is achieved by estimating the noise power¹ and applying a whitening matrix \mathbf{W} to $\mathbf{x}(t)$, i.e., an $n \times m$ matrix satisfying:

$$\mathbf{W}\mathbf{R}_{\mathbf{yy}}\mathbf{W}^H = \mathbf{W}(\mathbf{R}_{\mathbf{xx}} - \sigma\mathbf{I})\mathbf{W}^H = \mathbf{W}\mathbf{A}\mathbf{A}^H\mathbf{W}^H = \mathbf{I}. \quad (6)$$

The whitening matrix is estimated from the eigendecomposition of $\mathbf{R}_{\mathbf{xx}}$ [7]. The accuracy of the whitening matrix estimate depends on the estimation accuracy of the eigenvectors and eigenvalues corresponding to the signal subspace. The whitened process $\mathbf{z}(t) = \mathbf{W}\mathbf{x}(t)$ still obeys a linear model,

$$\mathbf{z}(t) = \mathbf{W}\mathbf{x}(t) = \mathbf{W}\mathbf{A}\mathbf{d}(t) + \mathbf{W}\mathbf{n}(t) = \mathbf{U}\mathbf{d}(t) + \mathbf{W}\mathbf{n}(t), \quad (7)$$

¹The noise power can be estimated only when $m > n$ [7]. If $m = n$, the estimation of the noise power becomes unavailable and $\sigma = 0$ will be assumed.

where $\mathbf{U} \triangleq \mathbf{W}\mathbf{A}$ is an $n \times n$ unitary matrix.

The next step is to estimate the unitary matrix \mathbf{U} . The whitened STFD matrices in the noise-free case can be written as

$$\mathbf{D}_{\mathbf{z}\mathbf{z}}(t, f) = \mathbf{W}\mathbf{D}_{\mathbf{x}\mathbf{x}}(t, f)\mathbf{W}^H = \mathbf{U}\mathbf{D}_{\mathbf{d}\mathbf{d}}(t, f)\mathbf{U}^H. \quad (8)$$

In the autoterm regions², $\mathbf{D}_{\mathbf{d}\mathbf{d}}(t, f)$ is diagonal, and an estimate $\hat{\mathbf{U}}$ of the unitary matrix \mathbf{U} may be obtained as a joint diagonalizer of the set of whitened STFD matrices evaluated at K autoterm t-f points, $\{\mathbf{D}_{\mathbf{z}\mathbf{z}}(t_i, f_i) | i = 1, \dots, K\}$. The source signals and the mixing matrix can be, respectively, estimated as $\hat{\mathbf{d}}(t) = \hat{\mathbf{U}}\hat{\mathbf{W}}\mathbf{x}(t)$ and $\hat{\mathbf{A}} = \hat{\mathbf{W}}^\# \hat{\mathbf{U}}$, where superscript $\#$ denotes pseudo-inverse.

IV. Properties of STFD Matrices

In reference [13], the subspace analyses of STFD matrices are presented for signals with clear t-f signatures, such as frequency modulated (FM) signals. It was shown that the offerings of using a STFD matrix instead of the covariance matrix are two-fold. First, the selection of autoterm t-f points, e.g., points on the source instantaneous frequency where the power is concentrated, enhances the SNR. Second, the difference in the t-f localization properties of the source signals permits source discrimination and allows the selection of fewer sources for matrix construction. In the presence of noise, the consideration of a subset of signal arrivals reduces perturbation in matrix eigendecomposition, and becomes essential when there is insufficient number of sensors.

The prime motivation of this letter is to make use of the above properties in the whitening phase of TFD-based BSS methods. In particular, the implicit reduction in the noise as a result of autoterm selection and fewer source considerations lead to improved signal subspace and source number estimation. Both, according to (11), are key to the whitening matrix construction.

²The selection of autoterm regions has been discussed in [11], [12], [14].

V. Modified Method for Source Separation

In the method proposed in [7] and summarized in Section III, although STFD matrices are used to estimate the unitary matrix \mathbf{U} , the covariance matrix is still used in the whitening process. Using the STFD matrix in place of the covariance matrix $\mathbf{R}_{\mathbf{xx}}$ to perform whitening is an attractive alternative.

Denote $\mathbf{D}_{\mathbf{xx}}(t_1, f_1), \dots, \mathbf{D}_{\mathbf{xx}}(t_K, f_K)$ as the STFD matrices constructed from K autoterm points being defined over a t-f region Ω and belonging to fewer $n_o \leq n$ signals. Also, denote, respectively, $\mathbf{d}^o(t)$ and $\dot{\mathbf{d}}(t)$ as the n_o and $n - n_o$ sources being present and absent in the t-f region Ω . The $n - n_o$ sources could be undesired emitters or sources to be separated in the next round of processing. The value of n_o is generally unknown and can be determined from the eigenstructure of the STFD matrix. Using the above notations, we have

$$\mathbf{x}(t) = \mathbf{A}^o \mathbf{d}^o(t) + \dot{\mathbf{A}} \dot{\mathbf{d}}(t) + \mathbf{n}(t), \quad (9)$$

where \mathbf{A}^o and $\dot{\mathbf{A}}$ are the $m \times n_o$ and $m \times (n - n_o)$ mixing matrices corresponding to $\mathbf{d}^o(t)$ and $\dot{\mathbf{d}}(t)$, respectively.

Let $\tilde{\mathbf{D}}_{\mathbf{xx}}$ be the average STFD matrix of a set of STFD matrices defined over the same region Ω , but may incorporate a different t-f kernel. The incorporation of multiple (t, f) points through the averaging process reduces the noise effect on the signal subspace estimation, as discussed in [13]. Denote $\hat{\sigma}^{tf}$ as the estimation of the noise-level eigenvalue of the STFD matrix $\tilde{\mathbf{D}}_{\mathbf{xx}}$. Then,

$$\tilde{\mathbf{W}} \tilde{\mathbf{D}}_{\mathbf{yy}} \tilde{\mathbf{W}}^H = \tilde{\mathbf{W}} (\tilde{\mathbf{D}}_{\mathbf{xx}} - \hat{\sigma}^{tf} \mathbf{I}) \tilde{\mathbf{W}}^H = \tilde{\mathbf{W}} \mathbf{A}^o \tilde{\mathbf{D}}_{\mathbf{dd}}^o (\tilde{\mathbf{W}} \mathbf{A}^o)^H = \mathbf{I}. \quad (10)$$

In (10), due to the ambiguity of signal complex amplitude in BSS, we have assumed that the averaged source TFD matrix $\tilde{\mathbf{D}}_{\mathbf{dd}}^o$ corresponding to $\mathbf{d}^o(t)$ is \mathbf{I} of $n_o \times n_o$ for convenience and without loss generality. Therefore, the whitening matrix $\tilde{\mathbf{W}}$ is obtained as

$$\tilde{\mathbf{W}} = [(\lambda_1^{tf} - \hat{\sigma}^{tf})^{-1/2} \mathbf{h}_1^{tf}, \dots, (\lambda_{n_o}^{tf} - \hat{\sigma}^{tf})^{-1/2} \mathbf{h}_{n_o}^{tf}]^H, \quad (11)$$

where $\lambda_1^{tf}, \dots, \lambda_{n_o}^{tf}$ are the n_o largest eigenvalues of $\tilde{\mathbf{D}}_{\mathbf{xx}}$ and $\mathbf{h}_1^{tf}, \dots, \mathbf{h}_{n_o}^{tf}$ are the corresponding eigenvectors of $\tilde{\mathbf{D}}_{\mathbf{xx}}$. Note that $\tilde{\mathbf{D}}_{\mathbf{dd}}^o$ and $\tilde{\mathbf{D}}_{\mathbf{yy}}$ are of reduced rank n_o instead of rank n , due to the source discrimination performed through the selection of the t-f points or specific t-f region. Therefore, $\tilde{\mathbf{W}}\mathbf{A}^o = \tilde{\mathbf{U}}$ is a unitary matrix, whose dimension is $n_o \times n_o$ rather than $n \times n$. The whitened process $\tilde{\mathbf{z}}(t)$ becomes

$$\tilde{\mathbf{z}}(t) = \tilde{\mathbf{W}}\mathbf{x}(t) = \tilde{\mathbf{W}}\mathbf{A}^o\mathbf{d}^o(t) + \tilde{\mathbf{W}}\mathbf{A}\dot{\mathbf{d}}(t) + \tilde{\mathbf{W}}\mathbf{n}(t) = \tilde{\mathbf{U}}\mathbf{d}^o(t) + \tilde{\mathbf{W}}\mathbf{A}\dot{\mathbf{d}}(t) + \tilde{\mathbf{W}}\mathbf{n}(t), \quad (12)$$

In the t-f region Ω , the TFD of $\dot{\mathbf{d}}(t)$ is zero and, therefore, the averaged STFD matrix of the noise-free components becomes an identity matrix, i.e.,

$$\tilde{\mathbf{D}}_{\mathbf{zz}} = \tilde{\mathbf{W}}\tilde{\mathbf{D}}_{\mathbf{xx}}\tilde{\mathbf{W}}^H = \tilde{\mathbf{U}}\tilde{\mathbf{D}}_{\mathbf{dd}}^o\tilde{\mathbf{U}}^H = \mathbf{I}. \quad (13)$$

Eqn. (13) implies that the autoterm and crossterm TFDs averaged over the t-f region Ω become unity and zero, respectively, upon whitening with matrix $\tilde{\mathbf{W}}$. $\tilde{\mathbf{U}}$ as well as the mixing matrix and source waveforms are estimated following the same procedure of Section III. It is noted that, when $n_o = 1$, source separation is no longer necessary.

Selection of the same number of sources, n_o , should be done at both whitening and joint diagonalization stages, otherwise mismatching of the corresponding sources will result. While our proposed modified blind source separation method provides the mechanism to satisfy this condition, the covariance-based whitening approach does not lend itself to avoid the mismatching.

VI. Simulation Results

We consider a two-sensor array with a half-wavelength spacing. For simplicity, we consider chirp signals as the sources to be separated. In the first example, two chirp signals are received in the presence of white Gaussian noise. The sources arrive from different directions $\theta_1 = 30^\circ$ and $\theta_2 = 35^\circ$. The normalized start and end frequencies of the first chirp signal are 0 and 0.5, respectively, whereas those for the second signal are

0.1 and 0.4. The number of snapshots used is 1024.

The performance is evaluated by using the mean rejection level (MRL), defined as [7]

$$\text{MRL} = \sum_{p \neq q} E \left| (\hat{\mathbf{A}}^\# \mathbf{A})_{pq} \right|^2 \quad (14)$$

where $\hat{\mathbf{A}}$ is the estimate of \mathbf{A} . A smaller value of the MRL implies better source separation results. An MRL lower than -10 dB is considered satisfactory [7].

Fig. 1 shows the MRL versus the input SNR of the two sources (we assume that all signals have the same power). The dashed line corresponds to the existing method where the covariance matrix \mathbf{R}_{xx} is used for whitening, and the solid line corresponds to the modified method where the averaged STFD matrix $\tilde{\mathbf{D}}_{xx}$ is used instead. In the latter, the average of spatial pseudo-Wigner-Ville distributions (SPWVDs) of window size 257 is applied to estimate the whitening matrix. For the estimation of the unitary matrix for both methods, the spatial Wigner-Ville distribution (SWVD)³ matrices using the entire data record are computed. The number of points used to perform the joint diagonalization is $K = 32$ for each signal and the points are selected on the signal instantaneous frequencies. The curves are calculated by averaging 100 independent trials with different noise sequences. Fig. 1 clearly shows the improvement when STFDs are used in both phases of source separations, specifically for low SNRs. To satisfy the -10 dB MRL, the required input SNR is about 17.8 dB for the existing method and is about 5.6 dB for the modified method.

To examine the advantages of source discrimination in the t-f domain, we add another chirp signal to the above scenario. The third chirp arrives from direction $\theta_3 = 40^\circ$, and its normalized start and end frequencies are 0.15 and 0.55, respectively. Other parameter settings are the same as those used in Fig. 1. Only the t-f points belonging to the first two signals are chosen to construct the STFD matrices for both methods (i.e., $n_o = 2$). It is evident from Fig. 2 that, by discriminating against, or filtering out, the third signal,

³The method proposed here is not limited to use specific TFDs and the SPWVD and SWVD are chosen for simplicity. Other TFDs can also be used.

the modified method provides very close performance to the two-signal case, whereas the existing covariance matrix based whitening method, due to the inability to discriminate among sources and provide sufficient degrees-of-freedom for subspace estimation, cannot provide satisfactory MRL, even when the input SNR is high.

VII. Conclusion

A modified blind source separation method for nonstationary signals is introduced. In this method, the TFD signal localization properties are fully utilized for improved separation performance. The proposed modification provides noise robustness and can be used to reduce the number of sources considered for separation.

References

- [1] L. Tong, Y. Inouye, and R-W. Liu, "Waveform-preserving blind estimation of multiple independent sources," *IEEE Trans. Signal Proc.*, vol. 41, no. 7, pp. 2461–2470, July 1993.
- [2] J. F. Cardoso and A. Souloumiac, "Blind beamforming for non-Gaussian signals," *IEE Proc. F*, vol. 140, no. 6, pp. 362–370, Dec. 1993.
- [3] A. Belouchrani, K. A. Meraim, H.-F. Cardoso, and E. Moulines, "A blind source separation techniques using second order statistics," *IEEE Trans. Signal Proc.*, vol. 45, no. 2, pp. 434–444, Feb. 1997.
- [4] O. Grellier and P. Comon, "Blind separation of discrete sources," *IEEE Signal Processing Letters*, vol. 5, no. 8, pp. 212–214, Aug. 1998.
- [5] B. Boashash (ed.), *Time-Frequency Signal Analysis and Processing*, Englewood, NJ: Prentice-Hall, 2002.
- [6] V. Chen and H. Ling, *Time-Frequency Transforms for Radar Imaging and Signal Analysis*, Boston, MA: Artech House, 2002.
- [7] A. Belouchrani and M. G. Amin, "Blind source separation based on time-frequency signal representation," *IEEE Trans. Signal Proc.*, vol. 46, no. 11, pp. 2888–2898, Nov. 1998.
- [8] A. S. Kayhan and M. G. Amin, "Spatial evolutionary spectrum for DOA estimation and blind signal separation," *IEEE Trans. Signal Processing*, vol. 48, no. 3, pp. 791–798, March 2000.
- [9] A. R. Leyman, Z. M. Kamran, and K. Abed-Meraim, "Higher-order time frequency-based blind source separation technique," *IEEE Signal Processing Letters*, vol. 7, no. 7, pp. 193–196, July 2000.
- [10] Y. Zhang and M. G. Amin, "Spatial averaging of time-frequency distributions for signal recovery in uniform linear arrays," *IEEE Trans. Signal Processing*, vol. 48, no.

- 10, pp. 2892–2902, Oct. 2000.
- [11] A. Belouchrani, K. Abed-Meraim, M. G. Amin, and A. M. Zoubir, “Joint anti-diagonalization for blind source separation,” in *Proc. ICASSP*, Salt Lake City, UT, pp. 2789–2792, May 2001.
- [12] L. Giulieri, N. Thirion-Moreau, and P.-Y. Arques, “Blind sources separation based on bilinear time-frequency representations: a performance analysis,” in *Proc. ICASSP*, Orlando, FL, pp. 1649–1652, May 2002.
- [13] Y. Zhang, W. Mu, and M. G. Amin, “Subspace analysis of spatial time-frequency distribution matrices,” *IEEE Trans. Signal Proc.*, vol. 49, no. 4, pp. 747–759, April 2001.
- [14] W. Mu, M. G. Amin, and Y. Zhang, “Bilinear signal synthesis in array processing,” *IEEE Trans. Signal Processing*, in press.

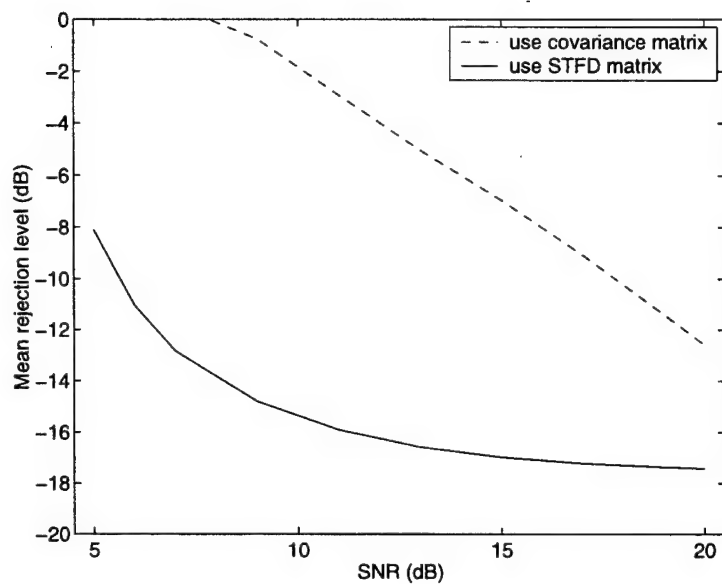


Fig. 1 MRL versus input SNR (two signal case).

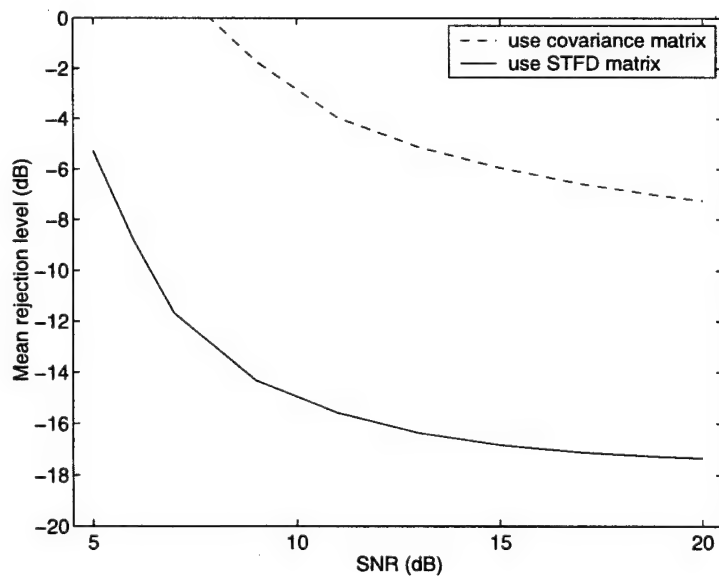


Fig. 2 MRL versus input SNR (three signal case).

A Unified Representation of Nonstationary and Cyclostationary Signals

Yimin Zhang, Moeness G. Amin, and Gordon J. Frazer

Abstract

The cyclic auto-correlation function, commonly used for cyclostationary signals, and the ambiguity function, typically employed for analysis and recovery of nonstationary signals, such as FM, have the same formulation. However, nonstationary and cyclostationary signals have distinct localization properties in the time-lag frequency-lag domain. Therefore, nonstationary and cyclostationary signals can be represented and processed within the same framework for many applications, with the distinct signatures allowing effective source discriminations. An example in array processing is given where nonstationary and cyclostationary signals are separated following simple spatial signature estimation exploiting the aforementioned properties.

I. Introduction

Most digital communication signals are stationary when they are sampled at the symbol-rate. On the other hand, when they are fractionally sampled, they demonstrate the so-called cyclostationary property, that is, the self-correlation function of such a signal is periodic with non-zero cyclic frequencies [1]. Exploitation of the cyclostationarity allows discrimination of source signals if their cyclic frequencies are distinct. This property has been widely discussed for various purposes in array processing, for example, source separation and direction finding [2], [3], [4], [5].

Another function with similar definition is the ambiguity function [6]. An ambiguity function is usually used for nonstationary signal analysis and waveform design. The consideration of the ambiguity function for multi-sensor receivers yields ambiguity-domain direction finding and source separation methods [7].

The purpose of this paper is to consider stationary, cyclostationarity and nonstationarity in a unified framework, with applications to key problems in array processing. In the unified time-lag frequency-lag domain, cyclostationary and nonstationary signals demonstrate different properties which can be used for source selection and discrimination, leading to simplified approaches and improved performance. An example in array processing is provided where nonstationary and cyclostationary signals are separated following simple spatial signature estimation exploiting the aforementioned properties.

II. Cyclic Auto-Correlation Function and Ambiguity Function

A. Cyclic Auto-Correlation Function

The cyclic auto-correlation function $\rho_s^{\beta_i}(\tau)$ of a scalar signal $s(t)$ is defined as

$$\rho_s^{\beta_i}(\tau) = \lim_{T \rightarrow \infty} \frac{1}{T} \int_0^T e^{j\beta_i t} s(t + \tau/2) s^*(t - \tau/2) dt \quad (1)$$

where $(\cdot)^*$ denotes complex conjugate, and τ and β_i denote the time-lag and frequency-lag variables, respectively. Signals with various modulations, such as amplitude modulation (AM), phase shift keying (PSK), and frequency shift keying (FSK), demonstrate the cyclostationary property, that is, $\rho_s^{\beta_i}(\tau) \neq 0$ for non-zero values of β_i .

B. Ambiguity Function

The ambiguity function of a signal $s(t)$ is defined as

$$D_s(\theta, \tau) = \int_{-\infty}^{\infty} e^{j\theta t} s(t + \tau/2) s^*(t - \tau/2) dt \quad (2)$$

where (θ, τ) are a pair of frequency-lag and time-lag variables, respectively. Comparing (1) and (2), it is obvious that the cyclic auto-correlation function and the ambiguity function are identical except for a normalization factor.

C. A Unified Framework for Discrete-Time Signals

In this paper, we consider a unified framework for cyclostationary and nonstationary signals. By considering N observations of discrete-time data, we define the unified cyclic auto-correlation function and (normalized) ambiguity function as

$$U_s(\theta, \tau) = \frac{1}{N} \sum_{t=0}^{N-1} e^{j\theta t} s(t + \tau/2) s^*(t - \tau/2). \quad (3)$$

D. Example and Remarks

In Fig. ??, we illustrate the cyclic auto-correlation function of a BPSK signal, where 4 samples are generated from each symbol. 128 data symbols are used. A rectangular waveform is used at each symbol and the amplitude of the waveform is unity. For all plots showing the cyclic auto-correlation function (ambiguity function), the time-lag is normalized by the symbol duration T , and the frequency lag is normalized by the symbol rate $f_s = 1/T$. With sufficiently large number of data samples, the cyclic auto-correlation function has non-zero values only at $\theta = kf_s$, where k is an integer. The cyclic auto-correlation function depends on the symbol rate and the pulse shaping function.

In Fig. ??, we illustrate the ambiguity function of a chirp signal, which has the same data length as the BPSK signal (note the different τ domain compared to Fig. 1). The start frequency of the chirp is 0 and the end frequency equals the symbol rate $f_s = 1/T$ (the corresponding range of θ is from 0 to $\pi/2$). The amplitude of the FM signal is 1. The ambiguity function of a chirp signal shows a linear signature, for which the line of the peak values always passes through the origin ($\theta = \tau = 0$).

It is clear that the peak values of the cyclic auto-correlation of a BPSK signal and the ambiguity function of a chirp signal overlap over only a very limited area. Unlike

the cyclic auto-correlation function of the BPSK signal, which has fixed and multiple cyclic frequencies, the frequency-lag for the ambiguity function of a chirp signal is time-lag dependent. Moreover, high values of the ambiguity function appear for each time-lag, in contrast to the cyclic auto-correlation function of a BPSK signal where the peaks correspond to only specific time-lag values. These properties are very important in source discrimination, as will be discussed later.

It is noted that the distinctive signature contrast between the digital signal and the FM signal is not preserved in the time-frequency domain, where the autoterm of the digital signal spreads over the entire time and frequency extent of the signal.

III. Array Processing

A. Signal Model

When m source signals impinge on an array of n sensors (we assume that $n \geq m$), the received signal vector $\mathbf{x}(t) = [x_1(t), \dots, x_n(t)]^T$ is expressed in the following form ($(\cdot)^T$ denotes the transpose of a matrix or a vector)

$$\mathbf{x}(t) = \mathbf{y}(t) + \mathbf{w}(t) = \mathbf{A}\mathbf{s}(t) + \mathbf{w}(t) \quad (4)$$

where $\mathbf{y}(t) = [y_1(t), \dots, y_n(t)]^T$ is the noise-free signal vector, $\mathbf{w}(t) = [w_1(t), \dots, w_n(t)]^T$ is the noise vector, and $\mathbf{s}(t) = [s_1(t), \dots, s_m(t)]^T$ is the source signal vector. Moreover, $\mathbf{A} = [\mathbf{a}_1, \dots, \mathbf{a}_m]$ is the $n \times m$ mixing matrix which is unknown. It is assumed that the noise vector $\mathbf{w}(t)$ is stationary and is uncorrelated with the source signal vector $\mathbf{s}(t)$ (the noise vector may be spatially and temporally white or colored).

For multi-antenna receivers, the (k, l) -th element of the cyclic correlation matrix (spatial ambiguity matrix) $\mathbf{U}_x(\theta, \tau)$ can be defined as the cyclic cross-correlation function (cross-ambiguity function) between x_k and x_l , expressed as

$$[\mathbf{U}_x(\theta, \tau)]_{k,l} = \frac{1}{N} \sum_t e^{j\theta t} x_k(t + \frac{\tau}{2}) x_l^*(t - \frac{\tau}{2}) \quad (5)$$

Denote $\mathbf{U}_s(\theta, \tau)$ as the cyclic correlation matrix (ambiguity matrix) of the source vector \mathbf{s} . The (k, l) -th element of $\mathbf{U}_s(\theta, \tau)$ is the cyclic cross-correlation function (cross-ambiguity function) between $s_k(t)$ and $s_l(t)$. We obtain the following result from (5)

$$E[\mathbf{U}_x(\theta, \tau)] = \mathbf{A}\mathbf{U}_s(\theta, \tau)\mathbf{A}^H \quad (6)$$

for $\theta \neq 0$, where $(\cdot)^H$ denote conjugate transpose. Note that the noise component is not shown in (6) as the expectation value of the cyclic auto- and cross-correlation function (ambiguity function) of the stationary noise is zero for $\theta \neq 0$.

B. Source Discrimination and Separation

It is noted that (6) is valid for any point (θ, τ) , $\theta \neq 0$. When considering one BPSK and one FM signal, (θ, τ) regions can be identified which include (θ, τ) points belonging to only one signal. That is, in the first group Ω_1 where the (θ, τ) points pertain to the BPSK signal, we have

$$E[\mathbf{U}_x(\theta, \tau)] = \mathbf{a}_1 U_{s_1}(\theta, \tau) \mathbf{a}_1^H. \quad (7)$$

Similary, in the second group Ω_2 where the (θ, τ) points pertain to the FM signal, we have

$$E[\mathbf{U}_x(\theta, \tau)] = \mathbf{a}_2 U_{s_2}(\theta, \tau) \mathbf{a}_2^H. \quad (8)$$

Therefore, in either Ω_1 or Ω_2 , $E[\mathbf{U}_x(\theta, \tau)]$ is rank one, and the spatial signature \mathbf{a}_i can be easily estimated from $E[\mathbf{U}_x(\theta, \tau)]$ evaluated at any $(\theta, \tau) \in \Omega_k$, $k = 1, 2$. Given finite period of data observation, multiple (θ, τ) points can be incorporated to achieve an improved estimate of the spatial signature. A convenient way to incorporate multiple (θ, τ) points is data augmentation [3], which obtains the spatial signature as the eigenvector corresponding to the maximum eigenvalue of $\mathbf{V}_k \mathbf{V}_k^H$, where \mathbf{V}_k is an augmented spatial cyclic correlation matrix (spatial ambiguity matrix)

$$\mathbf{V}_k = [\mathbf{U}_x(\theta_0, \tau_0), \mathbf{U}_x(\theta_1, \tau_1), \dots, \mathbf{U}_x(\theta_{L-1}, \tau_{L-1})], \quad (9)$$

where $\mathbf{U}_x(\theta_i, \tau_i) \in \Omega_k$ for $i = 0, 1, \dots, L-1$ and $k = 1, 2$. The high computations of eigendecomposition can be avoided by using a simpler, but less noise robust approach in which one, say, the first, column of matrix $\mathbf{V}_k \mathbf{V}_k^H$ is used instead.

Once the spatial signatures of both signals are estimated as $\hat{\mathbf{A}} = [\hat{\mathbf{a}}_1, \hat{\mathbf{a}}_2]$, the waveform of the BPSK signal can be estimated from

$$\hat{\mathbf{s}} = \hat{\mathbf{A}}^\# \mathbf{x} \quad (10)$$

where $(\cdot)^\#$ denotes pseudo-inverse of a matrix.

It is noted that, when one of the two signals is far stronger than the other, the spatial signature of the weak signal should be estimated after the strong signal is removed by projecting the data to its orthogonal subspace [8]. An example of recovery of a BPSK signal in the presence of strong FM jammer is presented in [9].

IV. Simulation Results

In the simulations, we consider one BPSK signal and one chirp signal impinging on a three-sensor linear array with half-wavelength spacing. The respective waveforms are described in Section II. The input power of both signals is 10 dB, and the input noise power is 0 dB. The following mixing matrix is used:

$$\mathbf{A} = \begin{bmatrix} 0.890 + j0.465 & 0.962 + j0.012 \\ 0.065 - j0.826 & 0.779 + j0.481 \\ -0.761 + j0.852 & -1.100 - j0.160 \end{bmatrix}$$

which corresponds to the magnitude value 0.62 of the spatial correlation coefficient between the BPSK and the chirp signal.

Fig. ?? shows the true and estimated waveforms of both signals. 512 $(\theta, \tau) \neq 0$ points along the chirp signature are used in estimating the spatial signature of the chirp signal, whereas 4 (θ, τ) points at $(\pm 1/T, \pm T/2)$ are used for the BPSK signal. The mean square error (MSE) obtained from 200 independent trials is -15.65 dB and -12.51 dB respectively for the two signals, which is very close to the bound -15.67 dB and -12.66 dB computed using the true mixing matrix \mathbf{A} instead of $\hat{\mathbf{A}}$ in (10). The BPSK signal has a lower MSE of about 3 dB because the quadrature noise component is removed.

V. Conclusions

A generalized framework is presented for separation and waveform recovery of cyclostationary and nonstationary signals. This approach is based on the general definition of the cyclic auto-correlation function and the ambiguity function. Based on the distinct localization properties of the nonstationary signals and cyclostationary signals in the time-lag frequency-lag domain, source discrimination can be performed prior to array processing, leading to simple yet effective waveform recovery.

References

- [1] W. A. Gardner, "Exploitation of the spectral redundancy in cyclostationary signals," *IEEE Signal Processing Mag.*, vol. 8, pp. 14–37, 1991.
- [2] W. A. Gardner, "Simplification of MUSIC and ESPRIT by exploitation of cyclostationarity," *Proc. IEEE*, vol. 76, no. 7, pp. 1775–1786, 1991.
- [3] G. Xu and T. Kailath, "Direction-of-arrival estimation via exploitation of cyclostationarity — A combination of temporal and spatial processing," *IEEE Trans. Signal Processing*, vol. 40, no. 7, pp. 1775–1786, 1992.
- [4] B. G. Agee, S. V. Schell, and W. A. Gardner, "Spectral self-coherence restoral: a new approach to blind adaptive signal extraction using antenna arrays," *Proc. IEEE*, vol. 78, no. 4, pp. 753–767, April 1990.
- [5] K. Abed-Merain, X. Xiang, J. H. Manton, and Y. Hua, "Blind source separation using second-order cyclostationary statistics," *IEEE Trans. Signal Processing*, vol. 49, no. 4, pp. 694–701, April 2001.
- [6] L. Cohen, *Time-Frequency Analysis*. Englewood Cliffs, NJ: Prentice Hall, 1995.
- [7] M. G. Amin, A. Belouchrani, and Y. Zhang, "The spatial ambiguity function and its applications," *IEEE Signal Processing Letters*, vol. 7, no. 6, pp. 138–140, June 2000.
- [8] M. G. Amin and Y. Zhang, "Interference suppression in spread-spectrum communication systems," in J. G. Proakis ed., *The Wiley Encyclopedia of Telecommunications*, New York, NY: John Wiley, 2002.
- [9] Y. Zhang, M. G. Amin, and G. J. Frazer, "A new approach to FM jammer suppression for digital communications," in *Proc. IEEE Sensor Array and Multichannel Signal Processing Workshop*, Rosslyn, VA, Aug. 2002.

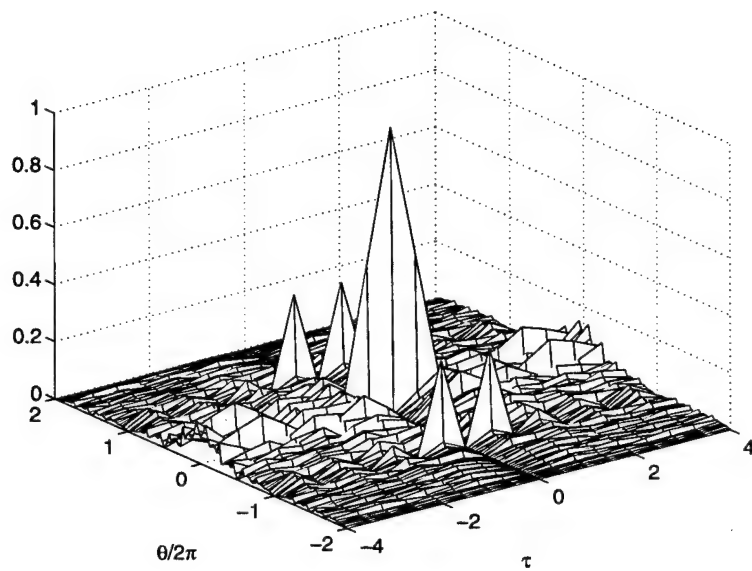


Fig. 1. Cyclic auto-correlation function (magnitude) of a fractionally sampled BPSK signal.

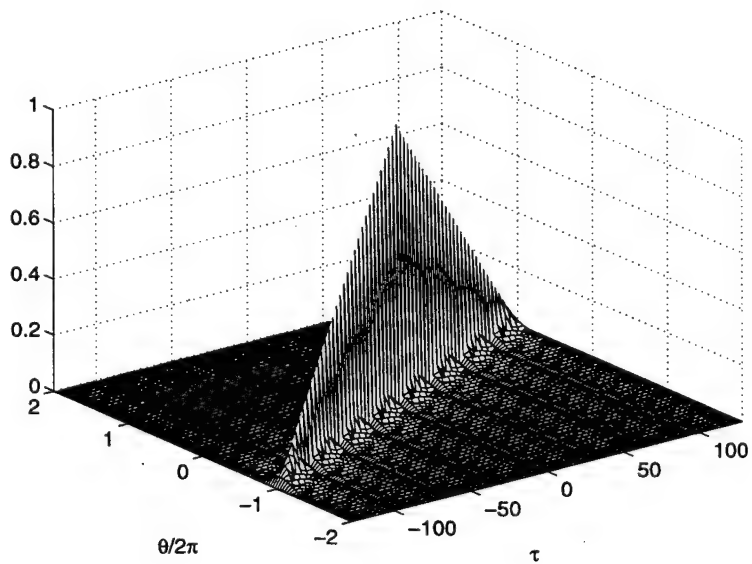


Fig. 2. Time-averaged ambiguity function (magnitude) of a chirp signal.

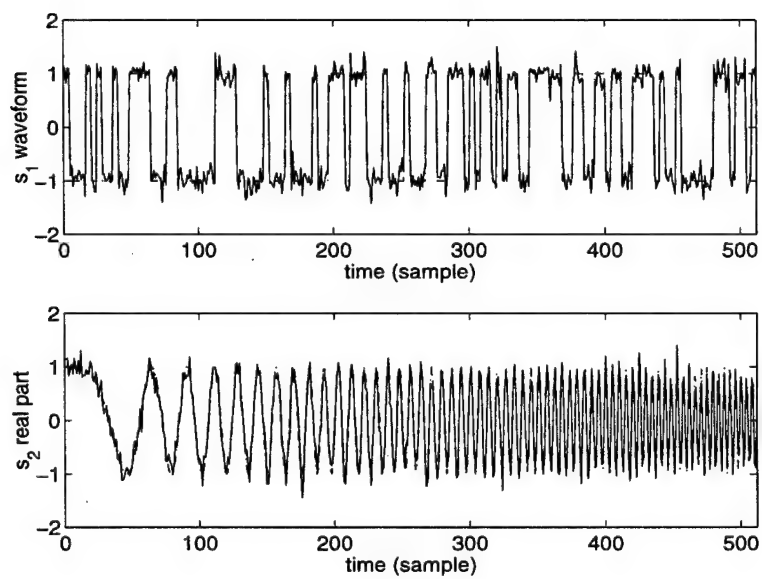


Fig. 3. True (---) and estimated (—) waveforms of both signals.

Aperture Synthesis for a Through-the-wall Imaging System

Fauzia Ahmad, Saleem A. Kassam, Gordon J. Frazer, and Moeness G. Amin

Abstract

An aperture synthesis scheme using subarrays that is based on the coarray concept is proposed for through-the-wall microwave imaging applications. Simulation results depicting the effectiveness of the proposed synthetic aperture technique for a TWI system are presented. The effects of incorrect estimates of wall parameters and errors in array element placement on this technique are also investigated.

1. Introduction

The ability to see through walls, doors and other visually opaque materials, using microwave signals has become a major area of interest in a variety of military and commercial applications. Through-the-wall imaging (TWI) can be used in rescue missions, behind-the-wall target detection, surveillance and reconnaissance, and even sensing through smoke and dust. Ferris and Currie [1,2] have reviewed existing and under development microwave systems that can detect the presence of persons behind walls and track their movement. Depending on the technology involved, these systems can provide a range resolution of a few inches and are able to sense moving targets and measure their speed. However, most of these systems have poor spatial resolution.

Improved spatial resolution can be achieved by using an enlarged array aperture. However, with the constraints of portability and low cost on the system, an innovative scheme is required for increasing the effective system aperture. In this paper, we use an aperture synthesis scheme based on the coarray formalism for TWI. The concept of coarrays was originally defined for narrow-band far-field active imaging [3, 4], and has also been extended to wideband imaging [5]. The coarray provides a convenient and elegant framework for understanding linear imaging techniques. This concept is important for active imaging, as the angular resolution and the point spread function, which is the response of the system to a point target, are directly related to the size of the coarray of the imaging system.

The coarray completely characterizes the performance of an imaging system, and is defined to be the set [3]

$$C_S = \{\underline{z} : \underline{z} = \underline{x} + \underline{y}, \underline{x} \in S_T, \underline{y} \in S_R\} \quad (1)$$

where S_T and S_R are the sets containing the position vectors of the elements in the transmit and receive apertures, respectively. It is possible for two systems that have the same coarray to achieve the same imaging performance.

2. System Specifications

In the underlying TWI system, we consider a pulsed radar system with a bandwidth of 666 MHz centered at 2 GHz. The system has a range resolution of 0.225 m.

2.1 Choice of pulse repetition frequency (PRF)

The maximum unambiguous range sets the upper limit on the PRF, whereas the lower limit is set by the desire to avoid Doppler ambiguities. For a pulsed radar, these limits on PRF f_r are given by

$$2f_{d\max} \leq f_r \leq c/2R_u \quad (2)$$

where R_u and $f_{d\max}$ are the maximum unambiguous range and maximum anticipated target Doppler frequency respectively. The free space path loss for the round trip range of 100m at 2 GHz is 78.4 dB [6]. In addition to this, there will be losses due to attenuation as a result of transmission through the wall, and further losses due to the fact that only part of the transmitted signal gets reflected at each juncture. Therefore, signals returning from beyond this round trip range of 100m would be highly attenuated. We set the unambiguous range for our TWI radar system to be 50 m (one half of the round trip range), which corresponds to a PRF of 3 MHz. On the other hand, considering the effect of likely translation, rotation, and oscillation of moving objects [7], we opt for a

maximum anticipated Doppler frequency of 250 Hz. This sets the lower limit of 500 Hz on the PRF. Accordingly, $500 \text{ Hz} \leq f_r \leq 3 \text{ MHz}$.

2.2 Effects of the wall through which the system is looking

The composition and thickness of the wall, its dielectric constant, and the angle of incidence all affect the strength and characteristics of the signal propagating through the wall. The dielectric constant of a dry concrete wall lies between 8 and 12. The velocity of a radio wave through a medium of dielectric constant ϵ is given by

$$v = \frac{c}{\sqrt{\epsilon}} \quad (3)$$

where c is the speed of light. Therefore, the velocity of a signal propagating through a concrete wall will decrease by a factor of 2.8 to 3.4, inducing a bias in the target range measurements [8].

3. Aperture Synthesis Using Subarrays

In this scheme, we employ a smaller transmit/receive array system as a subarray to synthesize an effective larger aperture. The transmit and receive subarray pairs are used to form component complex images by weighted linear beamforming, which will then be added coherently to obtain the composite complex amplitude image with the desired spatial resolution. The composite image has an effective coarray that is the union of the individual coarrays corresponding to each transmit/receive subarray pair. This and several other aperture synthesis techniques based on the coarray have been discussed in detail in [3].

Since aperture synthesis is obtained by independent serial use of the various subarrays, the overall system transmit and receive processing apparatus simplifies to that required by one subarray combined with a subarray multiplexer. The resolution of the larger array can thus be obtained by the use of a smaller number of processing channels at the expense of increased data acquisition time.

3.1 Transmit and Receive Apertures

Achieving a spatial resolution of one-half a meter at a range of 5 meters along both cross-range directions requires the length of the coarray along both directions to be at least 10λ , where $\lambda=0.15\text{m}$ is the wavelength corresponding to 2 GHz. This resolution could be obtained by use of a $\lambda/2$ -spaced 11×11 element square filled array for both transmission and reception. However, such an array would require a total of 121 transmit/receive elements, thereby rendering it impractical. Alternatively, we can design transmit and receive array geometries of Fig. 1(a,b). The transmit array is a 4-element sparse array with an inter-element spacing of 8λ . The receive array is a $\lambda/2$ -spaced 8×8 element square array. The corresponding coarray is shown in Fig. 1(c). It has a length of 11.5λ along both cross-range directions, thereby giving a resolution of 0.43m at 5m range. In order to apply the aperture synthesis technique, we divide these arrays into several transmit/receive subarray pairs. The total number of such pairs is determined by the increased data acquisition time due to serial operation of all the subarray apertures and the PRF of the system. In the extreme case of a single transmitter and a single receiver subarray, there will be a total of 256 subarray pairs. This requires 256 pulses to generate one composite complex amplitude image. If the system is operating at a PRF of 3 MHz, the "actual" PRF for the system using subarrays will be $3\text{ MHz}/256$ or 11.72

kHz, which is still 23 times higher than the lower limit of 500 Hz on the PRF. Assuming the scene is stationary over the $0.80\mu\text{s}$ pulse repetition interval, we opt for single transmitter, single receiver subarray apertures for the proposed system.

The subarray scheme in aperture synthesis partitions the coarray into distinct regions, which, for our system, are single-element disjoint subsets of the whole coarray. The coarray subsets corresponding to the 64 subarray pairs involving the same transmitter are represented by the same shade of gray as that of the transmitter in Fig. 1(c).

3.2 Imaging System Model

We consider the wall and the transmit/receive subarray of omni-directional transducers to be located in the x-y plane, whereas the volume to be imaged is located along the positive z-axis. The volume of interest is divided into a finite number of pixels in range, azimuth, and elevation. In order to image the set of ranges located along a particular elevation and azimuth (θ_f, φ_f) , we apply a time delay to the transmit element to focus it at range R_f along (θ_f, φ_f) . Then, we transmit the pulse, and process the reflections as follows. Time delay is applied to the receive element so that it is focused at $(R_f, \theta_f, \varphi_f)$. The delayed output from the receiver is matched filtered to detect I and Q components of the resulting signal, and a single complex value $I+jQ$ is formed. This process is repeated for each range R_f in direction (θ_f, φ_f) and then repeated again for each elevation and azimuth in the volume of interest. Component images are formed by repeating this process with various subarrays, and are coherently added to form the composite image. The displayed image is the magnitude of the complex value measured for each pixel.

Let us now consider in detail what the value of a single image pixel will be with a single transmitter, single receiver subarray for the case of a single point target. The

general case of multiple targets can be obtained by superposition. Let the transmitter and receiver locations be \mathbf{x}_t and \mathbf{x}_r . Let the target be located in the direction $\mathbf{g}=(u,v)=(\sin(\theta)\cos(\phi), \sin(\theta)\sin(\phi))$ at range R as shown in Fig. 2. Suppose it is desired to image the pixel at range R_f in the direction $\mathbf{h}=(\sin(\theta_f)\cos(\phi_f), \sin(\theta_f)\sin(\phi_f))$. As a time reference, let an element at the origin be given zero time delay. Let $p(t)=\text{Re}\{y(t)\exp(j\omega_c t)\}$ be the pulse transmitted from an element at the origin. $y(t)$ is the complex amplitude of the pulse at ω_c . Then the pulse received at \mathbf{x}_r when the transmitter is at \mathbf{x}_t is

$$q(t)=\text{Re}\{\exp(-\alpha(d_t+d_r))a(R,\mathbf{g})w_t w_r y(t-\tau)\exp(j\omega_c(t-\tau))\} \quad (4)$$

where α is the attenuation constant of the wall, d_t and d_r are the distances traveled through the wall on transmit and receive respectively, $a(R,\mathbf{g})$ is the complex reflectivity of the target, w_t and w_r are the weights applied to the transmit and receive elements respectively and τ is the sum of propagation and focusing delays when the array is focused in direction \mathbf{h} . These delays incorporate the slowing of waves due to propagation through the wall. The received signal is passed through I and Q matched filters, and their outputs are sampled at time T corresponding to the waveform time of flight for the focused range R_f . Hence,

$$I = \int q(\xi)y(\xi-T)\cos(\omega_c(\xi-T))d\xi \quad (5)$$

$$Q = -\int q(\xi)y(\xi-T)\sin(\omega_c(\xi-T))d\xi \quad (6)$$

where

$$T = (2R_f - (d_t + d_r))/c + (d_t + d_r)/v \quad (7)$$

and v is given by (3).

3.3 Model of the Walls

Each of the two side walls and the scene back wall is modeled as a set of point reflectors having the same constant reflectivity coefficient. Since backscattering from the two side walls is small compared to the back wall, the reflectivity coefficients as well as the density of the point targets constituting the side walls are given a lower value relative to the back wall. Figure 3 shows how these walls would look like in the R-u plane.

4. Simulation Results

In this section, we present simulated B-Scan and C-Scan images obtained using subarray aperture synthesis for the TWI system described above. All of the B-scan (Range vs. u) images are computed for $v=0$. The room being imaged is 5m x 7m. The wall through which the system is looking is a 6" thick concrete wall with a dielectric constant ϵ of 9. The room contains 4 stationary point targets, representing persons, whose locations and reflectivities are given in Table 1. Since the human body is composed of 65% water, its reflectivity is quite high as compared to that of the walls. Therefore, the back wall is given a reflectivity of 0.5 whereas each side wall is given a reflectivity of 0.3. The reflectivities are assumed to be frequency-independent. Also, the one-way attenuation through the wall is taken to be 6 dB for 6" thickness [7,8]. In all the figures, we plot the magnitude of the reflectivity estimate, with maximum value normalized to unity.

Figure 4 shows the B-scan image obtained under the assumption that the wall parameters (thickness and dielectric constant) are known exactly. We see that our scheme gives accurate estimates of target ranges and angular locations and is able to resolve the

targets at the same range. Figure 5 shows the extreme case scenario when we assume to have no knowledge of the wall parameters (estimated thickness and ϵ are 0 and 1 respectively). We note that the range estimates have large errors since the slowing down of the waves is not accounted for. Also due to focusing errors in beamforming, there is an error of 0.1 in the u -location of the target at 3m. The u -location errors of the other 3 targets are not that significant. This is because for targets closer to the front wall and at angles way off broadside, the distance through the wall is a significant portion of the target range and hence, errors are more pronounced. However, these errors would occur even if the entire transmit and receive arrays were used for beamforming instead of the subarray approach. Due to component image addition with focusing errors, the sidelobes are higher by 2 dB approximately over those in Figure 4.

Figure 6 shows the B-scan image obtained with exact knowledge of wall parameters, but with the following errors in transmit array locations (2" in left, 1" in right, 1" in top, 0" in the bottom element). These errors are possible, although large, in a practical set up. The beamformer, however, assumes no such errors exist. Although the sidelobes are raised, no other significant errors are observed. A C-scan image (u vs. v) for a fixed range of 6.0375m under no error conditions is shown in Figure 7. Clearly, the desired spatial resolution is obtained in both cross range directions.

5. Conclusions

We have examined the effectiveness of the aperture synthesis technique using subarrays for the through-the-wall microwave imaging problem. It is shown that the aperture synthesis technique can be used to achieve the desired cross-range resolution. The application of sparsely populated array geometries is desirable in TWI applications

to reduce system cost and complexity. We have shown that the proposed scheme is robust to a variety of errors such as incorrect estimates of wall parameters and array element location errors.

References

- [1] D. D. Ferris Jr. et al., "Microwave and millimeter-wave systems for wall penetration", *Proc. SPIE*, vol. 3375, pp. 269-279, Apr. 1998
- [2] D. D. Ferris Jr. et al., "A survey of current technologies for through-the-wall surveillance (TWS)", *Proc. SPIE*, vol. 3577, pp. 62-72, Nov. 1998,
- [3] R. T. Hoor et al., "The unifying role of the coarray in aperture synthesis for coherent and incoherent imaging", *Proc. IEEE*, vol. 78, no. 4, pp. 735-752, Apr. 1990.
- [4] R. J. Kozick et al., "Synthetic Aperture Pulse-Echo Imaging with Rectangular Boundary Arrays," *IEEE Trans. on Image Processing*, vol. 2, no. 1, pp. 68-79, Jan. 1993.
- [5] F. Ahmad et al., "Coarray analysis of the wide-band point spread function for active array imaging" *Signal Processing*, vol. 81, pp. 99-115, Jan 2001.
- [6] K. Pahlavan and A. H. Levesque, *Wireless Information Networks*, John Wiley & Sons Inc., 1995.
- [7] D. G. Falconer, et al., "Detection, location, and identification of building occupants using a robot-mounted through-wall radar", *Proc. SPIE*, vol. 4037, pp 72-81, 2000.
- [8] L. M. Frazier, "Radar Surveillance through Solid Materials" , *Proc. SPIE.*, vol. 2938 , pp. 139-146, Nov. 1996.

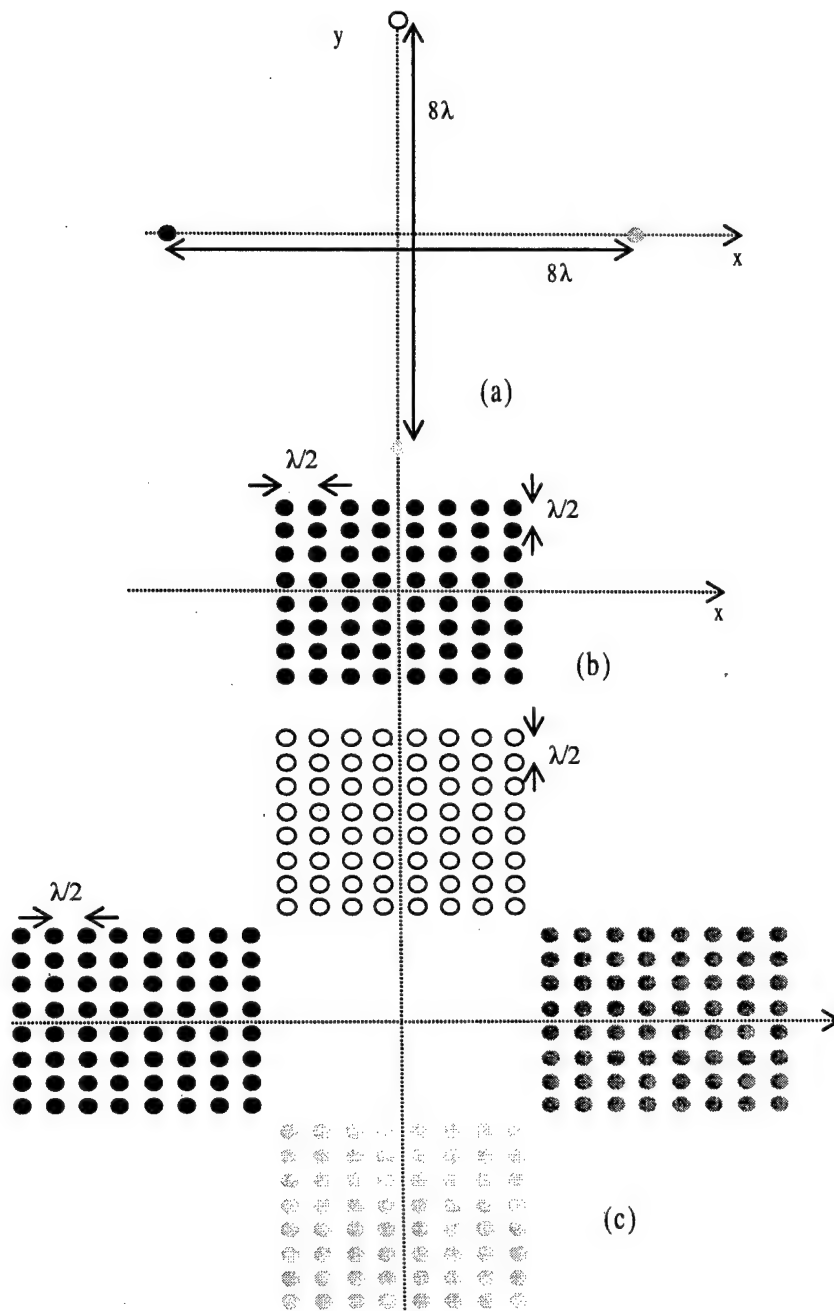


Figure 1: (a) Transmit array; (b) Receive array; (c) Coarray

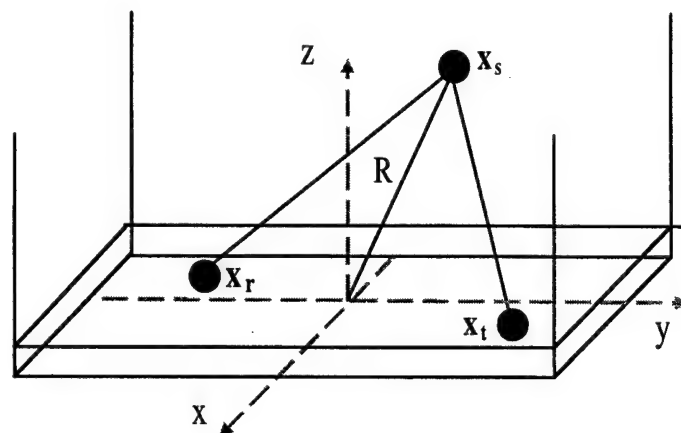


Figure 2: Path of a signal transmitted from x_t , reflected from x_s , and received at x_r . The wall width is along x-axis and y-axis represents its height, with the origin at the center of the wall. The length of the room lies along the positive z-axis.

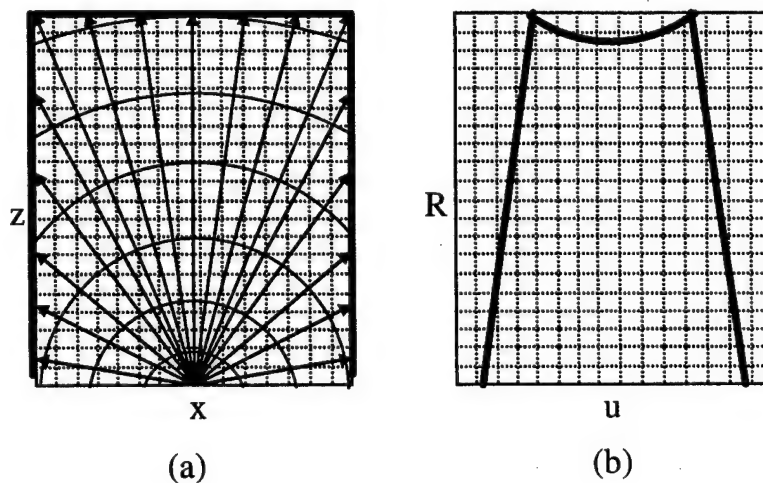


Figure 3:(a) Geometry depicting the ranges and angles corresponding to points on the side and the opposing walls in the x-z plane; (b) The side and the opposing wall in the R-u plane.

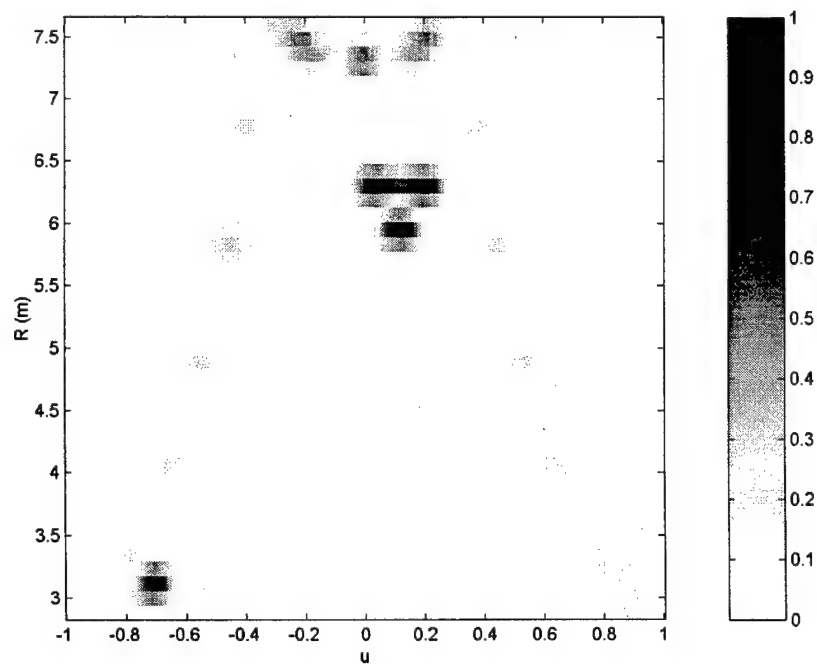


Figure 4: B-Scan image with exact knowledge of wall parameters

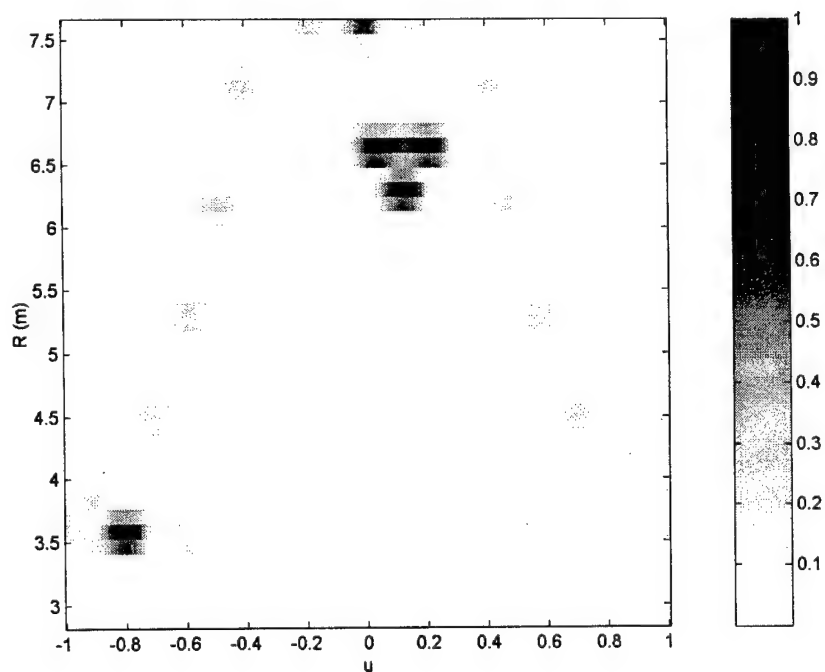


Figure 5: B-Scan Image with no knowledge of wall parameters

Target No.	Range (m)	U	v	Reflectivity
1.	3.0	-0.7	0	$0.707-j0.707$
2.	6.0375	0.05	0	$0.707+j0.707$
3.	6.0375	0.19	0	$0.5+j.866$
4.	5.7	0.12	0	$0.866+j0.5$

Table 1: Locations and Reflectivities of the stationary targets in the room.

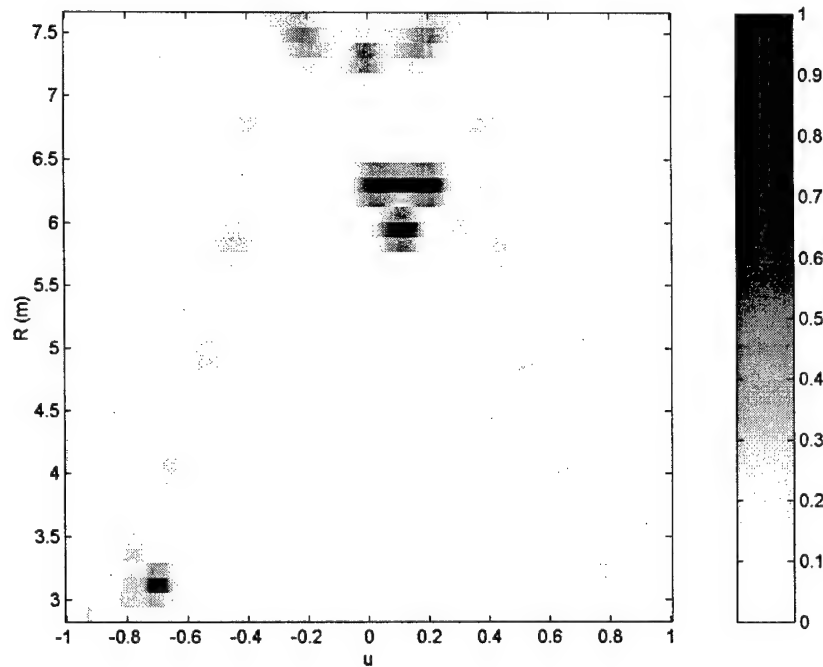


Figure 6: B-scan image with errors in transmit array locations

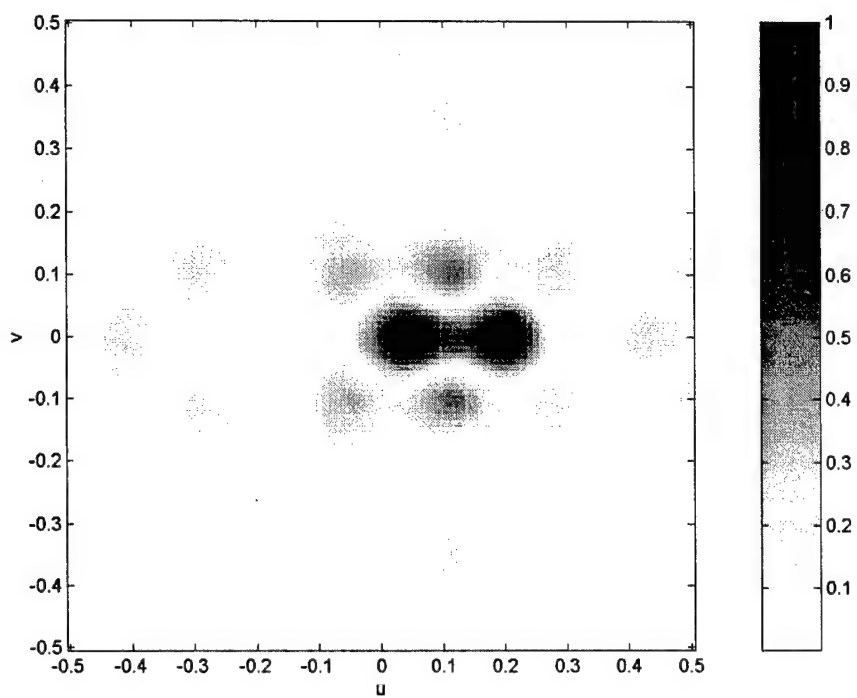


Figure 7: C-Scan image at range 6.0375 m.

Time-frequency ESPRIT for direction-of-arrival estimation of chirp signals

Aboulnasr Hassanien, Alex B. Gershman, and Moeness G. Amin

Abstract

In this paper, we develop an ESPRIT-type algorithm for estimating the Directions-Of-Arrival (DOA's) of multiple chirp signals using Spatial Time-Frequency Distributions (STFD's). An averaged STFD matrix (or multiple averaged STFD matrices) are used instead of the covariance matrix to estimate the signal and noise subspaces. The proposed algorithm is shown to provide a significant performance improvement over the traditional ESPRIT algorithm for FM sources, specifically in situations with closely spaced sources and low Signal-to-Noise Ratios (SNR's). Simulation results are provided to illustrate the performance of the proposed approach in scenarios with multiple narrowband chirp sources.

I. Introduction

The problem of DOA estimation in the presence of chirp and FM signal sources in sensor arrays arises in Synthetic Aperture Radar (SAR), Synthetic Aperture Sonar (SAS), inverse SAR and SAS (ISAR and ISAS), Doppler radar and sonar imaging, as well as in mobile communications, where FM signal waveforms can be intentionally transmitted [1]-[9]. In conventional array processing, subspace methods (for example, MUSIC and ESPRIT) are commonly applied and achieve excellent performance at a moderate computational cost. However, conventional subspace methods are based on the assumption that the received signals are stationary. As a result, the performance of conventional subspace-based DOA estimation techniques can degrade when dealing with nonstationary chirp signals.

Recently, STFD's have emerged as an efficient means of array processing in the case of multiple FM signals [10]-[14]. Spreading the noise power while localizing the sources in the time-frequency domain helps to improve the DOA estimation performance and enhance robustness against sensor noise. However, the existing narrowband STFD-based DOA estimation techniques [10]-[13] are based on a spectral search and, as a result, have high computational costs.

In this paper, a search-free STFD-based (time-frequency) ESPRIT algorithm is developed. In order to obtain improved estimates of the signal and noise subspaces, we use an averaged STFD matrix (or multiple averaged STFD matrices) in place of the covariance matrix which is used in the conventional ESPRIT algorithm. This averaging involves time-frequency points that correspond to source signatures with a maximal energy. The source DOA's are then estimated using either the least squares (LS) or the total least squares (TLS) ESPRIT approach [16]-[18].

The proposed technique enables to separate the signals in different averaged STFD matrices prior to DOA estimation and, therefore, makes it possible to estimate the source DOA's in the case when the number of array sensors is less than the number of sources. Moreover, closely spaced sources with well separated time-frequency signatures can be

efficiently resolved by separating them in different averaged STFD matrices and applying the ESPRIT algorithm to each of them independently.

To validate the effectiveness of the proposed technique and compare its performance with the conventional array processing methods, simulation results for chirp sources are presented. It is shown that significant performance gains can be achieved by the proposed algorithm compared to the conventional LS- and TLS-based ESPRIT techniques.

II. Signal Model

Consider L chirp signals impinging on a Uniform Linear Array (ULA) of M sensors. The array output (data snapshot) vector $\mathbf{x}(t) \in \mathbb{C}^{M \times 1}$ is modeled as

$$\mathbf{x}(t) = \mathbf{A}\mathbf{d}(t) + \mathbf{n}(t), \quad t = 1, \dots, N \quad (1)$$

where $\mathbf{d}(t) \in \mathbb{C}^{L \times 1}$ and $\mathbf{n}(t) \in \mathbb{C}^{M \times 1}$ are the vectors of signal waveforms and sensor noise, respectively, N is the number of data snapshots available, and $\mathbf{A} \in \mathbb{C}^{M \times L}$ is the array direction matrix. It is assumed that \mathbf{A} is full rank (which means that the steering vectors corresponding to L different angles of arrival are linearly independent). We assume that the noise is a spatially and temporally white zero-mean process, i.e.

$$\mathbb{E}\{\mathbf{n}(t)\mathbf{n}^H(s)\} = \sigma^2 \mathbf{I} \delta_{t,s} \quad (2)$$

where \mathbf{I} is the identity matrix, σ^2 is the noise variance, $\delta_{t,s}$ is the Kronecker delta, and $(\cdot)^H$ stands for the Hermitian transpose. The direction matrix can be expressed as

$$\mathbf{A} = [\mathbf{a}(\theta_1), \dots, \mathbf{a}(\theta_L)] \quad (3)$$

where

$$\mathbf{a}(\theta) = [1, e^{j\frac{\omega}{c}\Delta \sin \theta}, \dots, e^{j\frac{\omega}{c}\Delta(M-1) \sin \theta}]^T \quad (4)$$

is the steering vector, $\{\theta_k\}_{k=1}^L$ are the signal DOA's, ω is the central frequency, c is the propagation speed, Δ is the interelement spacing, and $(\cdot)^T$ denotes the transpose. Note that this model corresponds to the assumption of *narrowband* chirp signals where changes

of the central frequency within the observation interval are negligibly small (i.e., the matrix \mathbf{A} is time independent) [10]-[13]. The case of wideband chirp signals is addressed in [14] and [15].

The sample Spatial Pseudo-Wigner-Ville Distribution (SPWVD) matrix is given by [10]-[13]

$$\hat{\mathbf{D}}_{\mathbf{xx}}(t, f) = \sum_{\tau=-(K-1)/2}^{(K-1)/2} \mathbf{x}(t + \tau) \mathbf{x}^H(t - \tau) e^{-j4\pi f \tau} \quad (5)$$

where K is the odd window length. Taking the expectation, and assuming that the source waveforms and sensor noise are statistically independent, we have that [10], [14]

$$\begin{aligned} \mathbf{D}_{\mathbf{xx}}(t, f) &= \mathbb{E}\{\hat{\mathbf{D}}_{\mathbf{xx}}(t, f)\} \\ &= \mathbf{A} \mathbf{D}_{\mathbf{dd}}(t, f) \mathbf{A}^H + \sigma^2 \mathbf{I} \end{aligned} \quad (6)$$

where

$$\mathbf{D}_{\mathbf{dd}}(t, f) = \mathbb{E}\{\hat{\mathbf{D}}_{\mathbf{dd}}(t, f)\} \quad (7)$$

$$\hat{\mathbf{D}}_{\mathbf{dd}}(t, f) = \sum_{\tau=-(K-1)/2}^{(K-1)/2} \mathbf{d}(t + \tau) \mathbf{d}^H(t - \tau) e^{-j4\pi f \tau} \quad (8)$$

The relationship (6) holds true for each (t, f) point. In order to reduce the effect of the sensor noise, an averaging over multiple (t, f) points (corresponding to the autoterms of the STFD) can be used. The eigenstructure properties of the averaged STFD matrix can be exploited to estimate the signal DOA's in a similar way as in the conventional subspace-based array processing techniques [10]-[14].

In practical situations, the sample STFD matrices (5) are used instead of the exact (statistically expected) matrices (6). In the case of sources with distinct time-frequency signatures, it is possible to construct the averaged STFD matrices over time-frequency points belonging to a subset of the sources in the field-of-view. Using this approach, sources with close angular spacing can be efficiently resolved by separating them in different averaged STFD matrices and applying a DOA estimation algorithm to each matrix independently.

III. Time-Frequency ESPRIT

Let the averaged STFD matrix $\tilde{\mathbf{D}}_{\mathbf{xx}}$ be formed by averaging of multiple SPWVD matrices computed at PJ different time-frequency points $\{t_p, f_i\}$ ($p = 1, \dots, P; i = 1, \dots, J$) that belong to the time-frequency signatures of L_0 source signals ($L_0 \leq L < M$):

$$\tilde{\mathbf{D}}_{\mathbf{xx}} = \sum_{p=1}^P \sum_{i=1}^J \hat{\mathbf{D}}_{\mathbf{xx}}(t_p, f_i) \quad (9)$$

Note that the values of P and J may vary with time and can be determined by means of detection of the source time-frequency signatures, see [14], [19], and [20]. Let us divide a ULA of M sensors into two identical subarrays of $M - 1$ sensors shifted by the interelement spacing Δ , as shown in Fig. 1. As in the conventional ESPRIT case, define the submatrices \mathbf{A}_1 and \mathbf{A}_2 by deleting the last and first rows from \mathbf{A} respectively, i.e. let

$$\mathbf{A} = \begin{bmatrix} \mathbf{A}_1 \\ \text{last row} \end{bmatrix} = \begin{bmatrix} \text{first row} \\ \mathbf{A}_2 \end{bmatrix} \quad (10)$$

Then, \mathbf{A}_1 and \mathbf{A}_2 are related as

$$\mathbf{A}_2 = \mathbf{A}_1 \Phi \quad (11)$$

where

$$\Phi = \text{diag}\{e^{j\mu_1}, \dots, e^{j\mu_{L_0}}\} \quad (12)$$

and

$$\mu_i = (\omega/c)\Delta \sin \theta_i \quad (13)$$

are the source spatial frequencies.

Let \mathbf{U}_S be the matrix formed from the eigenvectors of $\tilde{\mathbf{D}}_{\mathbf{xx}}$ that correspond to the L_0 eigenvalues with the largest magnitude. As the columns of the steering matrix \mathbf{A} and the matrix $\tilde{\mathbf{U}}_S$ span approximately¹ the same (signal) subspace of the dimension L_0 , there exists a nonsingular $L_0 \times L_0$ matrix \mathbf{T} such that

$$\mathbf{U}_S \simeq \mathbf{A}\mathbf{T} \quad (14)$$

¹Note that \mathbf{U}_S is obtained from the eigendecomposition of the *sample* STFD matrix $\tilde{\mathbf{D}}_{\mathbf{xx}}$.

Applying this transformation to the sub-matrices \mathbf{A}_1 and \mathbf{A}_2 , we obtain

$$\mathbf{U}_{S,1} \simeq \mathbf{A}_1 \mathbf{T} \quad (15)$$

$$\mathbf{U}_{S,2} \simeq \mathbf{A}_2 \mathbf{T} \quad (16)$$

where $\mathbf{U}_{S,1}$ and $\mathbf{U}_{S,2}$ are formed by deleting the last and first rows of \mathbf{U}_S , respectively, that is

$$\mathbf{U}_S = \begin{bmatrix} \mathbf{U}_{S,1} \\ \text{last row} \end{bmatrix} = \begin{bmatrix} \text{first row} \\ \mathbf{U}_{S,2} \end{bmatrix} \quad (17)$$

Using (11) and (15)-(16) yields

$$\mathbf{U}_{S,2} \simeq \mathbf{U}_{S,1} \mathbf{\Psi} \quad (18)$$

where the matrices $\mathbf{\Psi}$ and $\mathbf{\Phi}$ are related as

$$\mathbf{\Psi} = \mathbf{T}^{-1} \mathbf{\Phi} \mathbf{T} \quad (19)$$

This means that $\{e^{j\mu_i}\}_{i=1}^{L_0}$ are the eigenvalues of the matrix $\mathbf{\Psi}$ [16]-[18].

Now, we can formulate our time-frequency ESPRIT algorithm as follows:

- *Step 1:* Compute the sample SPWVD matrices $\hat{\mathbf{D}}_{\mathbf{x}\mathbf{x}}(t, f)$ for all time-frequency points of interest and select the maximal energy points that belong to the source signatures.
- *Step 2:* Compute the averaged STFD matrix $\tilde{\mathbf{D}}_{\mathbf{x}\mathbf{x}}$ for a previously selected part of sources (for $L_0 \leq L$ sources) by means of involving in the averaging process only the time-frequency points that belong to the spatial signatures of these L_0 sources.
- *Step 3:* Compute the eigendecomposition of $\tilde{\mathbf{D}}_{\mathbf{x}\mathbf{x}}$ and obtain \mathbf{U}_S .
- *Step 4:* Obtain an estimate $\hat{\mathbf{\Psi}}$ of the matrix $\mathbf{\Psi}$ by solving (18) using either LS or TLS approaches.
- *Step 5:* Obtain estimates of the spatial frequencies μ_i from the eigenvalues of $\hat{\mathbf{\Psi}}$ and use them to find the estimates of the source DOA's θ_i .
- *Step 6:* Repeat Steps 2-5 for other (selected) parts of sources.

Note that algorithms are available to classify auto- and cross-terms in STFD's [19], [20]. These techniques can be used in Step 2.

The possibility of separating sources in different averaged STFD matrices prior to DOA estimation can essentially improve the performance of the ESPRIT algorithm, especially in the low SNR case and in the presence of closely spaced sources which are well separated in the time-frequency domain. However, this will increase the computational costs relative to the conventional ESPRIT algorithm because in this case ESPRIT should be applied simultaneously to several averaged STFD matrices.

IV. Simulation Results

We assume a ULA with $\Delta = \lambda/2$. This array is divided into 2 subarrays with the inter-subarray displacement $\lambda/2$ as shown in Fig. 1. Two narrowband chirp signals impinge on the array from the sources located at $\theta_1 = 3^\circ$ and $\theta_2 = 6^\circ$. After downconversion, the source waveforms are modeled as

$$d_1(t) = e^{j(\omega_1 t + \beta_1 t^2/2)}$$

$$d_2(t) = e^{j(\omega_2 t + \beta_2 t^2/2)}$$

The initial discrete-time frequencies of the source signals are chosen to be $\omega_1 = 0$ and $\omega_2 = \pi$ while their chirp rates are assumed to be $\beta_1 = 0.002$ and $\beta_2 = -0.002$, respectively. An observation interval of $N = 255$ snapshots is considered. Figure 2 shows the pseudo-Wigner-Ville distribution of the signals in the first array sensor. The noise is modeled as a complex Gaussian zero-mean spatially and temporally white process. A total of 300 independent Monte-Carlo simulation runs have been used to obtain each simulated point. The averaged STFD matrix $\tilde{\mathbf{D}}_{xx}$ is computed for each source signal separately by averaging the sample STFD matrices computed at 150 different time-frequency points that belong to the source signatures.

In the first example, we use an array of $M = 10$ sensors. Figure 3 displays the DOA estimation Root-Mean-Square Errors (RMSE's) versus the SNR for the conventional LS-

and TLS-ESPRIT algorithms, as well as for the proposed time-frequency modification of the LS- and TLS-ESPRIT techniques. Additionally, the so-called deterministic CRB [21] is shown in this figure (the latter bound is computed under the assumption that the source waveforms are unknown deterministic sequences). From Fig. 3, it is clear that the time-frequency ESPRIT algorithm has a substantial improvement over conventional ESPRIT. This is especially true in the low SNR case. Note that neither time-frequency ESPRIT nor conventional ESPRIT approaches the deterministic CRB.

In the second example, the source SNR is fixed and equal to 4 dB, while the number of array sensors is varied. Figure 4 shows the RMSE's of the same four methods as in the previous example versus the number of sensors M . It is evident from this figure that the time-frequency ESPRIT algorithm has substantially better performance than the conventional ESPRIT technique. Furthermore, at small values of M , the RMSE's of time-frequency ESPRIT can be lower than the deterministic CRB. To explain this behavior, we note that the displayed bound assumes unknown deterministic signal waveforms [21] and, therefore, does not take into account the chirp signal structure [8]. However, this structure is exploited in the proposed algorithm. Obviously, this can cause situations when the DOA estimation accuracy of the proposed technique is better than the deterministic CRB.

V. Conclusions

A time-frequency ESPRIT algorithm is introduced for DOA estimation of chirp signals in sensor arrays. The proposed algorithm is based on the concept of Spatial Time-Frequency Distributions (STFD's) and employs multiple averaged STFD matrices, instead of the covariance matrix (used in conventional array processing methods), to obtain the estimates of the signal DOA's. Computer simulations show that in scenarios with chirp signals, the proposed technique outperforms the conventional ESPRIT algorithm. The performance improvement is especially high in the case when the SNR is low or the sources are closely spaced.

References

- [1] *Advanced Radar Techniques and Systems*, G. Galati, Ed., IEE Press, 1993.
- [2] J. Chatillon, M. E. Bouhier, and M. E. Zakharia, "Synthetic aperture sonar for seabed imaging: relative merits of narrowband and wideband approaches," *IEEE Journ. Oceanic Engineering*, vol. 17, pp. 95-105, Jan. 1992.
- [3] S. Barbarossa, A. Scaglione, and G. B. Giannakis, "Product high-order ambiguity function for multicomponent polynomial-phase signal modeling," *IEEE Trans. Signal Processing*, vol. 46, pp. 691-707, March 1998.
- [4] P. M. Djuric and S. M. Kay, "Parameter estimation of chirp signals," *IEEE Trans. Acoust., Speech, Signal Processing*, vol. 38, pp. 2118-2126, Dec. 1990.
- [5] S. Peleg and B. Porat, "Estimation and classification of polynomial-phase signals," *IEEE Trans. Inform. Theory*, vol. 37, pp. 422-430, March 1991.
- [6] S. Shamsunder, G. B. Giannakis, and B. Friedlander, "Estimating random-amplitude polynomial phase signals: A cyclostationary approach," *IEEE Trans. Signal Processing*, vol. 43, pp. 492-505, Feb. 1995.
- [7] O. Besson, M. Ghogho, and A. Swami, "Parameter estimation for random amplitude chirp signals," *IEEE Trans. Signal Processing*, vol. 47, pp. 3208-3219, Dec. 1999.
- [8] A. B. Gershman, M. Pesavento, and M. G. Amin, "Estimating parameters of multiple wideband polynomial-phase sources in sensor arrays," *IEEE Trans. Signal Processing*, vol. 49, pp. 2924-2934, Dec. 2001.
- [9] X-G. Xia, "Discrete chirp-Fourier transform and its application to chirp rate estimation," *IEEE Trans. Signal Processing*, vol. 48, pp. 3122-3133, Nov. 2000.
- [10] A. Belouchrani, and M. G. Amin, "Time-frequency MUSIC," *IEEE Signal Processing Letters*, vol. 6, pp. 109-110, May 1999.
- [11] Y. Zhang and M. G. Amin, "Beamspace time-frequency MUSIC with application to airborne antenna array," *Proc. Asilomar Conf. Signals, Systems, and Computers*, Pacific Grove, CA, November 1998, vol. 1, pp. 838-841.

- [12] Y. Zhang, W. Mu, and M. G. Amin, "Subspace analysis of spatial time-frequency distribution matrices," *IEEE Trans. Signal Processing*, vol. 49, pp. 747-759, April 2001.
- [13] M. G. Amin and Y. Zhang, "Direction finding based on spatial time-frequency distribution matrices," *Digital Signal Processing*, vol. 10, no. 4, pp. 325-339, Oct. 2000.
- [14] A. B. Gershman and M. G. Amin, "Wideband direction-of-arrival estimation of multiple chirp signals using spatial time-frequency distributions," *IEEE Signal Processing Letters*, vol. 7, pp. 152-155, June 2000.
- [15] B. Völcker and B. Ottersten, "Linear chirp parameter estimation from multi channel data," *Proc. Asilomar Conf. Signals, Systems, and Computers*, Pacific Grove, CA, November 1999.
- [16] R. Roy and T. Kailath, "ESPRIT-estimation of signal parameters via rotational invariance techniques," *IEEE Trans. Acoust., Speech, Signal Processing*, vol 37, pp. 984-995, July 1989.
- [17] M. Haardt, *Efficient one-, two-, and multidimensional high-resolution array signal processing*, Ph.D. Thesis, Munich, October 1996.
- [18] B. Ottersten, M. Viberg, and T. Kailath, "Performance analysis of the total least squares ESPRIT algorithm," *IEEE Trans. Signal Processing*, vol. 39, pp. 1122-1135, May 1991.
- [19] L. Cirillo, A. Zoubir, N. Ma and M. G. Amin, "Automatic classification of auto- and cross-terms of time-frequency distributions in antenna arrays," *Proc. ICASSP'02*, Orlando, FL, May 2002.
- [20] L. Cirillo, A. Zoubir, and M. G. Amin, "Selection of auto- and cross-terms for blind non-stationary source separation," *Proc. IEEE Int. Symposium on Signal Processing and Information Technology* Cairo, Egypt, 2001.
- [21] P. Stoica and A. Nehorai, "Performance study of conditional and unconditional direction-of-arrival estimation," *IEEE Trans. Acoust., Speech, Signal Processing*, vol. 38, pp. 1783-1795, Oct. 1990.

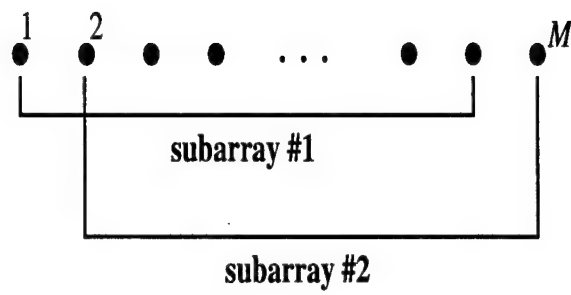


Fig. 1. The array structure.

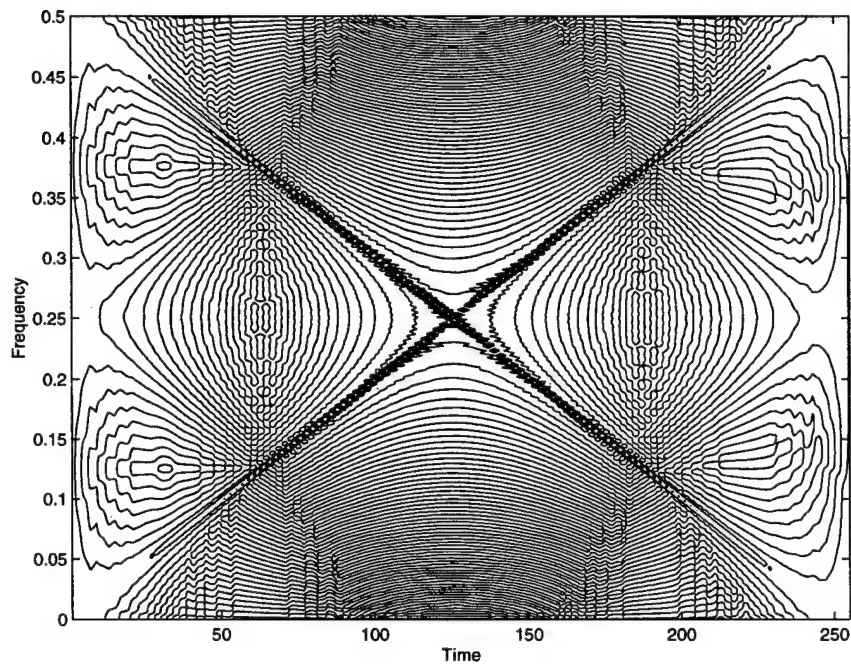


Fig. 2. Pseudo-Wigner-Ville distribution of the source waveforms.

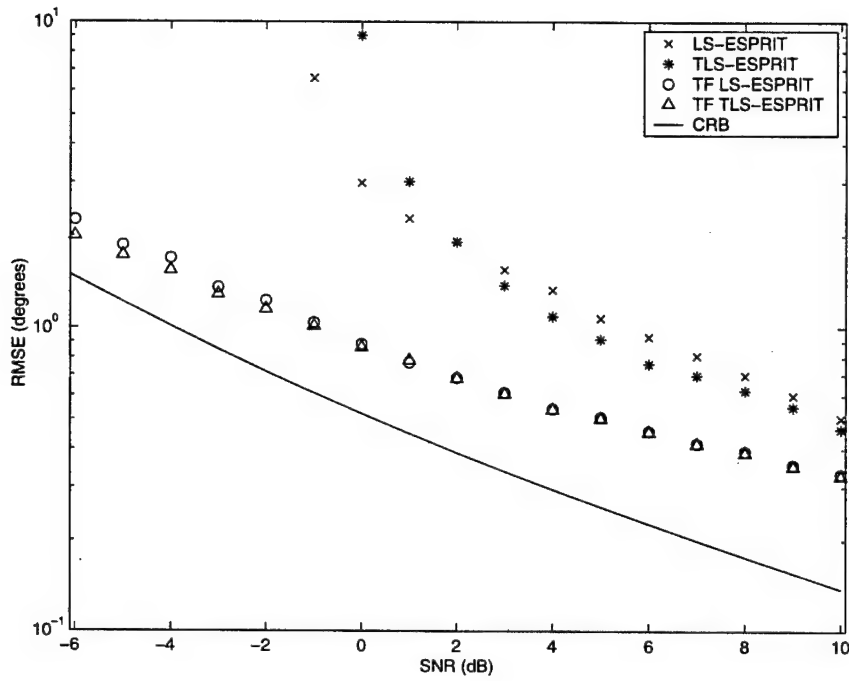


Fig. 3. The DOA estimation RMSE's versus the SNR. First example: $\theta_1 = 3^\circ$, $\theta_2 = 6^\circ$, and $M = 10$.

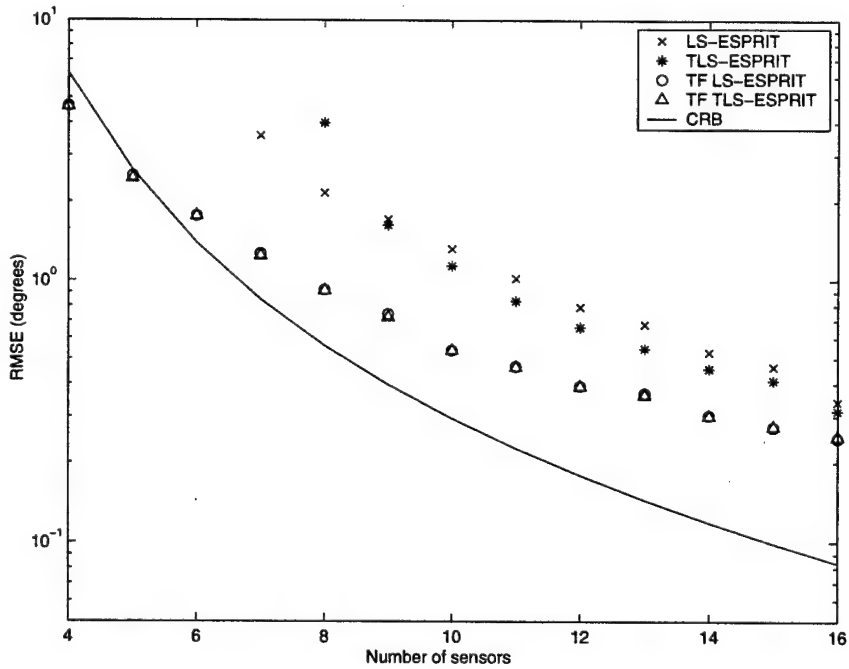


Fig. 4. The DOA estimation RMSE's versus the number of sensors M . Second example: $\theta_1 = 3^\circ$, $\theta_2 = 6^\circ$, and SNR = 4 dB.

Automatic Classification of Auto- and Cross-Terms of Time-Frequency Distributions in Antenna Arrays

Luke A. Cirillo, Abdelhak M. Zoubir, Ning Ma, and Moeness G. Amin

Abstract

The problem of selecting auto- and cross-terms of time-frequency distributions (TFDs) of nonstationary signals impinging on a multi-antenna receiver is considered. A detection approach is introduced which allows performance measurement and comparison of various schemes via receiver operating characteristics. Array averaging and array differencing techniques are both employed to form a basis for time-frequency (t-f) point selection. The proposed classification method is evaluated against the bootstrap-based method. It is shown that the former offers improved performance and simplified implementations.

I. Introduction

Time-frequency distributions have recently been proposed for applications to array signal processing problems [1], [2]. For this purpose, spatial time-frequency distributions (STFDs) have been introduced and represented in a matrix form. The elements of a STFD matrix are the time-frequency distributions and the cross-time frequency distributions of the data received at the multi-sensor array. It has been shown that the relationship between the spatial time-frequency distributions of the sensor data and the time-frequency distributions of the sources is identical to that of the sensor data covariance matrix and the sources' correlation matrix. This key property permits direction finding and blind source separation to be performed using the sources' time-frequency localization properties.

Blind source separation has been typically solved using statistical information available on source signals, including second or higher order statistics. A primary contribution in this area was to show that the STFDs are an effective alternative to separating sources whose signatures are different in the t-f domain [1], [2]. Successful applications of STFDs to source separation require computing STFDs at different t-f points. The auto-terms, which enforce the diagonal structure of the source TFD, are then incorporated into a joint-diagonalization (JD) technique to estimate the mixing, or the array manifold matrix. This technique was further generalized to incorporate cross-term STFD matrices by performing combined JD and joint off-diagonalization (JOD) [3]. In both of these methods, proper selection of either auto- or cross-term locations in the time-frequency plane has remained an important and necessary task.

A statistical test to decide whether a t-f location is dominated by auto- or cross-terms has been proposed in [4]. Array averaging of the TFDs is used to reduce the cross-terms without smearing the auto-terms [5], allowing the auto-terms to be more pronounced and easier to detect in the t-f domain. However, as shown in [6], there are advantages to using both auto- and cross-terms in combined JD/JOD. This requires devising an equivalent technique for cross-term enhancement and selections.

In this paper we propose a simple method for the suppression of auto-terms and enhancement of cross-terms. A procedure for automatic selection of auto- and cross- terms is proposed and a performance comparison to the bootstrap based scheme is given.

II. Signal Model

We consider the general problem of a number of independent non-stationary sources impinging on an array of sensors which has at least as many elements as the number of sources. The model for the array output is given as follows,

$$\mathbf{x}(t) = \mathbf{A}\mathbf{s}(t) + \mathbf{n}(t), \quad (1)$$

where $\mathbf{x}(t) = [\mathbf{x}_1(t), \dots, \mathbf{x}_m(t)]'$ is the array output vector, $\mathbf{s}(t) = [\mathbf{s}_1(t), \dots, \mathbf{s}_d(t)]'$ is the $d \times 1$ source signal vector and $\mathbf{n}(t)$ is the $m \times 1$ independent and identically distributed noise vector of variance σ^2 , at time t . The $m \times d$ mixing matrix \mathbf{A} is of the form $\mathbf{A} = [\mathbf{a}_1, \dots, \mathbf{a}_d]$, where $\mathbf{a}_i = [\mathbf{a}_{1i}, \dots, \mathbf{a}_{mi}]'$ denotes the steering vector for source i . Here m represents the number of array elements and d denotes the number of source signals.

A. Spatial TFD

The discrete form of Cohen's class of TFD's, for a signal $x(t)$ is given by [7]

$$D_{xx}(t, f) = \sum_{l, m=-\infty}^{\infty} \phi(m, l) x(t + m + l) x^*(t + m - l) e^{-j4\pi fl},$$

where $\phi(m, l)$ is the kernel defining the distribution. The STFD matrix, based on $D_{xx}(t, f)$ has been introduced in [1] and is given by

$$\mathbf{D}_{xx}(\mathbf{t}, \mathbf{f}) = \sum_{l, m=-\infty}^{\infty} \phi(\mathbf{m}, \mathbf{l}) \mathbf{x}(\mathbf{t} + \mathbf{m} + \mathbf{l}) \mathbf{x}^H(\mathbf{t} + \mathbf{m} - \mathbf{l}) e^{-j4\pi \mathbf{f} \mathbf{l}}.$$

In the (noise-free) case of auto-sensor TFD's,

$$D_{x_k x_k} = \sum_{u=1}^d \sum_{v=1}^d a_{ku} a_{kv}^* D_{s_u s_v}(t, f) \quad (2)$$

where H is the Hermition operator and $D_{s_i s_j}(t, f)$ is the ij element of $\mathbf{D}_{ss}(\mathbf{t}, \mathbf{f})$; the source TFD matrix. The ij element of matrix $\mathbf{D}_{xx}(\mathbf{t}, \mathbf{f})$ is equal to $D_{x_i x_j}(t, f)$, which is obtained

from the expression for $D_{xx}(t, f)$ by replacing the bilinear product of $x(t)$ with the data received at sensors i and j .

Below we consider only the pseudo Wigner-Ville distribution [7] with odd window length L and henceforth refer to the STFD matrix as \mathbf{D}_{xx} where the (t, f) parameters are dropped for convenience. The same applies to \mathbf{D}_{ss} .

B. Test Statistic

In [4], identification of auto- and cross-terms is achieved using the test statistic

$$\text{trace} \{ \mathbf{D}_{zz} \} / \text{norm} \{ \mathbf{D}_{zz} \}, \quad (3)$$

where $\text{trace} \{ \cdot \}$ is the matrix trace and $\text{norm} \{ \cdot \}$ is the Frobenius norm of a matrix. With $\hat{\sigma}^2$ being an estimate of σ^2 ,

$$\mathbf{D}_{zz} = \hat{\mathbf{W}}(\mathbf{D}_{xx} - \hat{\sigma}^2 \mathbf{I})\hat{\mathbf{W}}^H, \quad (4)$$

where $\hat{\mathbf{W}}$ is an estimate of the whitening transform \mathbf{W} such that $\mathbf{W}\mathbf{A}\mathbf{D}_{ss}\mathbf{A}^H\mathbf{W}^H$ is a unitary transformation of \mathbf{D}_{ss} .

It is proposed to discriminate between noise and either auto- or cross-terms by using the variance of the test statistic. As only a single value of the test statistic is known at any t-f point, the variance is estimated using a bootstrap resampling scheme by [4]. Once the noise regions in the t-f domain are identified, a threshold is set to discriminate between the auto- and cross-term locations.

III. Selection of Auto-terms

We denote the set of all t-f locations which contain the auto-terms, by \mathcal{S}_A . The test is formulated as follows:

$$\begin{aligned} H_0 : (t_0, f_0) &\notin \mathcal{S}_A \\ H_A : (t_0, f_0) &\in \mathcal{S}_A, \end{aligned} \quad (5)$$

where the null hypothesis H_0 is that the point (t_0, f_0) is not an auto-term. To apply this test, we define

$$\mathcal{S}_A = \left\{ (t, f) \in \mathcal{S}_T : \frac{1}{d} \text{trace} \{ \mathbf{D}_{ss}(t, f) \} > \gamma_A \right\} \quad (6)$$

where \mathcal{S}_T is the set of all locations in the t-f plane and γ_A is an arbitrarily selected bound.

A. Array Averaged TFD

The array averaged TFD improves signal synthesis performance by suppressing the cross-terms [5]. It is given by

$$\begin{aligned} \bar{D}(t, f) &= \frac{1}{m} \text{trace} \{ \mathbf{D}_{xx} \} \\ &= \sum_{u=1}^d \sum_{v=1}^d \beta_{uv} D_{s_u s_v}(t, f), \end{aligned} \quad (7)$$

where $\beta_{uv} = \frac{1}{m} \mathbf{a}_v^H \mathbf{a}_u$ is the spatial correlation coefficient of sources u and v . The value of β_{uv} is one for auto-source terms and less than or equal to one for cross-source terms. This coefficient takes a zero value if the respective sources u and v have orthogonal spatial signatures.

The whitened array average is defined as

$$\bar{D}_z = \text{trace} \{ \hat{\mathbf{W}} \mathbf{D}_{xx} \hat{\mathbf{W}}^H \} / d \quad (8)$$

with expected value $E[\bar{D}_z] = (\text{trace} \{ \mathbf{D}_{ss} \} + \sigma^2 \mathcal{T}_{\mathbf{W}}) / d$, where $\mathcal{T}_{\mathbf{W}} = \text{trace} \{ \mathbf{W} \mathbf{W}^H \}$. This indicates that a test statistic useful for detection of auto-terms can be based on the whitened array average since total cancellation of cross-terms is achieved.

B. Setting the Threshold

In the case of FM signals which have constant power over the observation interval, the variance of the whitened array average can be approximated by

$$\text{Var}[\bar{D}_z] = \sigma_{\bar{D}_z}^2 \approx \left(\frac{\sigma}{d} \right)^2 L (2 \mathcal{T}_{\mathbf{W}} + \sigma^2 \mathcal{T}_{\mathbf{W}^2}),$$

where $\mathcal{T}_{\mathbf{W}^2} = \text{trace}\{(\mathbf{W}\mathbf{W}^H)^2\}$. As \bar{D}_z is approximately normally distributed, a threshold γ for classification of auto-terms is set according to

$$\gamma = \gamma_A + \sigma^2 \mathcal{T}_{\mathbf{W}}/d + N_{1-\alpha}\sigma \bar{D}_z,$$

where N_α is the inverse of the standard normal distribution at probability α .

IV. Selection of cross-terms

We denote the set of all t-f locations that contain cross-terms of interest, by \mathcal{S}_C . The test is formulated as follows:

$$\begin{aligned} H_0 : (t_0, f_0) &\notin \mathcal{S}_C \\ H_A : (t_0, f_0) &\in \mathcal{S}_C \end{aligned} \tag{9}$$

where the set \mathcal{S}_C is defined in a similar manner to (6).

A. Array Differenced TFD

In order to suppress the auto-terms while supporting the cross-terms, we define the array differenced TFD

$$\check{D}(t, f) = \frac{1}{m-1} \sum_{u=1}^m (D_{x_u x_u}(t, f) - \bar{D}(t, f))^2 \tag{10}$$

which corresponds to the sample variance of the auto-sensor TFD's. Expanding the summand with (2) and (7) we obtain

$$\begin{aligned} G_k(t, f) &= D_{x_k x_k}(t, f) - \bar{D}(t, f) \\ &= \sum_{u=1}^d \sum_{v=1}^d \left(a_{ku} a_{kv}^* - \frac{1}{m} \sum_{l=1}^m a_{lu} a_{lv}^* \right) D_{s_u s_v}(t, f) \end{aligned}$$

and for $u = v$ (auto-terms)

$$\begin{aligned} G_k(t, f) &= \sum_{u=1}^d \left(|a_{ku}|^2 - \frac{1}{m} \sum_{l=1}^m |a_{lu}|^2 \right) D_{s_u s_u}(t, f) \\ &= 0, \text{ if } |a_{ij}|^2 = c_j \ \forall i. \end{aligned}$$

Here a_{uv} corresponds to the complex weighting of source v at element u of the array. The array difference results in complete cancellation of auto-terms, provided each sensor of the array has the same gain, even if the sources have different power. The array difference method is illustrated in Figure VII, where there are two chirp signals present having DOA's of 10 and -10 degrees at a 2 sensor array.

B. Setting the Threshold

The variance of the array difference is signal dependent and not easily approximated unless the SNR is very low. A threshold to automatically detect the cross-terms may be set by the following function

$$\gamma = \hat{\mu} + \beta \hat{\sigma} \quad (11)$$

where $\hat{\mu}$ and $\hat{\sigma}$ are estimates of the mean and standard deviation of the array difference respectively. Due to the peaks of auto- or cross-terms in the distribution, the mean may be estimated using the median of each time-slice, and the standard deviation as the average absolute deviation from this value. A suitable value for the parameter β may be in the range 3 to 5 depending on the rate of false classification that is considered acceptable.

V. Point Classification

In blind source separation (BSS) and direction of arrival (DOA) estimation, the ultimate goal of point selection is to allow construction of STFD matrices with either a strong diagonal or off-diagonal structure. This implies that only peaks of the auto- and cross-TFD's should be in \mathcal{S}_A or \mathcal{S}_C . In the case of a signal synthesis problem, we wish to select as many of the desired signal's auto-TFD terms as possible without including cross- or noise-terms. This will determine the appropriate value for the bounds γ_A or γ_C .

A. Point Classification Scheme

There are t-f locations dominated by either auto-, cross- or noise-terms. Using the array averaged (AA) TFD cross-terms are suppressed while the array differenced (AD)

TFD suppresses auto-terms. This translates the classification problem with three classes, into two classification problems each containing two classes. A proposed point classification scheme is illustrated in Figure 2.

The method of point classification involves thresholding of the appropriate TFD to obtain a set of t-f points. The TFD is also smoothed using a two-dimensional filter to reduce the effect of noise, and a threshold is applied to obtain another set of t-f points. This set of points is processed using binary morphological operations under the assumption that auto- and cross-terms will have some structure or connected shape in the TF plane. The block labelled O-C in Figure 2 signifies opening and closing operations [8] are used. The final decision is obtained as the intersection of these sets of t-f points. The result is a reduction in the false classification rate compared to that observed with simple thresholding.

B. Performance Evaluation

Performance of the classification scheme is evaluated by means of an operating characteristic (OC) curve. This gives the probability of (correct) classification for a particular probability of false classification. The set of t-f locations obtained by point classification of auto- and cross-terms are respectively denoted $\hat{\mathcal{S}}_A$ and $\hat{\mathcal{S}}_C$. Accordingly, empirical probabilities of detection and false alarm:

$$P_D = \# \{ \mathcal{S}_A \cap \hat{\mathcal{S}}_A \} / \# \{ \mathcal{S}_A \},$$

$$P_{FA} = \# \{ \hat{\mathcal{S}}_A - \mathcal{S}_A \} / \# \{ \mathcal{S}_T - \mathcal{S}_A \},$$

where $\# \{ \cdot \}$ denotes the number of elements in the set.

VI. Simulation

In the following simulations we choose γ_A and γ_C to be 3dB below the peak of the source signals auto- and cross-terms respectively. The threshold of each point detection scheme is varied in order to generate the operating characteristic. Herein point detection using

the array average and array difference will be referred to as method one and the bootstrap resampling scheme will be called method two.

In the first case, we consider a scenario with two source signals impinging on a three sensor array at 0 dB SNR. The source signals $s_1(t)$ and $s_2(t)$ are chirps with start and end frequencies $(0.3\pi, 0.1\pi)$ and $(0.25\pi, 0.01\pi)$ respectively. The OC's of method one and two are shown in Figure 3.

In the second case we consider a scenario with four source signals impinging on a five sensor array at 5 dB SNR. The source signals $s_1(t)$ and $s_2(t)$ are as defined previously. Signal $s_3(t)$ is a chirp with start and end frequency of $(0.2\pi, 0.325\pi)$. The signal $s_4(t)$ is of the form

$$s_4(t) = \exp[j2\pi(K_1 t^{1.5} + K_2 t)],$$

where K_1 and K_2 are chosen such that the start and end frequencies are $(0.25\pi, 0.5\pi)$. The signal $s_4(t)$ has a non-linear instantaneous frequency and therefore the auto-terms are not properly localized, when using WVD. The OC's of method one and two are shown in Figure 4.

A. Discussion

Simulations show that in low SNR, correct identification of both auto- and cross-terms is achievable with probability of false classification less than 2%. In the first scenario, only 30% of the total cross-terms were identified for 2% miss-classification. However, for the application of BSS, only a few strong cross-terms locations are required.

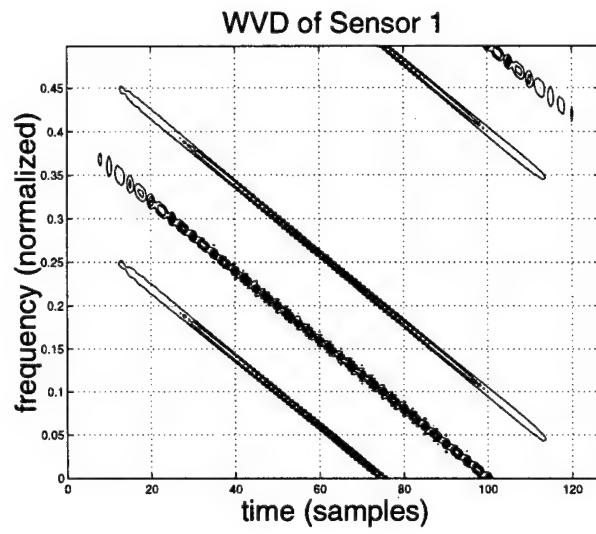
Similar performance in terms of operating characteristic has been achieved using both methods for point classification. In terms of computational complexity, the method of array averaging and differencing are significantly simpler than the bootstrap based method. The computational cost of computing both an array average and an array difference is comparable to computing the test statistic (3). However, bootstrapping requires re-computation of this statistic many times and thus implies a larger computational burden.

VII. conclusion

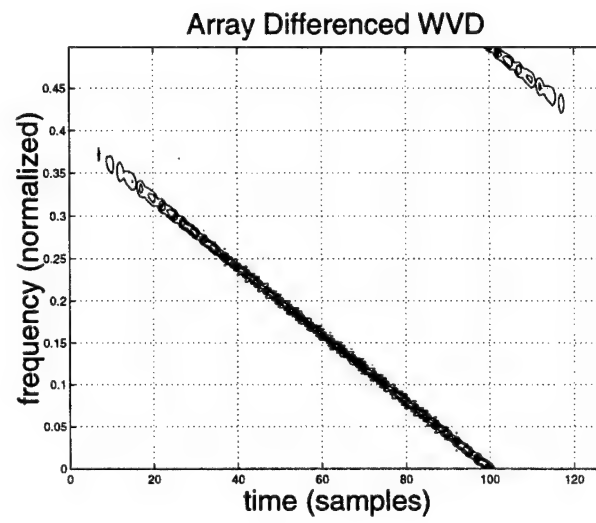
Selecting of auto- and cross-terms from an observed TFD has been cast here as a detection problem. A detection approach allows performance measurement and comparison of various schemes via the operating characteristic curves. The idea of array differencing has been introduced and combined with the method of array averaging to form the basis of a point selection algorithm. Performance of this scheme has been evaluated and compared to a bootstrap based method, showing both performance improvement and computational savings.

References

- [1] A. Belouchrani and M. G. Amin, "Blind source separation based on time-frequency signal representations," *IEEE Transactions on Signal Processing*, vol. 46, no. 11, pp. 2888–2896, November 1998.
- [2] Y. Zhang and M. G. Amin, "Spatial averaging of time-frequency distributions for signal recovery in uniform linear arrays," *IEEE Transactions on Signal Processing*, vol. 48, no. 10, pp. 2892–2902, October 2000.
- [3] M. G. Amin A. Belouchrani, K. Abed-Meraim and A. M. Zoubir, "Joint anti-diagonalization for blind source separation," in *Proc. of the IEEE International Conference on Acoustics, Speech and Signal Processing, (ICASSP)*, Salt LakeCity, Utah, 2001.
- [4] L. A. Cirillo, A. M. Zoubir, and M. G. Amin, "Selection of auto- and cross-terms for blind non-stationary source separation," in *Proc. of the IEEE International Symposium on Signal Processing and Information Technology, (ISSPIT)*, Cairo, Egypt, 2001, (to appear).
- [5] Y. Zhang W. Mu and M. G. Amin, "Bilinear signal synthesis in array processing," in *Proc. of the IEEE International Conference on Acoustics, Speech and Signal Processing, (ICASSP)*, Salt LakeCity, Utah, 2001.
- [6] A. Belouchrani, K. Abed-Meraim amd M. G. Amin, and A. M. Zoubir, "Blind separation of non-stationary sources," *IEEE Signal Processing Letters*, (under review).
- [7] L. Cohen, *Time-Frequency Analysis*, Prentice Hall, 1995.
- [8] K. Castleman, *Digital Image Proessing*, Prentice Hall, 1996.



(a)



(b)

Fig. 1. (a) WVD of chirp signals at the first sensor. (b) Array differenced WVD.

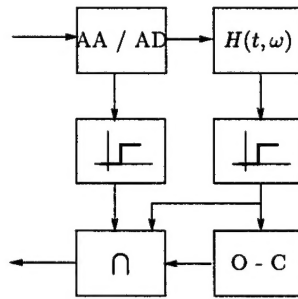


Fig. 2. Point classification scheme for selection of auto- and cross-terms from AA or AD TFD's.

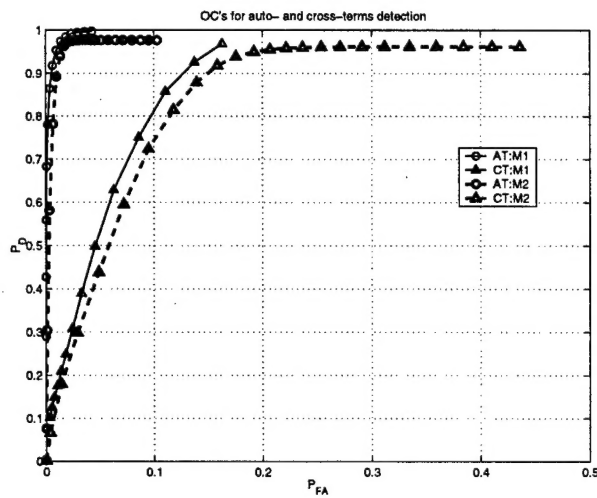


Fig. 3. OC's of methods one and two.

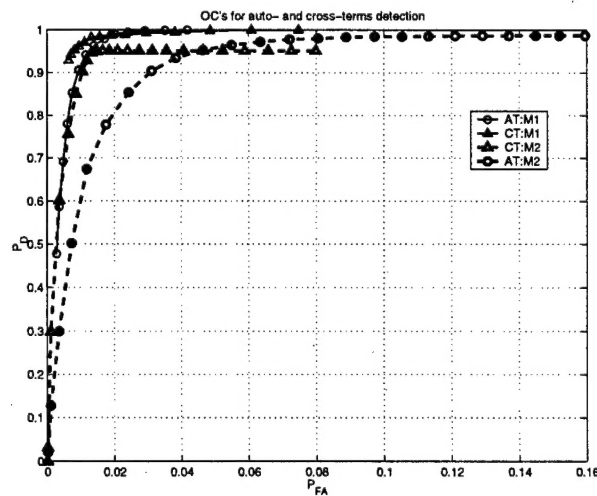


Fig. 4. OC's of methods one and two.

ONR FY02 Collection Data

NAME: Moeness G. Amin

UNIVERSITY: Villanova University

CONTRACT NUMBER: N00014-98-1-0176.

Project title is "Classification and Discrimination of Sources with Time-Varying Frequency and Spatial Spectra."

1. Papers in referred journals (Title; journal):

- W. Mu, M. G. Amin, and Y. Zhang, "Bilinear signal synthesis in array processing," Accepted for publication in the IEEE Transactions on Signal Processing.
- Y. Zhang and M. G. Amin, "Array processing for nonstationary interference suppression in DS/SS communications using subspace projection techniques," IEEE Transactions on Signal Processing, Dec. 2001.
- A. Gershman, M. Pesavento, M. Amin, "Estimating parameters of multiple wideband polynomial-phase sources in sensor arrays," IEEE Transactions on Signal Processing, Dec. 2001.

2. Books or Book chapters:

Two chapters have been submitted and will appear in two books in FY 02-03. They will be reported in next year annual report.

3. Patents (filed - granted):

None

4. Presentations (Invited - Contributed):

- A. Hassanien, A. B. Gershman, and M. G. Amin, "Time-frequency ESPRIT for direction-of arrival estimation of chirp signals," IEEE Sensor Array and Multichannel Signal Processing Workshop, Rosslyn, VA, Aug. 2002.
- Y. Zhang and K. Yang, "Subband adaptive arrays with different decimations," IEEE Sensor Array and Multichannel Signal Processing Workshop, Rosslyn, VA, Aug. 2002.
- Y. Zhang, M. G. Amin, and G. J. Frazer, "A new approach to FM jammer suppression for digital communications", Proceedings of the IEEE Sensor Array and Multichannel Signal Processing Workshop, Rosslyn, VA, Aug. 2002.
- G. J. Frazer and M. G. Amin, "Characterization of near-field scattering using a multiple weighted summed beamformer", Proceedings of SPIE 2002, Advanced Signal Processing Algorithms, Architectures and Implementations XII, Seattle, WA, July 2002.
- L. Cirillo, A. Zoubir, N. Ma, and M. Amin, "Automatic classification of auto-and cross-terms of time-frequency distributions in antenna arrays," Proceedings of the IEEE International Conference on Acoustics, Speech and Signal Processing, Orlando, FL, May 2002.

ONR FY02 Collection Data

- G. J. Frazer and M. G. Amin, "Characterization of near-field scattering using quadratic sensor-angle distributions", Proceedings of the IEEE International Conference on Acoustics, Speech and Signal Processing, Orlando, FL, May 2002.
- L. A. Cirillo, A. M. Zoubir, and M. G. Amin, "Selection of auto- and cross-terms for blind non-stationary sources separation," 1st IEEE International Symposium on Signal Processing and Information Technology, Cairo, Egypt, December 2001.
- G. J. Frazer and M. G. Amin, "Near-field scatter measurements using quadratic sensor-angle distributions", in Proceedings of the Second IEEE Sensor and Multichannel Signal Processing Workshop, Washington, DC, Aug. 2002.

5. Honors (Presidential YIP, elections to Fellow status in major scientific society; appointed editor of scientific journal, Academic promotion, Faculty Excellence award, elected NAS/NAE/IOM, awarded medal by scientific society, Program Chairman of scientific meeting, etc):

IEEE Distinguished Lecturer for the Signal Processing Society 2002-2003

Technical Chair of the 2nd IEEE International Symposium on Signal Processing and Information Technology, Morocco, December 2002.

6. Number of graduate students:

One

7. Number of Post-doctoral students:

Two

8. Number of undergraduate students supported:

None

9. Number of under-represented members by group:

One Woman (postdoc.)

REPORT DOCUMENTATION PAGEForm Approved
OMB No. 0704-0188

Public reporting burden for this collection of information is estimated to average 1 hour per response, including the time for reviewing instructions, searching data sources, gathering and maintaining the data needed, and completing and reviewing the collection of information. Send comments regarding this burden estimate or any other aspect of this collection of information, including suggestions for reducing this burden to Washington Headquarters Service, Directorate for Information Operations and Reports, 1215 Jefferson Davis Highway, Suite 1204, Arlington, VA 22202-4302, and to the Office of Management and Budget, Paperwork Reduction Project (0704-0188) Washington, DC 20503.

PLEASE DO NOT RETURN YOUR FORM TO THE ABOVE ADDRESS.

1. REPORT DATE (DD-MM-YYYY) 1-10-2002		2. REPORT DATE Interim		3. DATES COVERED (From - To) October 2001-September 2002	
4. TITLE AND SUBTITLE Classification and Discrimination of Sources with Time-Varying Frequency and Spatial Spectra				5a. CONTRACT NUMBER	
				5b. GRANT NUMBER G-N00014-98-1-0176	
				5c. PROGRAM ELEMENT NUMBER	
6. AUTHOR(S) Moeness G. Amin				5d. PROJECT NUMBER	
				5e. TASK NUMBER	
				5f. WORK UNIT NUMBER	
7. PERFORMING ORGANIZATION NAME(S) AND ADDRESS(ES) Villanova University 800 Lancaster Ave Villanova, PA 19085				8. PERFORMING ORGANIZATION REPORT NUMBER Acc: 527616	
9. SPONSORING/MONITORING AGENCY NAME(S) AND ADDRESS(ES) G. D. McNeal Office of Naval Research Ballston Center Tower One 800 North Quincy Street Arlinton, VA 22217-5660				10. SPONSOR/MONITOR'S ACRONYM(S)	
				11. SPONSORING/MONITORING AGENCY REPORT NUMBER	
12. DISTRIBUTION AVAILABILITY STATEMENT Approved for Public Release; Distribution is Unlimited					
13. SUPPLEMENTARY NOTES					
14. ABSTRACT This report focuses on improved characterization, separation, suppression, discrimination, and localization of nonstationary and cyclostationary sources using multi-sensor array receivers. The major contribution over the 2001-2002 fiscal year are: 1) Characterization of near-field scattering using quadratic sensor-angle distributions; 2) Improved blind separations of nonstationary sources based on spatial time-frequency distributions; 3) Introducing a unified representation of nonstationary and cyclostationary signals; 4) Devising aperture synthesis for a through-the-wall imaging system; 5) Nonstationary interference suppression in direct sequence spread spectrum communications using space-time oblique projection techniques; 6) Formulating the time-frequency ESPRIT for direction-of-arrival estimation of chirp signals; 7) Automatic classification of auto- and cross-terms of time-frequency distributions in antenna arrays; 8) Proposing a new approach to jammer suppression for digital communications.					
15. SUBJECT TERMS Blind Source Separation, Direction Finding, Time-Frequency Distributions, Sensor-Angle Distributions, Aperture Synthesis, Subband Arrays, Spread Spectrum Communications					
16. SECURITY CLASSIFICATION OF:			17. LIMITATION OF ABSTRACT	18. NUMBER OF PAGES	19a. NAME OF RESPONSIBLE PERSON
a. REPORT	b. ABSTRACT	c. THIS PAGE			19b. TELEPHONE NUMBER (include area code)
U	U	U	UU	95	